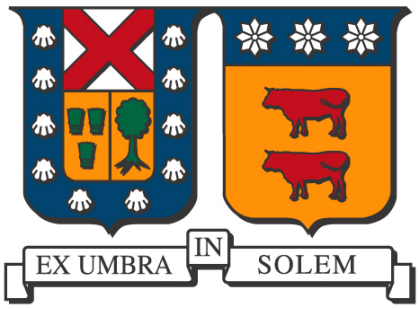

UNIVERSIDAD TECNICA FEDERICO SANTA MARIA

DOCTORAL THESIS

Experimental Studies of Parton Propagation in Strongly Interacting Matter

Author:
Sebastian TAPIA

Supervisor:
Dr. William BROOKS

A thesis submitted in fulfillment of the requirements for the degree of Doctor of Philosophy

in the

Experimental Group
Physics Department

April 17, 2018

"All those who wander in darkness seek the light. But when they reach the light, they avert their eyes from the blinding glare. [...] Someday your eyes will be burned by the light of truth, and you will know eternal darkness. That is the judgement."

Kazkis, damning Vincent before dying

UNIVERSIDAD TECNICA FEDERICO SANTA MARIA

Abstract

Science Faculty
Physics Department

Doctor of Philosophy

Experimental Studies of Parton Propagation in Strongly Interacting Matter

by Sebastian TAPIA

One important area of forefront research in strong interaction physics involves understanding how the fundamental particles of Quantum ChromoDynamics (QCD), the quarks and gluons, interact in spatially extended systems. Well-known research topics in this area include the study of gluon saturation at high parton densities, and jet quenching in ultra-relativistic collisions of large atomic nuclei. While perturbative treatments of QCD (pQCD) in proton-proton collisions produce excellent descriptions of the experimental data, the QCD-based description of processes in-medium is at a much more primitive stage, and there are many outstanding questions. One example is in the area of quark energy loss in-medium. Quark energy loss has long been conceived as occurring from two processes: partonic elastic scattering, and radiation of gluons, in analogy with the well-known processes in Quantum Electrodynamics (QED). Elastic scattering is expected to play a minor role for light quarks, while it is expected to play a larger role for heavy quarks; gluon radiation is expected to be the dominant effect for light quarks, and to play a smaller role for heavy quarks. These intuitive expectations have been validated by explicit pQCD calculations in numerous studies. However, a comparison of light quark observables to heavy quark observables does not currently appear to conform to these expectations at all. As an example, b-quark jets appear to demonstrate the same suppression in heavy ion collisions as light-quark jets in studies at the Large Hadron Collider (LHC). We propose to study heavy quark suppression using data from the ATLAS detector at the LHC. The experimental technique of choice is to measure J/ψ mesons in heavy ion collisions, comparing their production characteristics with those seen in proton-proton collisions, where no medium is present. To isolate the b-quark component, we focus on J/ψ mesons with a measured detached vertex relative to the primary collision vertex. The b quarks predominantly decay into J/ψ mesons long after they are produced, and thus these mesons serve as a proxy for the primordial heavy quarks passing through the medium. Since any suppression seen in heavy ion collisions is the result of attenuation of b-quarks in the hot, dense medium formed in those collisions, it is also of interest to compare these results to the same process as observed in cold matter, such as the system produced in p+Pb collisions at the LHC. Further comparisons to cold matter can be performed in electron-nucleus interactions, where the interaction of virtual photons provides a probe that is free of initial-state interactions. Studies of this kind can be carried out with light-quark signals using data from the EMC, HERMES, and CLAS experiments. Inter-comparison of the results found from these different types of systems will provide new insights into the emerging field of partonic interactions within systems of strongly interacting particles.

Acknowledgements

To CONICYT, DGIIP and CCTVAL for support my studies.
Thanks to my advisor William Brooks for his guide, my friends for useful discussions and my family.

Contents

List of Figures

List of Tables

Chapter 1

Introduction

Three decades ago, Matsui and Satz first suggested that charmonia, bound states of c and $\bar{c}$ quarks, could be a sensitive probe to study the hot, dense system created in nucleus-nucleus (A+A) collisions [55]. In their work, they postulated that Debye screening of the quark colour charge in a hot plasma would tend to prevent the formation of a quarkonium bound state in the medium, such as J/ψ and $\psi(2S)$, when the Debye length becomes smaller than the quarkonium binding radius. Therefore the impact of medium effects on the quarkonia production should be significantly larger for ψ (2S) than for J/ψ because the smaller binding energy makes the dissociation in the medium easier. This is referred to as sequential melting [37, 46]. Thus, the suppression of different quarkonium states could provide information related to the temperature and degree of deconfinement of the medium formed in heavy ion collisions.

Since then, there have been numerous experimental and theoretical investigations that have demonstrated that other effects are also present in addition to colour screening in a deconfined plasma [52, 26, 9]. First, it has been shown that over a wide range of interaction energies there is already a modification in the production of J/ψ mesons in systems where a large volume of quark-gluon plasma does not appear to form, such as in proton-nucleus collisions [42, 54, 1]. Second, it has been shown by the ALICE Collaboration that not only a suppression of quarkonia is observed in ion-ion collisions [18, 35, 59, 51], but an enhancement is also observed at low transverse momentum, p_{T}, relative to production in proton-proton (pp) collisions [4, 6]. This observation has led to the interpretation that recombination of charm quarks and anti-quarks from the medium can play a role by providing an additional mechanism of quarkonium formation [66, 27]. Finally, similarities in the J/ψ suppression with charge hadrons and D-mesons suggest that high p_{T} J/ψ's may also be sensitive to parton energy loss in the medium [65, 10]. At LHC energies, J/ψ production originates not only from the immediate formation of the composite $c\bar{c}$ bound state (prompt J/ψ), but also from the decay of b-hadrons that result in a decay vertex separated from the collision vertex by a few milimeters (non-prompt J/ψ). When a secondary vertex can be identified using the precise tracking system of the ATLAS experiment [12], it offers the intriguing possibility of using J/ψ production to study the propagation of b-quarks in the hot dense medium, as not hadronization is expected inside of the hot medium[48]. Suppression of the production of b-hadrons in the medium, in the most naive picture, is caused by a completely different phenomenon from the suppression of $c\bar{c}$ bound states. While $c\bar{c}$ bound state formation may be inhibited by colour screening from a hot and deconfined medium,

the suppression of high-p_{T} b-quark production is commonly attributed to energy loss of propagating b-quarks by collisional and/or radiative processes [29], not necessarily suppressing the total cross section but more likely shifting the yield to a lower p_{T}. Modification of the b-hadrons formation, or their decay products, may also play a role, particularly from a quantum mechanical perspective [49]. In any case, there is no reason to expect a modification of prompt J/ψ production to be similar to the modification of non-prompt J/ψ production, since quite different mechanisms are expected to contribute to those two classes of final states [9]. Simultaneous measurements of prompt and non-prompt charmonia are therefore essential for understanding the physics mechanisms of charmonium suppression in heavy ion collisions.

Chapter 2

Theorical Foundations

2.1 Quantum chromodynamics (QCD)

2.1.1 The QCD Lagrangian

The QCD Lagrangian is given by:

$$\mathcal{L} = -\frac{1}{4}\mathcal{F}_{A}^{\beta\alpha}\mathcal{F}_{\beta\alpha}^{A} + \sum \bar{q}_a(i\hat{D} - m)_{ab}q_b \tag{2.1}$$

This Lagrangian density describes the interaction of spin-1/2 quarks of mass m and massless spin-1 gluons. $\mathcal{F}_{A}^{\beta\alpha}$ is the field strength tensor derived from field $\mathcal{A}_{\alpha}^{A}$,

$$\mathcal{F}_{A}^{\beta\alpha} = \partial_\alpha \mathcal{A}_{\beta}^{A} - \partial_\beta \mathcal{A}_{\alpha}^{A} - g f^{ABC}\mathcal{A}_{\alpha}^{B}\mathcal{A}_{\beta}^{C} \tag{2.2}$$

and the indices A,B,C run over the eight colour degrees of freedom of the gluon field. It is the third 'non-abelian' term on the right-hand-side of Eq 2.2 which distinguishes QCD from QED, giving rise to triplet and quadratic gluon self-interactions and ultimately to the property of asymptotic freedom.
The sum over flavours runs over the n_f different flavours of quarks, g is the coupling constant which determines the strength of the interaction between coloured quanta, and f^{ABC} (A,B,C = 1,..,8) are the structure constants of the SU(3) colour group. The quarks fields q_a are in the triplet representation of the colour group, (a = 1,2,3) and $\mathcal{D}$ is the covariant derivative, Acting on triplet and octet fields the covariant derivative takes the from

$$(\mathcal{D}_\alpha)_{ab} = \partial_\alpha \delta_{ab} + ig(t^C \mathcal{A}_{\alpha}^{C})_{ab}, (\mathcal{D}_\alpha)_{AB} = \partial_\alpha \delta_{AB} + ig(T^C \mathcal{A}_{\alpha}^{C})_{AB} \tag{2.3}$$

where t and T are matrices in the fundamental and adjoint representations of SU(3) respectively:

$$[t^A, t^B] = if^{ABC}t^C, [T^A, T^B] = if^{ABC}T^C, (T^A)_{BC} = -if^{ABC} \tag{2.4}$$

$\hat{D}$ in Eq. 2.1 is a symbolic notation for $\gamma_\mu D^\mu$ and the spinor indices of γ_μ and q_a have been suppressed. Otherwise we follow the notation of Bjorken and Drell, ("Relativistic Quantum Fields", 1964) with metric given by $g^{\alpha\beta}$ = diag(1,-1,-1,-1) and set $\hbar$ = c = 1. By convention the normalisation of the SU(N) matrices is chosen to be,

$$Trt^A t^B = T_R \delta^{AB}, \;\; T_R = \frac{1}{2} \tag{2.5}$$

With this choice the SU(N) colour matrices obey the following relations,

$$t^A_{ab}t^A_{bc} = C_F\delta_{ab}, C_F = \frac{N^2-1}{2N} = \frac{4}{3}, (N=3) \tag{2.6}$$

$$TrT^CTD = f^{ABC}f^{ABD} = C_A\delta^{CD}, C_a = N = 3 \tag{2.7}$$

We cannot perform perturbation theory with the Lagrangian of Eq. 2.1 without the gauge fixing term. It is impossible to define the propagator for the gluon field without making a choice of gauge. The choice,

$$\mathcal{L}_{gauge-fixing} = -\frac{1}{2\lambda}(\partial^\alpha \mathcal{A}^{\mathcal{A}}_\alpha)^\in, \tag{2.8}$$

fixes the class of covariant gauges and λ is the gauge parameter. In a non-abelian theory such as QCD this covariant gauge-fixing term must be supplemented by a ghost Lagrangian, which is given by

$$\mathcal{L}_{ghost} = \partial_\alpha \eta^A (D^\alpha_{AB}\eta^B). \tag{2.9}$$

here η^A is a complex scalar field which obeys Fermi statistics. The derivation of the form of the ghost Lagrangian is best provided by the path integral formalism and the procedures due to Fadeev and Popov, (Phys. Lett. 258 (1977) 377). The ghost fields cancel un physical degrees of freedom which would otherwise propagate in covariant gauge.

2.1.2 The Feynman rules

The Feynman rules are defined from the action operator $\phi = i\int \mathcal{L}d^4x$ rather than form the Lagrangian density. We can separate the effective Lagrangian into a free piece $\mathcal{L}_\prime$, which normally contains all the terms bilinear in the fields, and an interaction piece, $\mathcal{L}_\mathcal{I}$, which contains all the rest:

$$\Phi = \Phi_0 + \Phi_I$$
$$\Phi_0 = i\int d^4x\mathcal{L}_0(x), \quad \Phi_I = i\int d^4x\mathcal{L}_I(x) \tag{2.10}$$

The practical recipe to determine the Feynman rules is that the inverse propagator is derived from $-\Phi_0$, whereas the Feynman rules for the interacting parts of the theory which are treated as perturbations are derived from Φ_I.
This recipes (including the extra minus sign) can be understood by considering the following two different approaches to the quantisation of a theory. For simplicity, consider a theory which contains only a complex scalar field ϕ and an action which contains only bilinear terms, Φ = ϕ^*(K+K')ϕ. In the first approach, both K and K' are included in the free Lagrangian, Φ_0 = ϕ^*(K+K')ϕ .Using the above rule the propagator $\triangle$ for the ϕ field is given by

$$\triangle = \frac{-1}{K+K'} \tag{2.11}$$

In the second approach K is regarded as the free Lagrangian, $\Phi_0 = \phi^*K\phi$, and K' as the interaction Lagrangian, $\Phi_I = \phi^*K'\phi$. Now Φ_I is included to all orders in perturbation theory by inserting the interaction term an infinite

number of times:

$$\triangle = \frac{-1}{K} + (\frac{-1}{K})K'(\frac{-1}{K}) + (\frac{-1}{K})K'(\frac{-1}{K})K'(\frac{-1}{K}) + ... = \frac{-1}{K+K'} \tag{2.12}$$

Using the free piece of $\mathcal{L}_0$ of the QCD Lagrangian given in Eq. 2.10 one can readily obtain the quark and gluon propagator. Thus, for example, the inverse fermion propagator in momentum space can be obtained by making the identification $\partial^\alpha = -ip^\alpha$ for an incoming field. In momentum space the two point function of the quark field depends on a single momentum p. It is found to be

$$\Gamma^{(2)}_{ab}(p) = -i\delta_{ab}(\hat{p} - m), \tag{2.13}$$

which is the inverse of the propagator given in table 1. The $i\epsilon$ prescription for the pole of the propagator is added to preserve causality, in exactly the same way as in QED. Similar the inverse propagator of the gluon field is found to be

$$\Gamma^{(2)}_{\{AB,\alpha,\beta\}}(p) = i\delta_{AB}\left[p^2 g_{\alpha\beta} - (1 - \frac{1}{\lambda})p_\alpha p_\beta\right] \tag{2.14}$$

It is straightforward to check that without the gauge fixing term this function would have no inverse. The result for the gluon propagator $\triangle$ is as given in figure (2.1):

$$\Gamma^{(2)}_{\{AB,\alpha,\beta\}}(p)\ \triangle^{(2)\{BC,\beta,\gamma\}}(p) = \delta^C_A g^\gamma_\alpha \tag{2.15}$$

$$\triangle^{(2)}_{\{BC,\beta,\gamma\}}(p) = \delta_{BC}\frac{i}{p^2}\left[-g_{\beta\gamma} + (1-\lambda)\frac{p_\beta p_\gamma}{p^2}\right]. \tag{2.16}$$

Replacing derivatives with the appropriate momenta, Eqs. 2.1, 2.8 and 2.9 can be used to derive all the rules in figure (2.1).

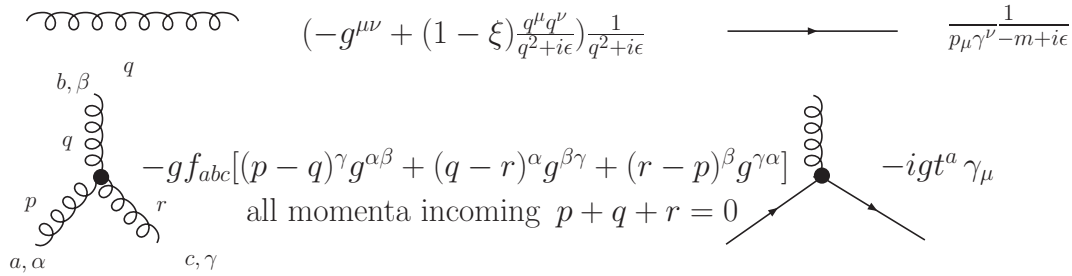

FIGURE 2.1: Feynman rules

2.1.3 The QCD running coupling

In order to introduce the concept of the running coupling, consider as an example a dimensionless physical observable R which depends on a single energy scale Q. By assumption the scale Q is much bigger than all other dimensional parameters such as masses. We shall therefore set the masses to zero. (This step requires the additional assumption that R has a sensible zero mass limit.) Naive scaling would suggest that because there is a single large scale, R should have a constant value independent of Q. This result is

not however true in a renormalisable quantum field theory. when we calculate R as a perturbation series in the coupling $\alpha_S = \frac{g^2}{4\pi}$, (defined in analogy with the fine structure constant of QED), the perturbation series requires renormalisation to remove ultra-violet divergences. Because this renormalisation procedure introduces a second mass scale μ - the point at which the subtraction which remove the ultra-violet divergences are performed - R depends in general on the ratio $\frac{Q}{\mu}$ and is not, therefore, constant. It follows also that the renormalised coupling α_S depends on the choice made for the subtraction point μ.
However μ is an arbitrary parameter. The Lagrangian of QCD makes no mention of the scale μ, even though a choice of μ is required to define the theory at the quantum level. Therefore, if we hold the bare coupling fixed, physical quantities such as R cannot depend on the choice made for μ. Since R is dimensionless, it can only depend on the ratio $\frac{Q^2}{\mu^2}$ and the renormalised coupling α_S. Mathematically, the μ dependence of R may be quantified by

$$\mu^2 \frac{d}{d\mu^2} R(\frac{Q^2}{\mu^2}, \alpha_S) \equiv \left[\mu^2 \frac{\partial}{\partial \mu^2} + \mu^2 \frac{\partial \alpha_S}{\partial \mu_S} \frac{\partial}{\partial \alpha_S} \right] R = 0. \tag{2.17}$$

To rewrite this equation in a more compact form we introduce the notations

$$t = ln(\frac{Q^2}{\mu^2}), \quad \beta(\alpha_S) = \mu^2 \frac{\partial \alpha_S}{\partial \mu^2}, \tag{2.18}$$

and rewrite Eq. 2.17 as

$$\left[-\frac{\partial}{\partial t} + \beta(\alpha_S) \frac{\partial}{\partial \alpha_S} \right] R = 0. \tag{2.19}$$

this first order partial differential equation is solved by implicitly defining a new function - the running coupling α_S(Q) - as follows:

$$t = \int_{\alpha_S}^{\alpha_S(Q)} \frac{dx}{\beta(x)}, \quad \alpha_S(\mu) \equiv \alpha_S. \tag{2.20}$$

By differentiating Eq. 2.20 we can show that

$$\frac{\alpha_S(Q)}{\partial t} = \beta(\alpha_S(Q)), \quad \frac{\partial \alpha_S(Q)}{\partial \alpha_S} = \frac{\beta(\alpha_S(Q))}{\beta(\alpha_S)}. \tag{2.21}$$

and hence that R(1,$\alpha_S(Q)$) is a solution of Eq. 2.19. The above analysis shows that all of the scale dependence in R enters through the running of the coupling constant $\alpha_S(Q)$. It follows that knowledge of the quantity R(1,α_S), calculated in fixed order perturbation theory, allows us to predict the variation of R with Q if we can solve Eq. 2.20. Now we will show that QCD is an asymptotically free theory. This means that $\alpha_S(Q)$ becomes smaller as the scale Q increases. For sufficiently large Q, therefore, we can always solve Eq. 2.20 using perturbation theory.

2.1.4 The beta function and the Λ parameter in QCD

The running of the coupling constant α_S is determined by the renormalisation group equation. In QCD, the β function has the perturbative expansion

$$\begin{gathered}\beta(\alpha_S) = -b\alpha_S^2(1 + b'\alpha_S + O(\alpha_S^2)) \\ b = \frac{(33 - 2n_f)}{12\pi}, \quad b' = \frac{(153 - 19n_f)}{2\pi(22 - n_f)},\end{gathered} \tag{2.22}$$

where n_f is the number of active light flavours. From Eq. 2.21 we may write,

$$\frac{\partial\alpha_S(Q)}{\partial t} = -b\alpha_S^2(Q)\left[1 + b'\alpha_S(Q) + O(\alpha_S^2(Q))\right]. \tag{2.23}$$

Neglecting the b' and higher coefficients in Eq. 2.23 gives the solution

$$\alpha_S(Q) = \frac{\alpha_S(\mu)}{1 + \alpha_S(\mu)bt}, \quad t = ln(\frac{Q^2}{\mu^2}). \tag{2.24}$$

This gives the relation between $\alpha_S(Q)$ and $\alpha_S(\mu)$, if both are in the perturbative region. Evidently as t become very large, the running coupling $\alpha_S(Q)$ decreases to zero. This is the property of *asymptotic freedom*. The approach to zero is rather slow since α_S only decreases like an inverse power of $logQ^2$. Notice that the sign of b is crucial. With the opposite sign of b the coupling would $increase$ at large Q^2, as it does in QED. Perturbative QCD tells us how the coupling constant varies with the scale, not the absolute value itself. The latter has to be obtained from experiment. Thus we can choose as 'the' fundamental parameter of the theory the value of the coupling constant at a convenient reference scale which is large enough to be in the perturbative domain, M_Z^2 for example. Setting $\mu = M_Z$ in Eq. 2.24, we can then deduce the value at any other large scale Q^2.
An alternative approach, which was adopted historically and is still convenient for many purposes, is to introduce a dimensional parameter directly into the definition of $\alpha_S(Q^2)$. By convention this parameter is called Λ and is the constant of integration defined by

$$ln\frac{Q^2}{\Lambda^2} = -\int_{\alpha_S(Q^2)}^{\infty}\frac{dx}{\beta(x)} = \int_{\alpha_S(Q^2)}^{\infty}\frac{dx}{bx^2(1 + b'x + ...)}. \tag{2.25}$$

Λ represents ths scale at which the coupling would diverge, if extrapolated outside the perturbative domain. More qualitatively, it indicates the order of magnitude of the scale at which $\alpha_S(Q^2)$ becomes strong. Depending on the precise definition its value is in the neighbourhood of 300 MeV. Thus $\alpha_S(Q^2)$ becomes large, and perturbation theory breaks down, for scales comparable with the masses of the light hadrons, i.e. Q $\simeq$ 1 GeV. This could be an indication that the $confinement$ of quarks and gluons inside hadrons is actually a consequence of the growth of the coupling at low scales, which is a corollary of the decrease at high scales that leads to asymptotic freedom. The introduction of Λ allows us to write the asymptotic solution for α_S in terms of this parameter. In leading order (LO), i.e retaining only the b coefficient in the β function, we can perform the integration in Eq. 2.25 to obtain

$$\alpha_S(Q^2) = \frac{1}{b \ln(\frac{Q^2}{\Lambda^2})} \tag{2.26}$$

We can see how α_S looks in the figure (2.2)

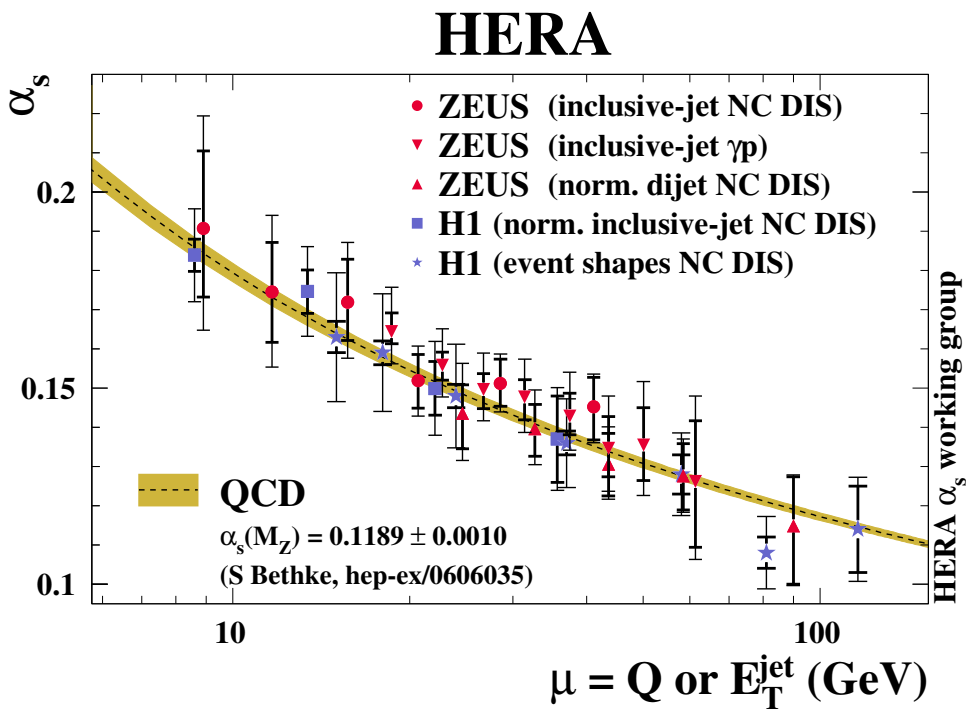

FIGURE 2.2: The experimental data on running QCD coupling from deep inelastic scattering (DIS) experiments at HERA. The dashed line with a band around it is the theoretical expectation for the strong coupling.

2.1.5 QCD phase diagram

Thermodynamic properties of a system are most readily expressed in terms of a phase diagram in the space of thermodynamic parameters, in the case of QCD, as a temperature T and baryo-chemical potential μ_B phase diagram.
After the discovery of the asymptotic freedom [61, 43], the existence of a deconfined state of quarks and gluons was predicted at high temperature and/or high pressures [28, 36]. At sufficiently high temperatures, quarks and gluons interact weakly and the system will behave as an ideal ultra-relativistic gas. The degrees of freedom will be then determined by the flavor numbers, spin states, color and charge states of the quarks and gluons. The deconfined state was called later quark gluon plasma [63] (QGP). One open question after the discovery of the asymptotic freedom, concerned the properties of the transition from the hadron gas to the QGP: does it take place smoothly or via a phase transition and exhibiting critical behaviours?. Several studies has been done theoretically and base in Lattice calculations, the most important features are summarised as follow:

- **From chiral symmetry restoration**:
  At sufficiently high temperature $T \gg \Lambda_{\text{QCD}}$, due to the asymptotic

freedom of QCD, perturbation theory around the approximation of the QGP should become applicable. In this regime, $m_u = m_d = 0$, the Lagrangian of QCD acquires chiral symmetry $SU(2)_L \times SU(2)_R$, corresponding to SU(2) flavour rotations of (u_L, d_L) and (u_R, d_R) doublets independently. The ground state of QCD breaks the chiral symmetry spontaneously; this is a non-perturbative phenomenon. A transition from a broken chiral symmetry vacuum state to a chirally symmetric equilibrium state at some temperature $T_C \sim \Lambda_{QCD}$ should be expected.

- **Pisarski and Wilczek [60]**:
  The transition cannot be of second order for three massless quarks.

- **Crossover**:
  The second order transition requires tuning chiral symmetry breaking parameters (quark masses) to zero. In the absence of the exact chiral symmetry (broken by quark masses) the transition from low to high temperature phases of QCD need not proceed through a singularity. Lattice simulations do indeed show that the transition is a crossover for $\mu = 0$.

- **Critical point**:
  The first order transition line is now ending at a point known as the QCD critical point or end point. This is a common feature most liquids, including water. The line which we know as the water boiling transition ends at pressure $p = 218$ atm and $T = 374$ C. In QCD the two coexisting phases are hadron gas (lower T), and quark-gluon plasma (higher T). What distinguishes the two phases?

Figure 2.3 show the contemporary pictorial description of the QCD phase diagram as is today conceived.

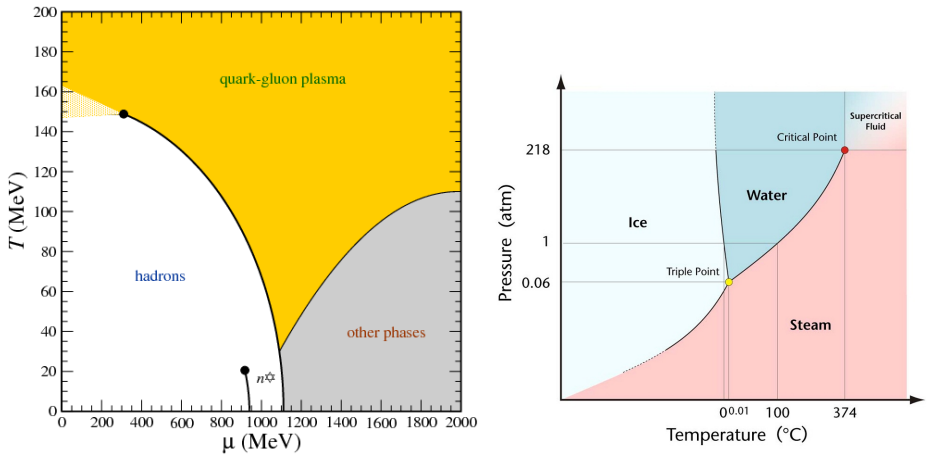

FIGURE 2.3: (Left) Lay-out of the hadronic matter phase diagram as it is today conceived [50], (Right) phase diagram of water.

2.2 Charmonia as probe of dense matter

As the transition to the QGP only concerns the light quarks u, d and s, for which the chiral symmetry is a good approximation and heavy quarks explicitly break the chiral symmetry, they are not directly concerned by the transition to QGP. In other words, the bound states of heavy quarks (quarkonia) are not necessarily melt in a QGP and they could exist as bound states. For this reason, these bound states become very interesting probes for measuring the temperature of the QGP [55]. The QGP could also be studied via its tomography using high energy partons. QCD predicts that high energy partons will lose energy via gluon radiation when crossing the QGP. Recently similarities found in the J/ψ suppression with charge hadrons and D-mesons suggest that high p_{T} J/ψ's may also be sensitive to parton energy loss in the medium [65, 10].

Screening of the colour potential

In vacuum, the quarkonium spectrum can be described via non relativistic models based on a potential interaction like:

$$V(r) = \sigma r - \frac{\alpha}{r} \tag{2.27}$$

where α represents the string tension of the $q\bar{q}$-pair and α is a Coulombian-like constant [55].
If the $q\bar{q}$ state is embedded in a QGP at a temperature T, the interaction potential between the heavy quarks will be affected by the presence of the free colour charges in the QGP. This is the screening of the potential. In the plasma, assuming that the potential is only Coulombian ($\sigma = 0$), potential has to be replaced by a potential with a screening constant:

$$V(r) = -\frac{\alpha}{r} \times e^{-r/\lambda_D} \tag{2.28}$$

where λ_D is the Debye length. Let us assume that the average distance between the quarks in a 1S state (J/ψ or $\Upsilon(1S)$) can be estimated by the Bohr radius expression:

$$r_B = \frac{1}{\alpha m_Q} \tag{2.29}$$

In the case of J/ψ, $m_Q = m_c = 1.25$ GeV and $\alpha(m_c) = 0.36$, so $r_B = 0.44$ fm. For the $\Upsilon(1S)$, $m_Q = m_b = 4.2$ GeV and $\alpha(m_b) = 0.22$, so r_B = 0.22 fm.
If $r_B \ll \lambda_D$, the potential between the heavy quarks can be considered as a Coulombian potential and the bound state exhibits the same properties in the QGP as in the vacuum. However, if $r_B \geq \lambda_D$, the quarkonium properties will be modified by the medium, and it could happen that the quarkonium becomes an unstable state and therefore would melt, pictorial representation is shown in figure 2.4. For electromagnetic plasmas, the Debye length depend on the temperature of the plasma and the charge density ρ:

$$\lambda_D = \sqrt{\frac{T}{8\pi\alpha\rho}} \tag{2.30}$$

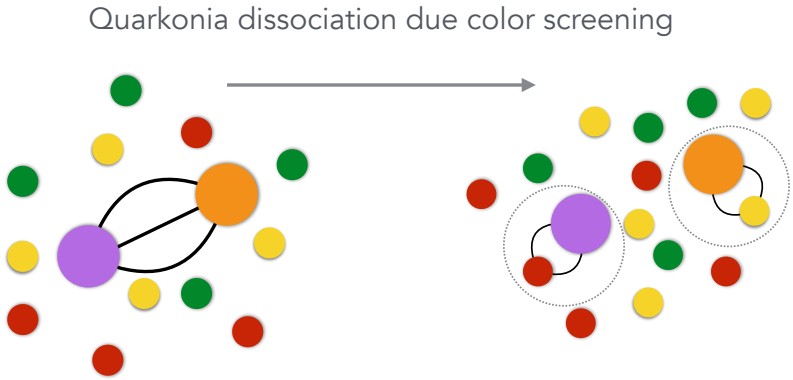

FIGURE 2.4: Representation of color screening.

Assuming that the previous expression is also valid for the QGP and an ideal ultra-relativistic gas $\rho \propto T^3$, one obtains :

$$\lambda_D = \frac{1}{\sqrt{8\pi\alpha T}} \tag{2.31}$$

And therefore, the quarkonia could be melt for temperature above T_d;

$$T_d = \frac{1}{\sqrt{8\pi\alpha(T) r_B}} \tag{2.32}$$

For $\alpha(T) \sim 0.2$, one obtains that $T_d \sim 200$ MeV $(1.3T_c)$ for the J/ψ and $T_d \sim 400$ MeV $(2.6T_c)$ for the $\Upsilon(1S)$. Assuming that for 2S states the r_B would be twice larger, one would conclude that the dissociation temperature for $\psi^{'}$ is $\leq T_c$ and for $\Upsilon(2S)$ similar to that of J/ψ. This explains why $\psi(2S)$ resonance is easily melt with respect to J/ψ and why $\Upsilon(1S)$ would melt at higher temperatures than that of J/ψ.

Parton - QGP interaction

QCD predictions tell that the formation length of the radiated gluon will be larger than the average distance between the gluons in the QGP. As a consequence several interaction centres will participate in the gluon emission from the parton, and the amplitude from the interaction centres will interfere (this phenomenon is called Landau-Migdal-Pomeranchuck effect) since the radiated gluon will be coherently emitted along all its formation length. For this reason, for a QGP thicknesses about $1-3$ fm, the ΔE should be proportional to the square of the transversed path length in the QGP [23, 69]:

$$\Delta E \sim \alpha_S \times C_R \times \bar{q}(\rho_g) \times L^2 \tag{2.33}$$

where α_s is the strength of the strong interaction, C_R is the colour charge factor $\hat{q}$ is the transport coefficient which depends on the gluon density (ρ_g) of the QGP and L is the thickness of the QGP.
The energy lost will depend on the nature of the parton:

- Gluons will exhibit larger energy-loss per unit of length than that of quarks. A relative factor $9/4$ due to the colour charge, is associated to the gluonsstrahlung mechanism from a gluon with respect to that from a quark.
- Heavy quarks are expected to lose less energy than light quarks, due to the absence of gluon radiation at forward angles, below $\theta < M/E$, where M is the quark mass and E its energy [38]. This phenomenon, predicted by the QCD, is called dead-cone effect. The dead-cone effect should become measurable for beauty quarks, whereas this effect should remain relatively small for charm quarks. Moreover, elastic collisions with partons in the QGP could also contribute to the energy-loss of heavy quarks in the QGP.

2.2.1 Quarkonium production

The theoretical study of quarkonium production processes involves both perturbative and non-perturbative aspects of QCD. On one side, the production of the heavy-quark pair, $q\bar{q}$, which will subsequently form the quarkonium, is expected to be perturbative since it involves momentum transfers at least as large as the mass of the considered heavy quark. On the other side, the evolution of the $q\bar{q}$ pair into the physical quarkonium state is non-perturbative, over long distances, with typical momentum scales such as the momentum of the heavy-quarks in the bound-state rest frame, $\mathrm{m}_q v$ and their binding energy $\mathrm{m}_q v^2$, v being the typical velocity of the heavy quark or antiquark in the quarkonium rest frame ($v^2 \approx 0.3$ for the charmonium and 0.1 for the bottomonium). In nearly all the models or production mechanisms discussed nowadays, the idea of a factorisation between the pair production and its binding is introduced. Different approaches differ essentially in the treatment of the hadronisation, although some may also introduce new ingredients in the description of the heavy-quark-pair production. In the following, we briefly describe three of them which can be distinguished in their treatment of the non-perturbative part: the Colour-Evaporation Model (CEM), the Colour-Singlet Model (CSM), the Colour-Octet Mechanism (COM), the latter two being encompassed in an effective theory referred to as Non-Relativistic QCD (NRQCD), figure 2.5 shows diagram examples of single and octet production.

Colour-Evaporation Model

The cross section to produce a given quarkonium state is then supposed to be obtained after a multiplication by a phenomenological factor F_Q related to a process-independent probability that the pair eventually hadronises into this state. One assumes that a number of non-perturbative-gluon emissions occur once the $q\bar{q}$ pair is produced and that the quantum state of the pair at its hadronisation is essentially decorrelated, at least colour-wise, with that at its production. From the reasonable assumption [8] that one

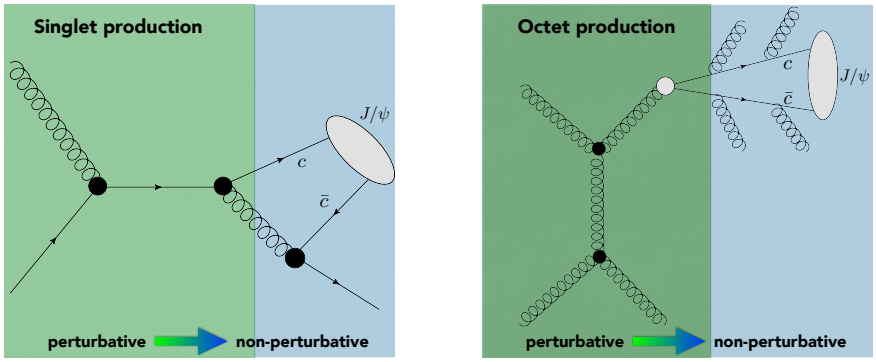

FIGURE 2.5: Example of singlet (left) and octet (right) J/ψ production diagrams.

ninth, one colour-singlet $q\bar{q}$ configuration out of nine possible, of the pairs in the suitable kinematical region hadronises in a quarkonium, a simple statistical counting [8] was proposed based on the spin J_Q of the quarkonium Q, $F_Q = 1/9x(2J_Q+1)/\sum_i(2J_i+1)$, where the sum over i runs over all the charmonium states below the open heavy-flavour threshold.
Mathematically, one has

$$\sigma_Q^{(N)LO} = F_Q \int_{2m_Q}^{2m_H} \frac{d\sigma_{q\bar{q}}^{(N)LO}}{dm_{q\bar{q}}} dm_{q\bar{q}} \tag{2.34}$$

In the latter formula, a factorisation between the short-distance $q\bar{q}$-pair production and its hadronisation is the quarkonium state is of course implied although it does not rely on any factorisation proof. In spite of this, this model benefits from a successful phenomenology but for the absence of predictions for polarisation observables and discrepancies in some transverse momentum spectra.

Colour-Singlet Model

Th model relies on the assumption that the quantum state of the pair does not evolve between its production and its hadronisation, neither in spin, nor in colour. Assuming that the quarkonia are non-relativistic bound states, the partonic cross section for quarkonium production can be expressed as that for the production of heavy-quar pair with zero relative velocity, ν, in a color-singlet state and in the same angular-momentum and spin as that the quarkonia that will be produced, and the square of the Schrödinger wave function at the origin in the position space.
In the case of hadroproduction, the hadronic cross section can we written as following:

$$d\sigma[Q+X] = \sum_{ij} \int dx_i dx_j f_i(x_i,\mu_F) f_j(x_j,\mu_F) \times d\hat{\sigma}_{i+j\to(q\bar{q})+X}(\mu_R,\mu_F)|\psi(0)|^2 \tag{2.35}$$

where the parton distribution functions (PDF), i and j, of the colliding hadrons, $f_{ij}(x)$ and the absolute value of the color singlet $c\bar{c}$ wave function, ψ, needs be determined from data or models. Once these quantities are provided, CSM becomes fully predictive and has no free parameters.

Colour-Octet Mechanism

In this model the hadronisation probability of a heavy-quark pair into a quarkonium is expressed via long-distance matrix elements (LDMEs). In addition to the expansion in powers of α_s, NRQCD further introduces an expansion in v. It is then natural to account for the effect of higher-Fock states (in v) where the $q\bar{q}$-pair is in an octet state with a different angular-momentum and spin states. The consideration of the leading Fock state (in v) amounts to the CSM, which is thus a priori the leading NRQCD contribution (in v). However, this opens the possibility for non-perturbative transitions between these coloured states and the physical meson. One of the virtues of this is the consideration of $3S_1^{[8]}$ states in P-wave productions, whose contributions cancel the infra-red divergences in the CSM. As compared to the Eq. 2.36, one has to further consider additional quantum numbers (angular momentum, spin and colour), generically denoted n, involved in the production mechanism:

$$d\sigma[Q+X] = \sum_{ijn} \int dx_i dx_j f_i(x_i, \mu_F) f_j(x_j, \mu_F) \times d\hat{\sigma}_{i+j\to(q\bar{q})_n+X}(\mu_R, \mu_F, \mu_\Lambda) \langle \Theta_Q^n \rangle \tag{2.36}$$

Instead of the Schrödinger wave function at the origin squared, the former equation involves the LDMEs, $\langle \Theta_Q^n \rangle$ and a non-physical scale μ_Λ .

Chapter 3

ATLAS Experiment

3.1 The lead journey to a collision

Linear accelerator 3 (Linac 3) is the starting point for the ions used in experiments at CERN. It provides lead ions for the Large Hadron Collider (LHC) and for fixed-target experiments. Linear accelerators use radio-frequency cavities to charge cylindrical conductors. The ions pass through the conductors, which are alternately charged positive or negative. The conductors behind them push particles and the conductors ahead of them pull, causing the particles to accelerate. Superconducting magnets ensure the ions remain in a tight beam.
After Linac 3 lead ions goes into the Low Energy Ion Ring (LEIR), which prepares them for injection into the LHC. Linac 3 uses up about 500 milligrams of lead per two weeks of operation. At the particles' origin and during acceleration through Linac 3, electrons are stripped away. Eventually, all of the electrons are removed and the lead is transformed into bare nuclei, which are easier to accelerate than whole ions.
LEIR receives long pulses of lead ions from Linac 3 and transforms them into the short, dense bunches suitable for injection to the Large Hadron Collider (LHC). LEIR splits each long pulse from Linac 3 into four shorter bunches, each containing 2.2x108 lead ions. It takes about 2.5 seconds for LEIR to accelerate the bunches, in groups of two, from 4.2 MeV to 72 MeV. The ions are then at a suitable energy to be passed to the Proton Synchrotron (PS) for storage. Next, the lead ions are passed from accelerator to accelerator along the CERN complex to end up at their highest energy in the LHC. The LHC uses 592 bunches of ions per beam, so it takes around 10 minutes for LEIR to provide enough for a complete fill. Figure 3.1 shows the complete CERN's accelerator complex.

3.2 The large hadron collider

The Large Hadron Collider (LHC) is the world's largest and most powerful particle accelerator. It first started up on 10 September 2008, and remains the latest addition to CERN's accelerator complex. The LHC consists of a 27 kilometre ring of superconducting magnets with a number of accelerating structures to boost the energy of the particles along the way. Inside the accelerator, two high-energy particle beams travel at close to the speed of light before they are made to collide. The beams travel in opposite directions in separate beam pipes, two tubes kept at ultrahigh vacuum. They are guided around the accelerator ring by a strong magnetic field maintained by superconducting electromagnets. The electromagnets are built

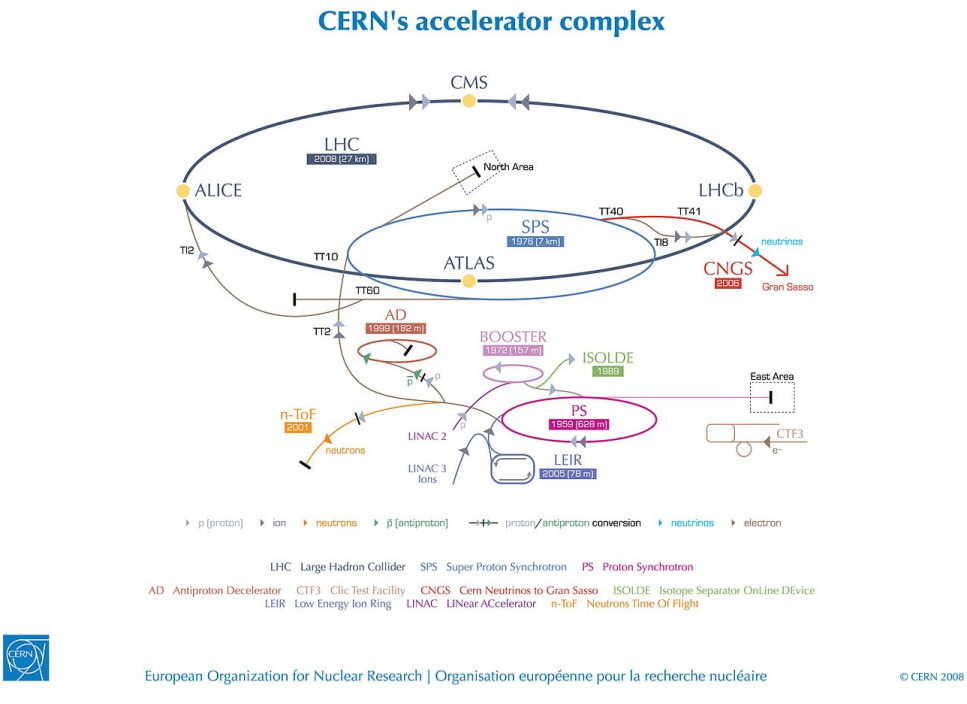

FIGURE 3.1: Cern accelerator complex.

from coils of special electric cable that operates in a superconducting state, efficiently conducting electricity without resistance or loss of energy. This requires chilling the magnets to -271.3 C a temperature colder than outer space. For this reason, much of the accelerator is connected to a distribution system of liquid helium, which cools the magnets, as well as to other supply services. Thousands of magnets of different varieties and sizes are used to direct the beams around the accelerator. These include 1232 dipole magnets 15 metres in length which bend the beams, and 392 quadrupole magnets, each 5-7 metres long, which focus the beams. Just prior to collision, another type of magnet is used to "squeeze" the particles closer together to increase the chances of collisions. The particles are so tiny that the task of making them collide is akin to firing two needles 10 kilometres apart with such precision that they meet halfway. All the controls for the accelerator, its services and technical infrastructure are housed under one roof at the CERN Control Centre. From here, the beams inside the LHC are made to collide at four locations around the accelerator ring, corresponding to the positions of four particle detectors - ATLAS, CMS, ALICE and LHCb, shown if figure 3.2.

3.3 ATLAS detector

The ATLAS detector [12] at the LHC covers nearly the entire solid angle around the collision point[1]. It consists of an inner tracking detector surrounded by a thin superconducting solenoid, electromagnetic and hadronic

[1]ATLAS uses a right-handed coordinate system with its origin at the nominal interaction point (IP) in the centre of the detector and the z-axis along the beam pipe. The x-axis points from the IP to the centre of the LHC ring, and the y-axis points upwards. Cylindrical coordinates (r, ϕ) are used in the transverse plane, ϕ being the azimuthal angle around the z-axis.

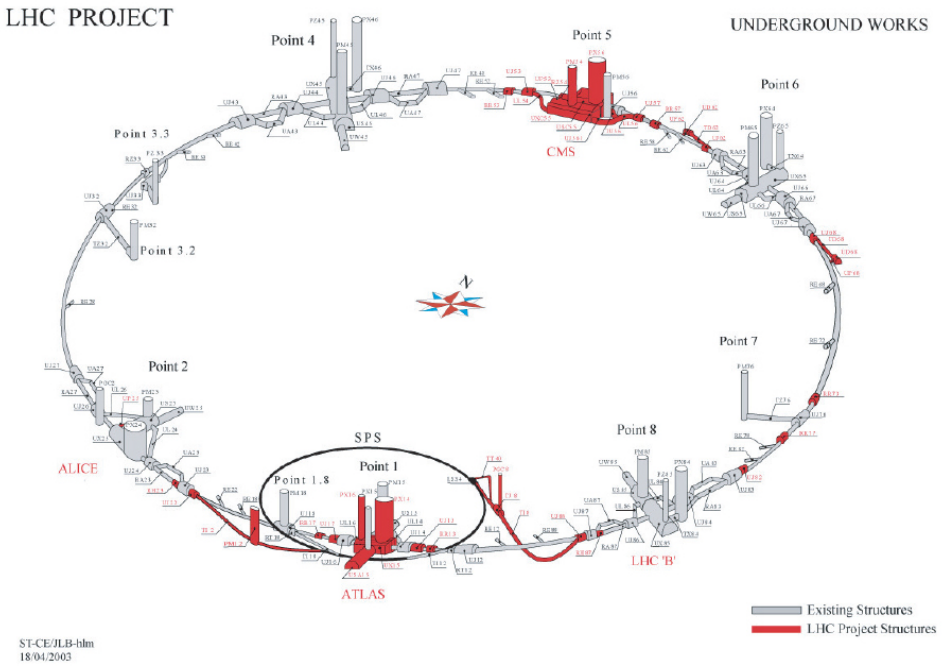

FIGURE 3.2: A schematic diagram of the LHC ring showing the locations of the four experiments.

calorimeters, and a muon spectrometer incorporating three large superconducting toroid magnets with eight coils each. Figure 3.3 shows a schematic diagram of the ATLAS detector.

3.3.1 Tracking system

The inner-detector system (ID) (figure 3.4) is immersed in a 2 T axial magnetic field and provides charged particle tracking in the pseudorapidity range $|\eta| < 2.5$. The high-granularity silicon pixel detector covers the vertex region and typically provides three measurements per track, the first hit being normally in the innermost layer. It is followed by the silicon microstrip tracker (SCT) which usually provides four two-dimensional measurement points per track. These silicon detectors are complemented by the transition radiation tracker (TRT), which enables radially extended track reconstruction up to $|\eta| = 2.0$. Since 2015 the detector contains with the presence of the Insertable B-Layer [30], an additional pixel layer close to the interaction point which provides high-resolution hits at small radius to improve the tracking and vertex reconstruction performance.

3.3.2 Calorimeter system

The calorimeter system, shown in figure 3.5, covers the pseudorapidity range $|\eta| < 4.9$. Within the region $|\eta| < 3.2$, electromagnetic calorimetry is provided by barrel and endcap high-granularity lead/liquid-argon (LAr) electromagnetic calorimeters, with an additional thin LAr presampler covering $|\eta| < 1.8$, to correct for energy loss in material upstream of the

The pseudorapidity is defined in terms of the polar angle θ as $\eta = -\ln\tan(\theta/2)$. Angular distance is measured in units of $\Delta R \equiv \sqrt{(\Delta\eta)^2 + (\Delta\phi)^2}$.

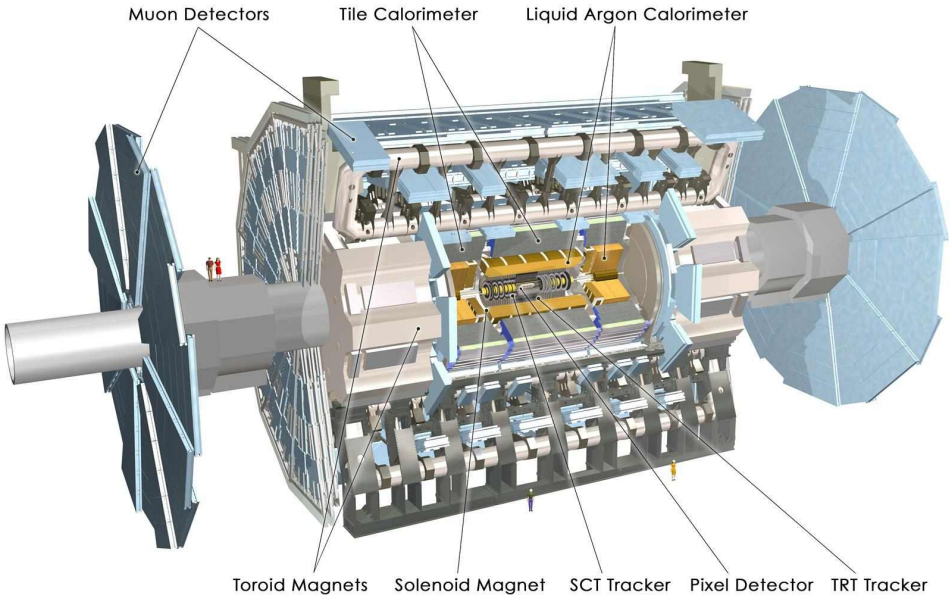

FIGURE 3.3: ATLAS detector. ATLAS Experiment © 2016 CERN.

calorimeters. Hadronic calorimetry is provided by the steel/scintillating-tile calorimeter, segmented into three barrel structures within $|\eta| < 1.7$, and two copper/LAr hadronic endcap calorimeters. The solid angle coverage is completed with forward copper/LAr and tungsten/LAr calorimeter modules optimised for electromagnetic and hadronic measurements respectively.

3.3.3 Muon system

The muon spectrometer (MS) comprises separate trigger and high-precision tracking chambers measuring the deflection of muons in a magnetic field generated by superconducting air-core toroids. The precision chamber system covers the region $|\eta| < 2.7$ with three layers of monitored drift tubes (MDT), complemented by cathode strip chambers (CSC) in the forward region, where the background is the highest. The muon trigger system covers the range of $|\eta| < 2.4$ with resistive plate chambers (RPC) in the barrel, and thin gap chambers (TGC) in the endcap regions. The arrangement of the muon chambers is shown in figure 3.6.

3.3.4 Zero-Degree Calorimeters

The primary purpose of the ATLAS Zero-Degree Calorimeters (ZDC) [45] is to detect forward neutrons with $|\eta| > 8.3$ in heavy-ion collisions. The ZDC's play a key role in the pile-up rejection of such collisions, by using the anti-correlation between the number of very forward (spectator) neutrons and the number of reconstructed charged particles (see figure 3.7). In addition to the muon trigger, two triggers are used in Pb+Pb collisions to select minimum-bias events for the centrality analysis. These are based on the presence of a minimum amount of transverse energy in all sections of

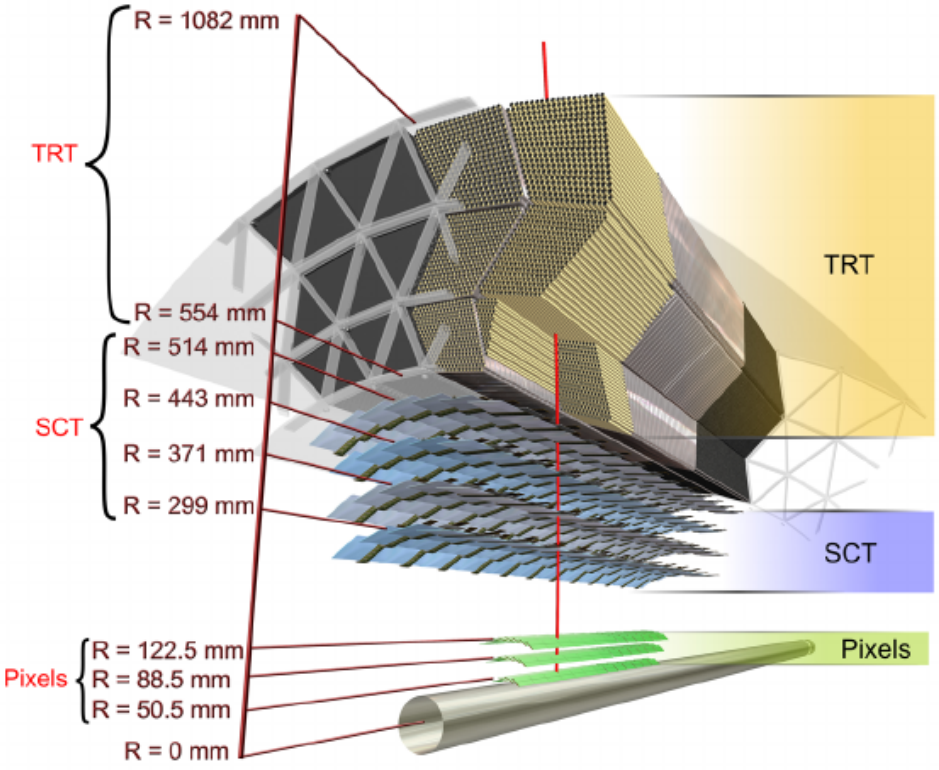

FIGURE 3.4: ATLAS tracking system. ATLAS Experiment © 2016 CERN.

the calorimeter system ($|\eta| < 3.2$) or, for events which do not meet this condition, on the presence of substantial energy deposits in both zero-degree calorimeters (ZDCs). It is located at ± 140 m from the interaction point, just beyond the point where the common straight-section vacuum-pipe divides back into two independent beam-pipes. The ZDC modules consist of layers of alternating quartz rods and tungsten plates which will measure neutral particles at pseudorapidities $|\eta| > 8.3$.

3.3.5 Trigger System

A two-level trigger system is used to select events of interest [21]. The Level-1 (L1) trigger is implemented in hardware and uses a subset of detector information to reduce the event rate to a design value of at most 100 kHz. This is followed by a software-based trigger levels, the High Level Trigger (HLT), which reduce the event rate to a maximum value of 1 kHz.

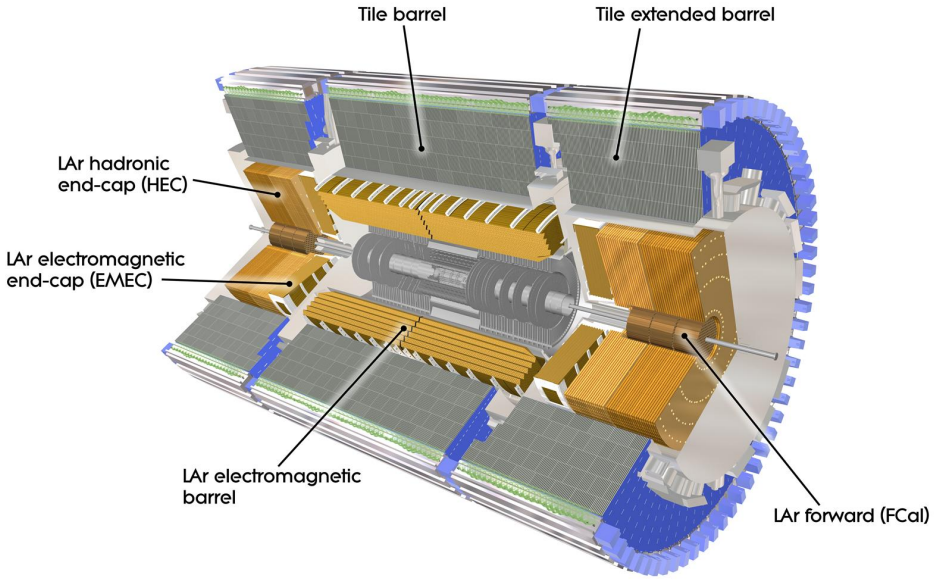

FIGURE 3.5: ATLAS calorimeter system. ATLAS Experiment © 2016 CERN.

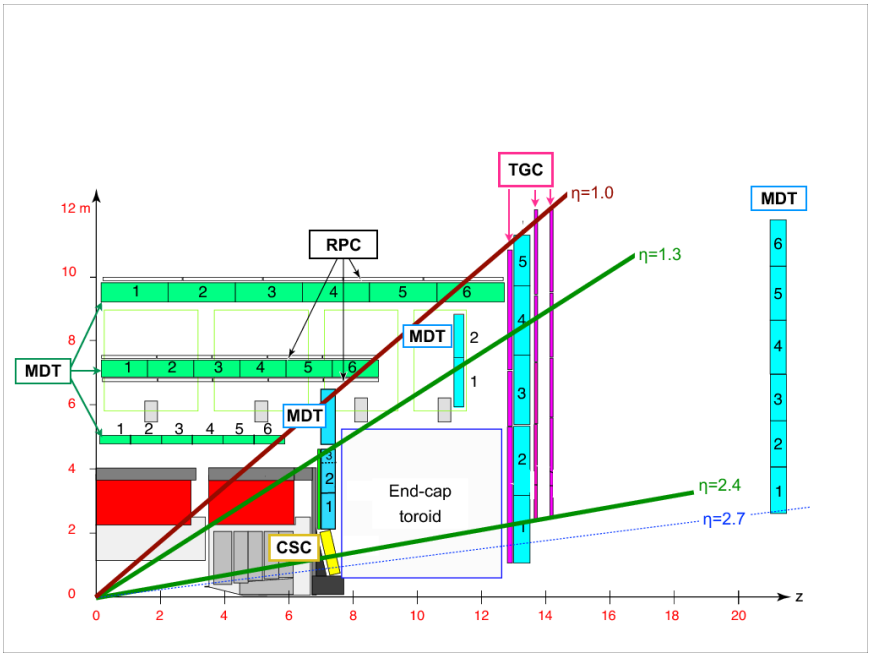

FIGURE 3.6: ATLAS muon system. ATLAS Experiment © 2016 CERN.

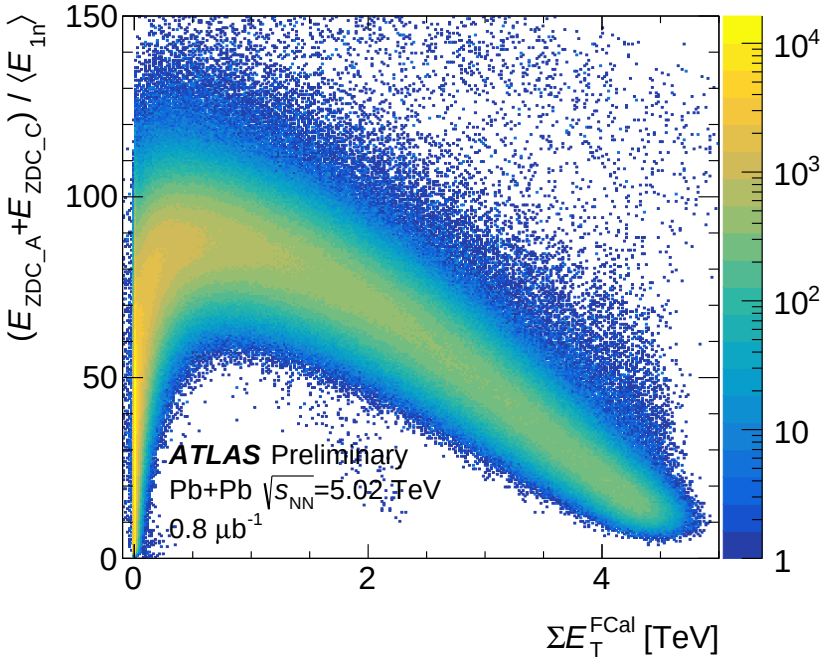

FIGURE 3.7: Correlation of the sum of the energies in the two ZDC arms, normalized to the single neutron energy, vs. the sum of transverse energies measured in the FCal cells ($3.2 < \eta < 4.9$) at the electromagnetic scale. Events are triggered on a combination of triggers, one based on a ZDC coincidence, confirmed by a track measured by the high level trigger, and the other based on measuring greater than 50 GeV in the full ATLAS calorimeter system. A reconstructed vertex is also required to be present in each event.

Chapter 4

Datasets and Event selection

In the analysis we used three different samples of data, MC HIJING overlay, HardProbes and MinBias data. In this section we briefly describe the composition and usage of these data samples.

4.1 Datasets

The HardProbes sample was used in two data formats: xAOD or full sample, and DAOD filtered with the HION3 derivation, requiring events with at least one J/ψ, $\psi(2S)$ or Υ reconstructed in events that have fire any of the muon triggers, details in appendix A. The xAOD data format was used only for performance studies while the DAOD data format was used in the extraction of the observables. MinBias data were used to calculate the number of event by centrality slice that will be used later to normalize the J/ψ yield in Pb-Pb collisions similar to what is done in pp with the integrated luminosity, details in appendix B. In Figure 4.1 we can see the raw cross section defined as J/ψ Candidates/Luminosity for each run, we can observed that in last part of the data taking the dimuon trigger was prescaled to suppress the high rate of dimuons produced in the Pb+Pb collisions.

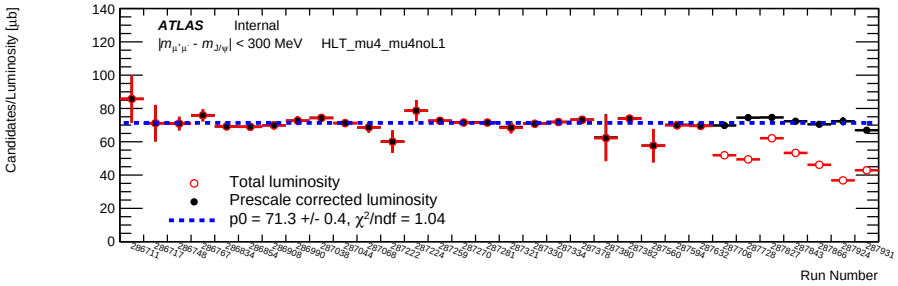

FIGURE 4.1: Raw cross section, defined as the number of J/ψ Candidates by Luminosity selected with the dimuon trigger HLT_mu4_mu4noL1 in 5.02 TeV Pb+Pb collision data for each run.

4.2 Simulation

Monte Carlo (MC) simulations have been used for performance studies. A sample of prompt ($pp \to J/\psi \to \mu\mu$) and non-prompt ($b\bar{b} \to J/\psi \to \mu\mu$) J/ψ simulated with PYTHIA8B+PHOTOS [64, 24], so called signal MC, overlaid

Name of the sample
mc15_5TeV.300200.Pythia8BPhotospp_A14_CTEQ6L1_bb_Jpsimu2p5mu2p5.merge.AOD.e4973_s2860_r7792_r7676
mc15_5TeV.300000.Pythia8BPhotospp_A14_CTEQ6L1_pp_Jpsimu2p5mu2p5.merge.AOD.e4973_s2860_r7792_r7676

TABLE 4.1: MC samples for simulation of J/ψ in pp events.

Name of the sample
mc15_5TeV.300000.Pythia8BPhotospp_A14_CTEQ6L1_pp_Jpsimu2p5mu2p5.merge.AOD.e4973_s2873_r8053_r7676/
mc15_5TeV.300000.Pythia8BPhotospp_A14_CTEQ6L1_pp_Jpsimu2p5mu2p5.merge.AOD.e4973_s2890_r8097_r7676/
mc15_5TeV.300000.Pythia8BPhotospp_A14_CTEQ6L1_pp_Jpsimu2p5mu2p5.merge.AOD.e4973_s2891_r8098_r7676/
mc15_5TeV.300000.Pythia8BPhotospp_A14_CTEQ6L1_pp_Jpsimu2p5mu2p5.merge.AOD.e4973_s2892_r8099_r7676/
mc15_5TeV.300000.Pythia8BPhotospp_A14_CTEQ6L1_pp_Jpsimu2p5mu2p5.merge.AOD.e4973_s2893_r8100_r7676/
mc15_5TeV.300200.Pythia8BPhotospp_A14_CTEQ6L1_bb_Jpsimu2p5mu2p5.merge.AOD.e4973_s2873_r8053_r7676/
mc15_5TeV.300200.Pythia8BPhotospp_A14_CTEQ6L1_bb_Jpsimu2p5mu2p5.merge.AOD.e4973_s2890_r8097_r7676/
mc15_5TeV.300200.Pythia8BPhotospp_A14_CTEQ6L1_bb_Jpsimu2p5mu2p5.merge.AOD.e4973_s2891_r8098_r7676/
mc15_5TeV.300200.Pythia8BPhotospp_A14_CTEQ6L1_bb_Jpsimu2p5mu2p5.merge.AOD.e4973_s2892_r8099_r7676/
mc15_5TeV.300200.Pythia8BPhotospp_A14_CTEQ6L1_bb_Jpsimu2p5mu2p5.merge.AOD.e4973_s2893_r8100_r7676/

TABLE 4.2: MC samples for simulation of J/ψ in Pb+Pb events.

with a sample of HIJING (Heavy Ion Jet INteraction Generator) simulation [44] was used to study the trigger and reconstruction performance in the high multiplicity environment of the Pb+Pb collision. MC dataset used are shown in tables 4.1,4.2.
To validate our simulation we compare the σ and the mass of the J/ψ signal observed in data and MC using a pair of fully reconstructed muons, muon + ID track and muon + MS segment. Comparison can be seen as a function of the "probe" η in figure 4.2 and a function of p_{T} in figure 4.3 and a function of $\sum E_T^{FCal}$ in figure 4.4.

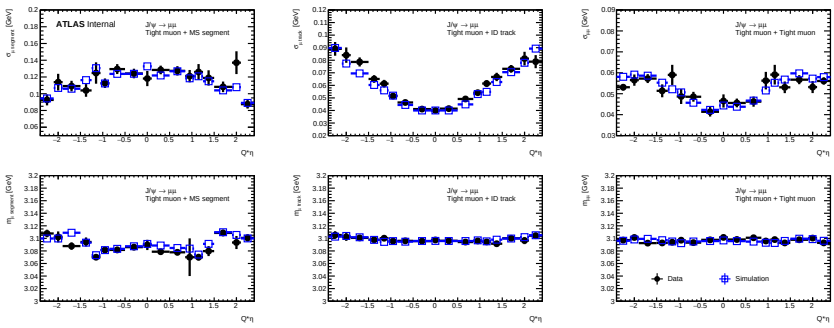

FIGURE 4.2: Comparison between the J/ψ σ and mass observed in data and MC as a function of the probe η.

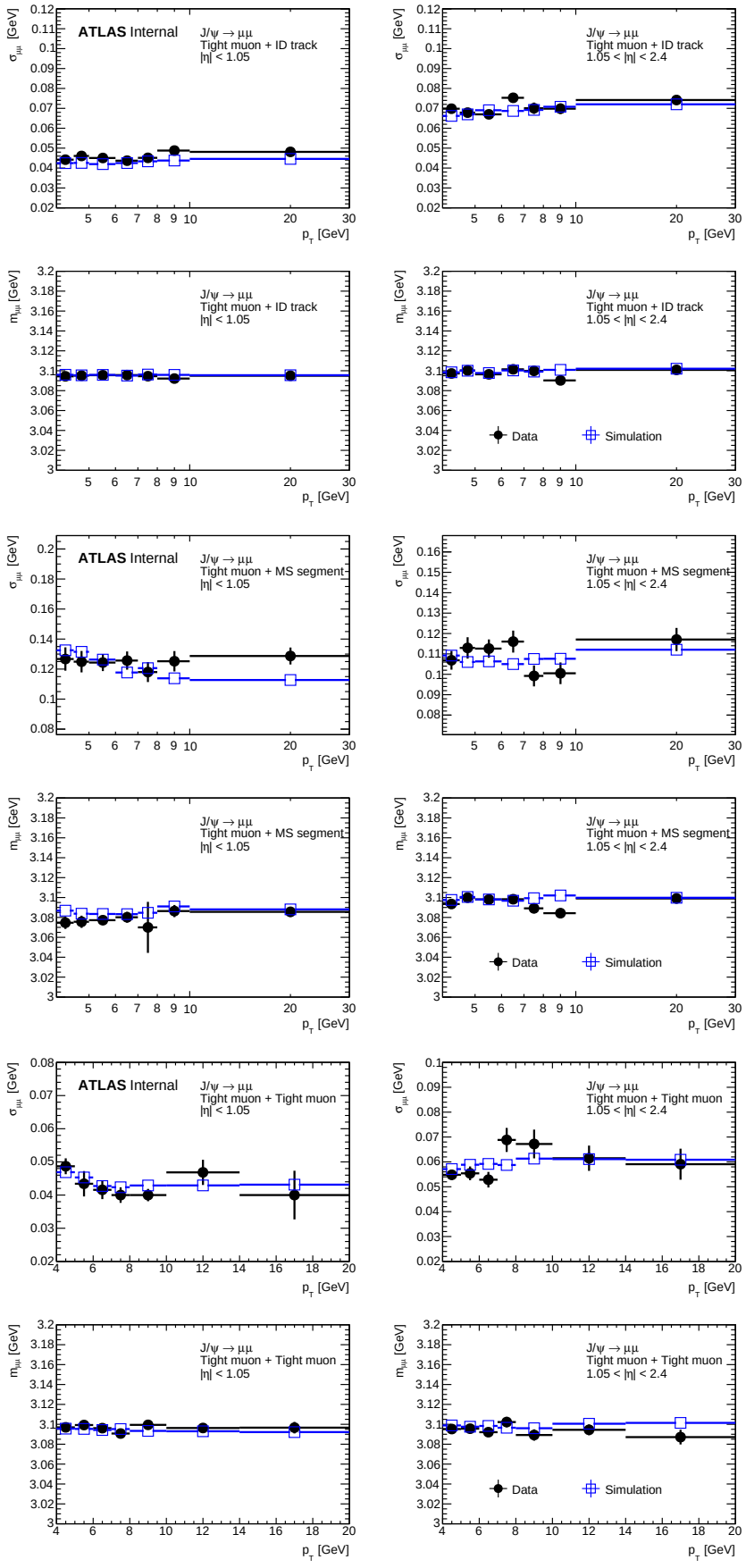

FIGURE 4.3: Comparison between the J/ψ σ and mass observed in data and MC as a function of the probe p_{T}.

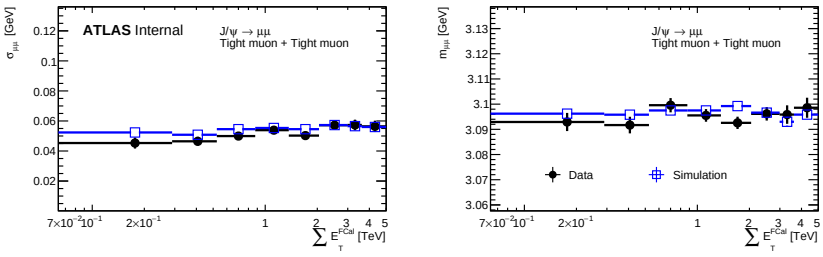

FIGURE 4.4: Comparison between the J/ψ σ and mass observed in data and MC as a function of the probe $\sum E_T^{FCal}$.

Chapter 5

Detector Performance

5.1 Muon Recostruction

The muon system is designed to reconstruct muons, providing an independent measurement of momentum from their curvature in the toroidal field. Muon reconstruction in the MS starts with a search for hit patterns inside each muon chamber to form segments. Muon track candidates are then built by fitting together hits from segments in different layers. The algorithm used for this task performs a segment-seeded combinatorial search that starts by using as seeds the segments generated in the middle layers of the detector where more trigger hits are available. The search is then extended to use the segments from the outer and inner layers as seeds. The segments are selected using criteria based on hit multiplicity and fit quality and are matched using their relative positions and angles. The same segment can initially be used to build several track candidates. Later, an overlap removal algorithm selects the best assignment to a single track, or allows for the segment to be shared between two tracks. The hits associated with each track candidate are fitted using a global χ^2 fit. A track candidate is accepted if the χ^2 of the fit satisfies the selection criteria. The MS tracks are then extrapolated to the interaction point and refitted with a loose interaction point constraint taking into account the energy loss in the calorimeter (see Figure 5.1). The tracks resulting from this process are known as muon extrapolated tracks (ME tracks).

5.1.1 Combined reconstruction

Several muon identification and reconstruction algorithms are employed in ATLAS, of which each exhibits specific benefits and limitations. Four muon types are defined depending on which subdetectors are used in reconstruction:

- Combined (CB) muon: track reconstruction is performed independently in the ID and MS, and a combined track is formed with a global refit that uses the hits from both the ID and MS subdetectors. During the global fit procedure, MS hits may be added to or removed from the track to improve the fit quality. Most muons are reconstructed following an outside-in pattern recognition, in which the muons are first reconstructed in the MS and then extrapolated inward and matched to an ID track.

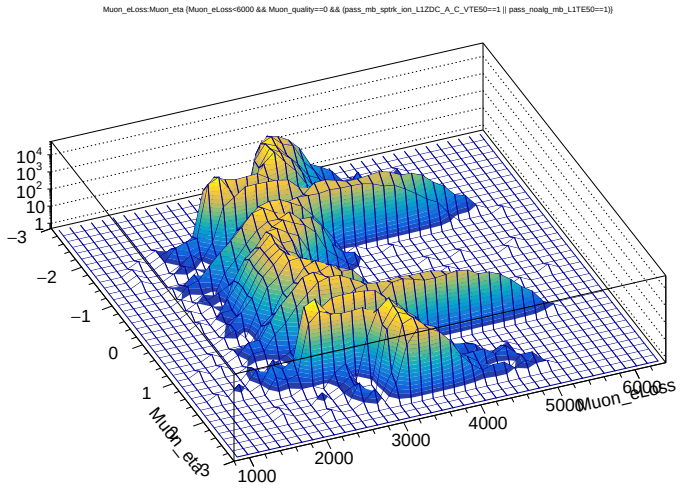

FIGURE 5.1: Muon energy loss in the calorimeters as a function of the muon η.

- MuGirl muon: Inside-out combined reconstruction, in which ID tracks are extrapolated outward and matched to MS tracks, this is used only as a complementary approach.
- Segment-tagged (ST) muons: a track in the ID is classified as a muon if, once extrapolated to the MS, it is associated with at least one local track segment in the MDT or CSC chambers. ST muons are used when muons cross only one layer of MS chambers, either because of their low pT or because they fall in regions with reduced MS acceptance.
- Calorimeter-tagged (CT) muons: a track in the ID is identified as a muon if it can be matched to an energy deposit in the calorimeter compatible with a minimum-ionizing particle. This type has the lowest purity of all the muon types but it recovers acceptance in the region where the ATLAS muon spectrometer is only partially instrumented to allow for cabling and services to the calorimeters and inner detector. The identification criteria for CT muons are optimised for that region ($|\eta| < 0.1$) and a momentum range of $15 < p_T < 100$ GeV.

5.1.2 Muon identification

Muon identification is performed by applying a set of quality requirements based upon the specific features of each of the muon types described in the previous section. Such requirements aim to reject fake muons coming mainly from pion and kaon decays and guarantee robust momentum measurements. For CB tracks, the variables used in muon identification are:

- q/p significance, defined as the absolute value of the difference between the ratio of the charge and momentum of the muons measured in the ID and MS divided by the sum in quadrature of the corresponding uncertainties;

$$\frac{|q/p_{ID} - q/p_{ME}|}{\sqrt{\sigma^2_{ID} + \sigma^2_{ME}}} \tag{5.1}$$

- $\rho^{'}$, defined as the absolute value of the difference between the transverse momentum measurements in the ID and MS divided by the p_T of the combined track;
$$\frac{p_T^{ID} - p_T^{ME}}{p_T^{CB}} \tag{5.2}$$
- normalised χ^2 of the combined track fit.

To guarantee a robust momentum measurement, specific requirements on the number of hits in the ID and MS are used. For the ID, the following quality cuts requires in the $|\eta| < 2.5$ region are applied:

- pixel hits + inoperative pixel sensors > 0;
- SCT hits + inoperative SCT sensors > 4;
- pixel holes + inoperative SCT sensors < 3;
- for $0.1 < |\eta| < 1.9$, $\mathrm{n}_{\mathrm{TRT}}^{\mathrm{hits}} + \mathrm{n}_{\mathrm{TRT}}^{\mathrm{outliers}} > 5$ and $\mathrm{n}_{\mathrm{TRT}}^{\mathrm{outliers}} < 0.9(\mathrm{n}_{\mathrm{TRT}}^{\mathrm{hits}} + \mathrm{n}_{\mathrm{TRT}}^{\mathrm{outliers}})$;

Four muon identification selections (Medium, Loose, Tight, and High-pT) are provided to address the specific needs of different physics analyses. Loose, Medium, and Tight are inclusive categories in that muons identified with tighter requirements are also included in the looser categories.
Medium muons The Medium identification criteria provide the default selection for muons in ATLAS. This selection minimises the systematic uncertainties associated with muon reconstruction and calibration. Only CB and ME tracks are used. The former are required to have ≥ 3 hits in at least two MDT layers, except for tracks in the $|\eta| < 0.1$ region, where tracks with at least one MDT layer but no more than one MDT hole layer are allowed. The latter are required to have at least three MDT/CSC layers, and are employed only in the $2.5 < |\eta| < 2.7$ region to extend the acceptance outside the ID geometrical coverage. A loose selection on the compatibility between ID and MS momentum measurements is applied to suppress the contamination due to hadrons misidentified as muons. Specifically, the q/p significance is required to be less than seven. In the pseudorapidity region $|\eta| < 2.5$, about 0.5% of the muons classified as Medium originate from the inside-out combined reconstruction strategy.
Loose muons The Loose identification criteria are designed to maximise the reconstruction efficiency while providing good-quality muon tracks. They are specifically optimised for reconstructing Higgs boson candidates in the four-lepton final state. All muon types are used. All CB and ME muons satisfying the Medium requirements are included in the Loose selection. CT and ST muons are restricted to the $|\eta| < 0.1$ region. In the region $|\eta| < 2.5$, about 97.5% of the Loose muons are combined muons, approximately 1.5% are CT and the remaining 1% are reconstructed as ST muons.
Tight muons Tight muons are selected to maximise the purity of muons at the cost of some efficiency. Only CB muons with hits in at least two stations of the MS and satisfying the Medium selection criteria are considered. The normalised χ^2 of the combined track fit is required to be < 8 to remove pathological tracks. A two-dimensional cut in the $\rho^{'}$ and q/p significance variables is performed as a function of the muon p_T to ensure stronger background rejection for momenta below 20 GeV where the misidentification

probability is higher.
High-p_T muons The High-pT selection aims to maximise the momentum resolution for tracks with transverse momentum above 100 GeV. The selection is optimised for searches for high-mass $Z^{'}$ and $W^{'}$ resonances. CB muons passing the Medium selection and having at least three hits in three MS stations are selected. Specific regions of the MS where the alignment is suboptimal are vetoed as a precaution. Requiring three MS stations, while reducing the reconstruction efficiency by about 20%, improves the pT resolution of muons above 1.5 TeV by approximately 30%.

5.1.3 Tight muon reconstruction efficiency

As the muon reconstruction in the ID and MS detectors is performed independently, a precise determination of the muon reconstruction efficiency in the region $|\eta| < 2.5$ is obtained with the tag-and-probe method as explained in the following. The method is based on the selection of an almost pure muon sample from $J/\psi \rightarrow \mu\mu$ events, requiring one leg of the decay (tag) to be identified as a tight muon [20] that fires the single muon trigger (HLT_mu4) and the second leg (probe) to be reconstructed by a system independent of the one being studied. Two kind of probes are used to measure muon efficiencies. ID tracks allow a measurement of the efficiency in the MS, while MS tracks are used to determine the complementary efficiency of the muon reconstruction in the ID.
The efficiency measurement for tight muons consists of two stages. First, the efficiency ε(Tight|ID) of reconstructing these muons is estimated assuming a reconstructed ID track. Then, this result is corrected by the efficiency ε(ID|MS) of the ID track reconstruction, measured using MS probes, finally the total efficiency is written in the form:

$$\varepsilon(\text{Tight}) = \varepsilon(\text{Tight}|\text{ID}) \times \varepsilon(\text{ID}) \approx \varepsilon(\text{Tight}|\text{ID}) \times \varepsilon(\text{ID}|\text{MS}) \qquad (5.3)$$

This approach is valid only if the ID track reconstruction is independent from the muon spectrometer track reconstruction (ε(ID) $\approx \varepsilon$(ID|MS)).
Tag-probe pairs are selected within the invariant mass window of 2.7-3.5 GeV and requiring a transverse momentum of at least 4 GeV for each muon. The tag muon is required to satisfy the Tight muon identification selection and to have triggered the readout of the event. A probe is considered successfully reconstructed if a selected muon, or MS track, is found within a ΔR = 0.05 cone around the probe track. The background contamination and the muon reconstruction efficiency are measured with a simultaneous maximum-likelihood fit of two statistically independent distributions of the invariant mass: events in which the probe is or is not successfully matched to the selected muon. The signal is modelled with a weighted sum of Gaussian and Crystal Ball functions with a single set of parameters for the two independent samples. Separate first-order polynomial fits are used to describe the background shape for matched and unmatched probes. Example plots are shown in figure 5.2

Results of the ε(Tight|ID) and ε(ID|MS) efficiencies can be seen in Figure 5.3, 5.4, 5.5 and 5.6. In order to suppress statistical fluctuation of efficiency, the truth reconstruction efficiency, shown in Figure 5.7, is used to

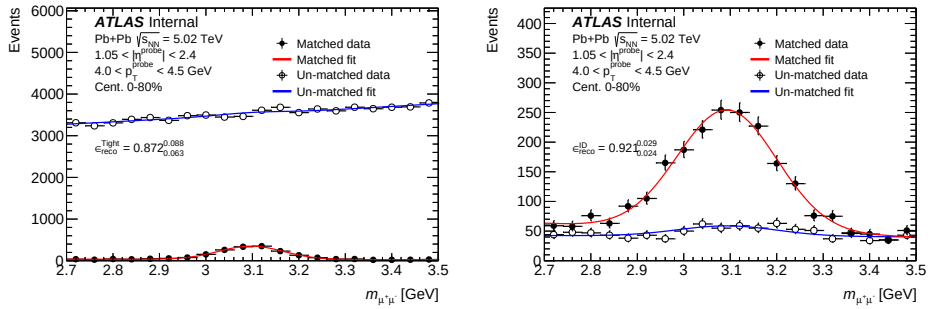

FIGURE 5.2: Fit examples of: (left) extraction of the first term of the reconstruction efficiency $\varepsilon(\text{Tight}|\text{ID})$, (right) extraction of the second term of the reconstruction efficiency $\varepsilon(\text{ID}|\text{MS})$.

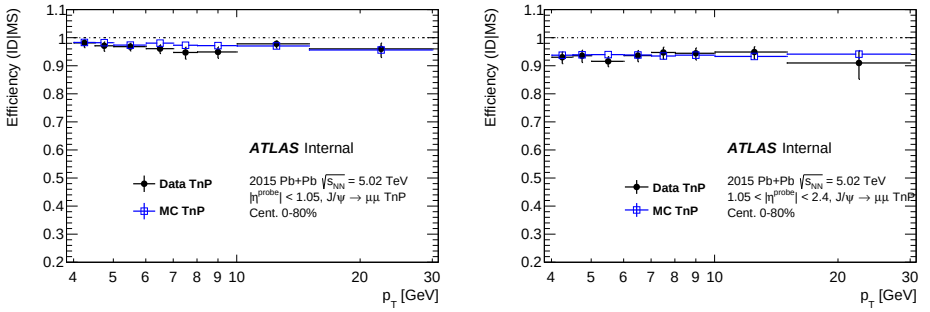

FIGURE 5.3: ID reconstruction efficiency of muons as a function of the muon p_T for the barrel region (left) and the end-cap region (right). Black solid points represents efficiencies obtained from 5.02 TeV Pb+Pb data, while blue open squares represents efficiency in MC.

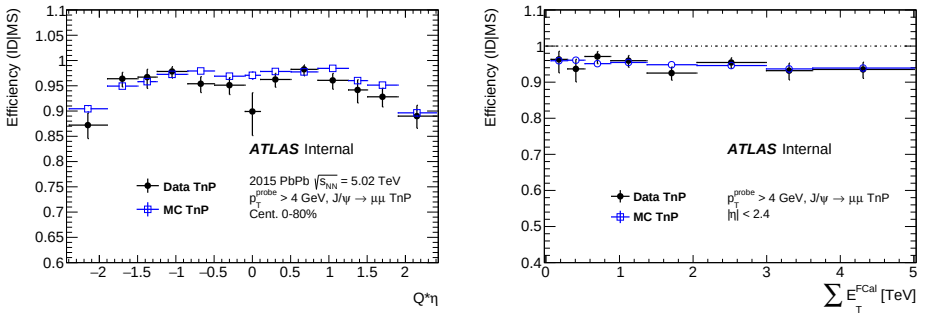

FIGURE 5.4: ID reconstruction efficiency of muons as a function of the muon η (left) and the sum E_T in the forward calorimeter (right). Black solid points represents efficiencies obtained from 5.02 TeV Pb+Pb data, while blue open squares represents efficiency in MC.

correct data. In addition to the efficiency itself, a scale factor define as the fit of the ratio between efficiency obtained using tag-and-probe method in data and simulation is applied to recover any deviation of the simulation

from real detector behavior. The data to simulation ratio is defined as:

$$\mathrm{SF}(p_T^{\mu}, \eta_{\mu}) = \frac{\varepsilon_{\mathrm{data}}(\mathrm{Tight}|\mathrm{ID}) \times \varepsilon_{\mathrm{data}}(\mathrm{ID}|\mathrm{MS})}{\varepsilon_{\mathrm{MC}}(\mathrm{Tight}|\mathrm{ID}) \times \varepsilon_{\mathrm{MC}}(\mathrm{ID}|\mathrm{MS})} \tag{5.4}$$

The resulting reconstruction scale factors are shown in Figure 5.8, discussion about systematic uncertainties is done in Section 6.4. The total reconstruction weight for a selected candidate (μ_1, μ_2) in Pb+Pb data is given by:

$$\omega_{\mathrm{reco}} = 1/(\mathrm{SF}(\mu_1) * \varepsilon_{\mathrm{MC}}^{\mathrm{truth}}(\mu_1) \times \mathrm{SF}(\mu_2) * \varepsilon_{\mathrm{MC}}^{\mathrm{truth}}(\mu_2)) \tag{5.5}$$

Finally, to correct the data accounting for the centrality dependence of the reconstruction efficiency, we compare the average efficiency, $\langle\epsilon\rangle$, with the centrality dependent efficiency, $\epsilon(E_{\mathrm{T}})$. Then a fit of the ratio of this two quantities, $\langle\epsilon\rangle/\epsilon(\mathrm{E_T})$, is used to correct the data, together with its systematic variations, on top of the usual reconstruction correction. Plots of the $\epsilon(E_{\mathrm{T}})$ and $\langle\epsilon\rangle$ comparison and their ratio are presented in figure 5.9. Adding this new term to equation 5.5 we obtain the complete reconstruction weight:

$$\omega_{\mathrm{Full\ reco}} = \left(\frac{\langle\epsilon\rangle}{\epsilon(E_{\mathrm{T}})}\right)^2 \frac{1}{\mathrm{SF}(\mu_1) * \varepsilon_{\mathrm{MC}}^{\mathrm{truth}}(\mu_1) \times \mathrm{SF}(\mu_2) * \varepsilon_{\mathrm{MC}}^{\mathrm{truth}}(\mu_2)}. \tag{5.6}$$

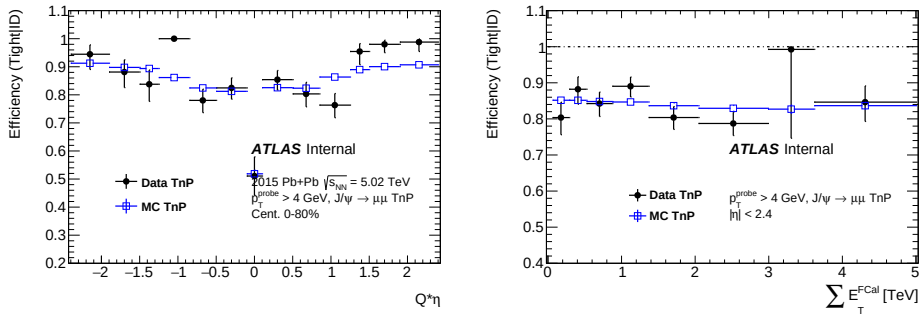

FIGURE 5.5: Muons reconstruction efficiency as a function of the probe η (left) and the sum E_T in the forward calorimeter (right). Black solid points represents efficiencies obtained from 5.02 TeV Pb+Pb data, while blue open squares represents efficiency in MC.

5.1.4 Pb+Pb versus pp reconstruction

The muon reconstruction performance in pp collisions is necessary to measure the J/ψ cross section, σ_{pp}. The pp performance can be found in several papers as [19, 20]. In these thesis we restrict ourselves to just show the clear difference observed with respect to Pb+Pb collisions, specially in the performance of the inner detector.

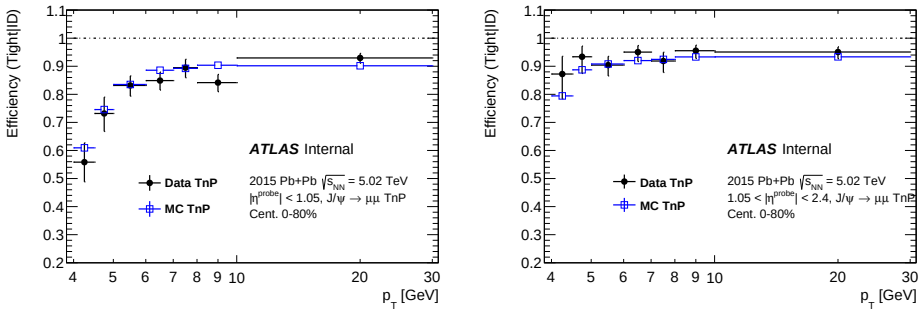

FIGURE 5.6: Muons reconstruction efficiency with respect to ID as a function of the muon p_T for the barrel region (left) and the end-cap region (right). Black solid points represents efficiencies obtained from 5.02 TeV Pb+Pb data, while blue open squares represents efficiency in MC.

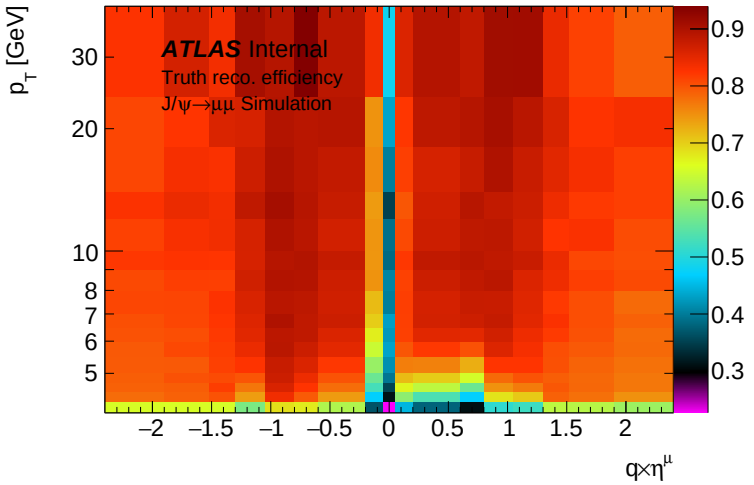

FIGURE 5.7: Truth reconstruction efficiency map for "Tight" muons obtained from MC.

5.2 Muon triggering Run2

5.2.1 Level-1 (L1) muon trigger

Muon triggers are denoted by the prefix (MU), there are three low-p_{T} thresholds (MU0, MU4, MU6) and three high-p_{T} thresholds (MU10, MU15, MU20). The L1 triggers generated by hits in the RPC require a coincidence of hits in the three layers for the highest three p_{T} thresholds, and a coincidence of hits in two of the three layers for the rest of thresholds. The L1 triggers generated by hits in the TGC require a coincidence of hits in the three layers, except for limited areas in the lowest threshold.
Following the p_{T} thresholds and the corresponding detector regions, region of interest (RoIs), are then sent to the high-level-trigger (HLT) for further consideration. The typical dimensions of the RoIs are 0.1×0.1 (0.03×0.03) in $\Delta\eta \times \Delta\phi$ in the RPCs (TGCs). The geometric coverage of the L1 trigger is about 99% in the endcap regions and about 80% in the barrel region. The

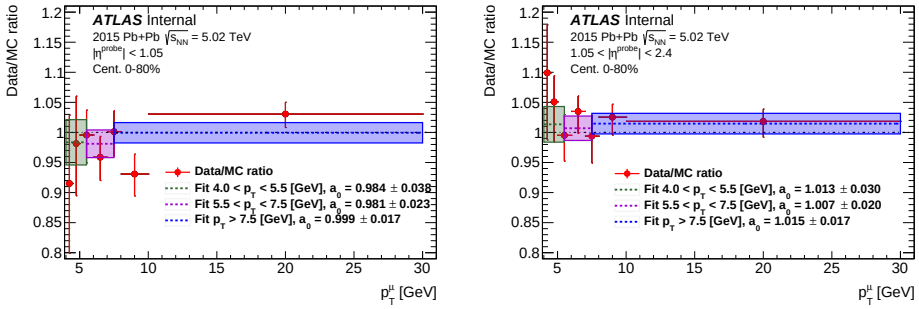

FIGURE 5.8: Tight muon reconstruction efficiency scale factor as a function of the muon p_T for the barrel region (left) and the end-cap region (right). Flat fits are applied to three different p_T ranges, 4.0-5.5, 5.5-7.5 and 7.5-30 GeV.

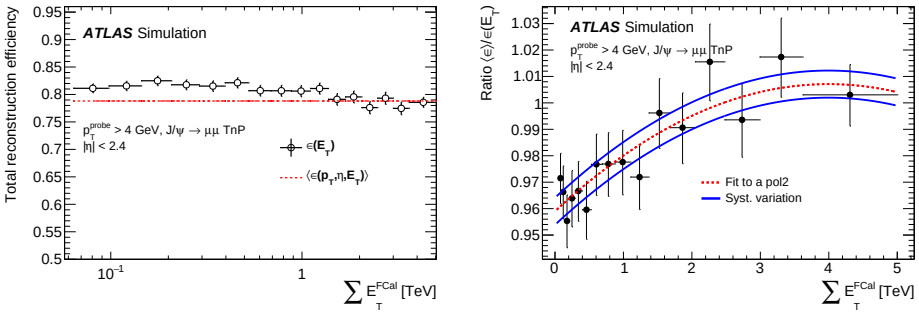

FIGURE 5.9: (left) Comparison between the average reconstruction efficiency and the reconstruction efficiency as a function of the sum of traverse energy deposited in the forward calorimeters. (right) Ratio between the centrality dependent efficiency and the average efficiency.

limited geometric coverage in the barrel region is due to gaps at around $\eta = 0$ (to provide space for services of the inner detector and calorimeters), the feet and rib support structures of the ATLAS detector and two small elevator shafts in the bottom part of the spectrometer plus a few dead RPC chambers (see Fig. 5.13).

5.2.2 High-Level-Trigger (HLT)

Muons in the event-filter are found by two different procedures. The first focuses on RoIs defined by the Level-1 described above and is referred to as the RoI-based method. The second procedure searches the full detector without using the information from the previous levels and is referred to as the full-scan (FS) method and is specify with the suffix **noL1** in the name. In the RoI-based method, muon candidates are first formed by using the muon detectors (called event-filter stand-alone-muons), and are subsequently combined with inner detector tracks leading to event-filter combined-muons. If no combined-muon is formed, muon candidates are searched for by extrapolating inner detector tracks to the muon detectors. If there are corresponding track segments, combined-muons are formed.

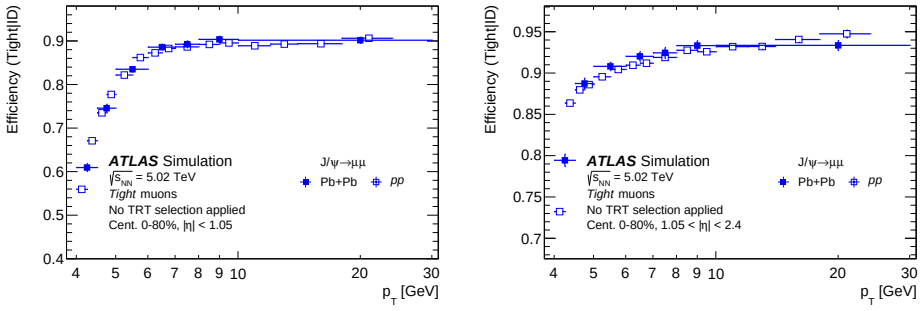

FIGURE 5.10: Muon reconstruction efficiency with respect to the ID in pp and Pb+Pb 5.02 TeV collisions as a function of the muon transverse momentum. (left) For the Barrel region, $|\eta| < 1.05$, (right) For the Endcap region, $1.05 < |\eta| < 2.4$

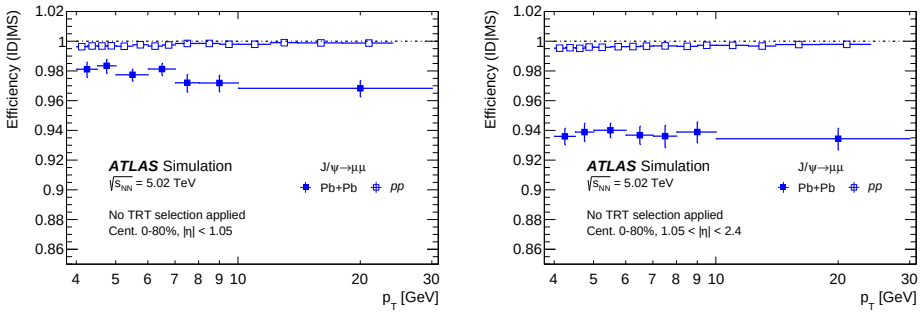

FIGURE 5.11: ID reconstruction efficiency of tracks related to muons in pp and Pb+Pb 5.02 TeV collisions as a function of the muon transverse momentum. (left) For the Barrel region, $|\eta| < 1.05$, (right) For the Endcap region, $1.05 < |\eta| < 2.4$

5.2.3 Menu proposal for Pb+Pb 5.02 TeV

Several single and di-muon chains were studied to determinate their feasibility to run during the Pb+Pb data taking, CPU and timing consumption in addition to the their rate rejection was evaluated to discriminate between the different algorithms. In this study we focus in a hybrid RoI-FullScan chain for di-muons event selection because this algoritm shows the best efficiency to background rejection proportion (agains the others algos) and also the correlation between the two muons is not strong making easier the performance determination in physics analysis.
Single muon chains was designed to collect events coming from electroweak processes, $Z \rightarrow \mu\mu$ and $W \rightarrow \nu\mu$, while di-muon chains were specially tuned to select event with quarkonia decays, $J/\psi, \psi(2S), \Upsilon(1S, 2S, 3S)$, to muons. Table 5.1 and Table 5.2 show some of the chains selected for studies and proposed to be included in the menu. The color in Table 5.1 and Table 5.2 refers to a different algorithm Full-scan, RoI base, MS only. The rates was predicted using a default luminosity of $L = 2 * 10^{27} cm^{-2} s^{-1}$.
In Table 5.3 we show the full list of algorithm that run during the FS chain,

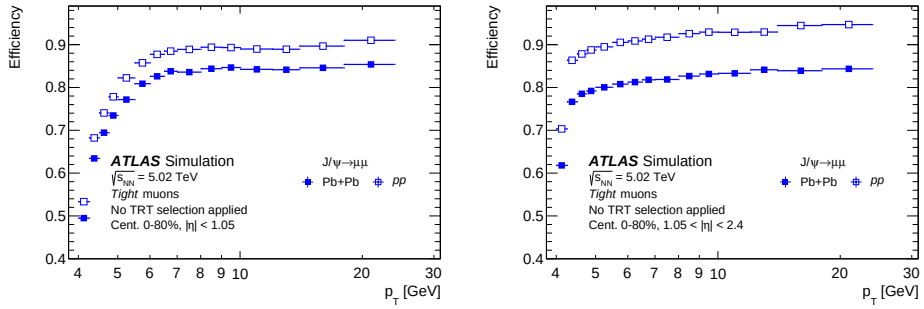

FIGURE 5.12: Total muon reconstruction efficiency in pp and Pb+Pb 5.02 TeV collisions as a function of the muon transverse momentum. (left) For the Barrel region, $|\eta| < 1.05$, (right) For the Endcap region, $1.05 < |\eta| < 2.4$

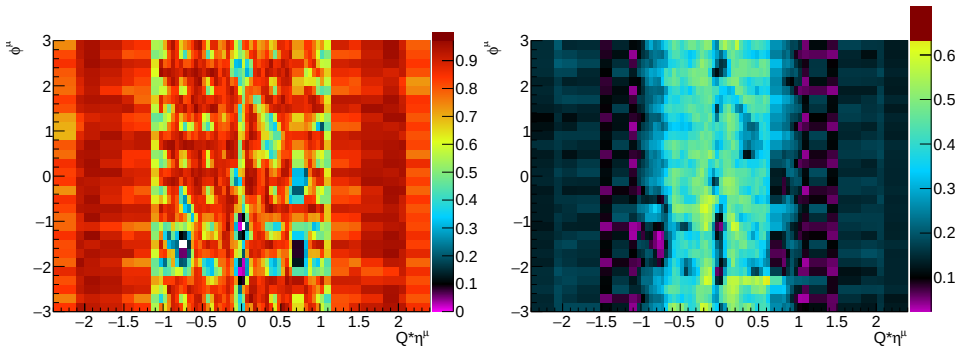

FIGURE 5.13: Trigger efficiency maps made with muons with $p_{\mathrm{T}} > 6$ GeV (left) and muons with $p_{\mathrm{T}} < 6$ GeV (right). (left) We can see the RPC dead chambers (holes) in ϕ[-1,-2] and the space for service around $\eta = 0$. (right) We can distinguish the 8 magnets pipes along ϕ.

we observed that the final step "Muon Spectrometer to Inner detector interpolation" have a huge CPU consumption because of the large number of reconstructed tracks in the inner detector, this can end-up with a rain of time-out during the eventual data taking overwhelming the acquisition system. As a result of this study we recommend not run the single muon FS chain during the peak of instantaneous luminosity or run it but heavily prescaled.

5.2.4 Trigger efficiency

Dimuon trigger in Pb+Pb collisions

The event selection trigger of Pb+Pb data is HLT_mu4_mu4noL1. This dimuon trigger is seeded by a single muon L1 item, L1_MU4, which requires the formation of a RoI with $p_{\mathrm{T}} > 4$ GeV at L1. The muon candidates found at L1 must be confirmed at HLT, and the ID-MS combined tracks of the trigger elements must also satisfy $p_{\mathrm{T}} > 4$ GeV. Once the muon is confirmed at HLT a search for a second muon start this time by the FullScan algorithm, this one doesn't require an RoI formed at L1. To estimate the efficiency of

HLT Chain	L1 item	prescale	Rate [Hz]	Info
mu4noL1	L1_MU4	1	264	support
mu4	L1_MU4	1	289	support
mu4_L1MU0	L1_MU0	1	302	support
mu6noL1	L1_MU4	1	87	support
mu6	L1_MU4	1	79	Primary
mu6_L1MU0	L1_MU0	1	80	backup
mu10	L1_MU6	1	11	backup
mu14	L1_MU10	1	3	backup
mu15_msonly	L1_MU11	1	18	testing
mu20_msonly	L1_MU15	1	11	testing

TABLE 5.1: Single muons chains.

HLT Chain	L1 item	prescale	Rate [Hz]	Info
2mu4	L1_2MU4	1	7	backup
2mu4_L1MU0	L1_2MU0	1	8	testing
2mu4_msonly	L1_2MU4	1	11	testing
2mu4_msonly_L1MU0	L1_2MU0	1	13	testing
2mu6	L1_2MU4	1	0.9	backup
2mu6_L1MU0	L1_2MU0	1	0.9	testing
2mu6_msonly	L1_2MU4	1	2	testing
2mu6_msonly_L1MU0	L1_2MU0	1	3	testing
mu4_mu4noL1	L1_MU4	1	13	Primary
mu6_mu4noL1	L1_MU4	1	4	backup

TABLE 5.2: Di-muon chains.

HLT_mu4_mu4noL1 chain, the following factorization form is used:

$$\varepsilon_{\text{trig}}(\mu_1,\mu_2) = \begin{array}{l} 1-(1-\varepsilon_{\text{mu4}}(\mu_1))(1-\varepsilon_{\text{mu4}}(\mu_2)) \\ -\varepsilon_{\text{mu4}}(\mu_1)\cdot(1-\varepsilon_{\text{mu4noL1}}(\mu_2)) \\ -\varepsilon_{\text{mu4}}(\mu_2)\cdot(1-\varepsilon_{\text{mu4noL1}}(\mu_1)) \end{array} \tag{5.7}$$

where ε(mu4) is the efficiency of RoI based HLT_mu4 single muon trigger with respect to reconstructed muons and ε(mu4noL1) is the efficiency of the FullScan based HLT_mu4noL1 single muon trigger.
This section describes the method to measure the efficiency and the selection used to define the sample used. In the following, unless otherwise specified, when referring to a "muon" it is implicit that this particle is reconstructed as a tight muon.
Tag-and-probe is use to measure the muon trigger performance. The tag-and-probe method relies on a pair of muon candidates. If one muon candidate has caused the trigger to record the event (called the tag-muon), the other muon serves as a "probe" (called the probe-muon) to measure the trigger performance with a minimal amount of bias. This method has been applied in the present analysis to dimuon decays of J/ψ mesons candidates. Events are required to pass the single-muon trigger HLT_mu6. A pair of oppositely charged muons with invariant mass consistent with the mass of the J/ψ, $|m_{J/\psi} - m_{\mu\mu}| < 0.4$ GeV, is required for measuring the efficiency

n	CPU(ms)	Component
80	328	TrigMuSuperEF_FSSA
37	1	TrigMuonEFFSRoiMaker
255	295	TrigFastTrackFinder_Muon
245	114	TrigAmbiguitySolver_Muon_EFID
245	12	TRTDriftCircleMaker_Muon_EFID
245	14	TRTTrackExtAlg_Muon_EFID
245	80	TrigExtProcessor_Muon_EFID
245	31	InDetTrigTrackSlimmer_Muon_EFID
245	3	InDetTrigTrackingxAODCnv_Muon_EFID
245	2	TrigVxPrimary_Muon_EFID
245	1	InDetTrigParticleCreation_Muon_EFID
245	1	InDetTrigVertexxAODCnv_Muon_EFID
37	11081	TrigMuSuperEF_TMEFCombinerOnly
Total	11963 milliseconds	

TABLE 5.3: HLT_mu4noL1 list of algorithm and timers.

of the dimuon trigger. The tag muon is required to have $p_T > 6$ GeV and to have an angular distance of $\Delta R < 0.05$ to an HLT object that passes the HLT_mu6 trigger.
The probe-muon is matched to a trigger object if it lies within a distance $\Delta R < 0.01$ from an HLT object. In the case of the HLT_mu4noL1 trigger all probes are also required to match the L1_MU4 with a $\Delta R < 0.3$ in order to remove totally the L1 dependence. The background contamination and the muon reconstruction efficiency are measured with a simultaneous maximum-likelihood fit of two statistically independent distributions of the invariant mass: events in which the probe is or is not successfully matched to the selected muon, in the same way that is done for the reconstruction efficiency. Example of the fits used to extract the efficiency is shown in figure 5.14.

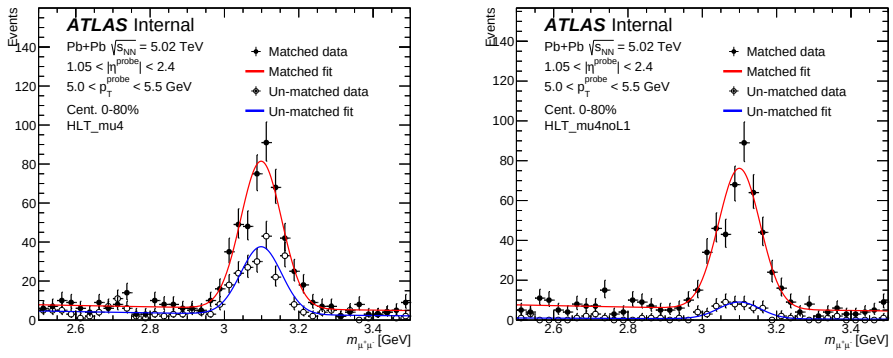

FIGURE 5.14: Selected fit: (leff) example of the extraction of the trigger efficiency $\varepsilon_{\mathrm{mu4}}$, (right) example of the extraction of the trigger efficiency $\varepsilon_{\mathrm{mu4noL1}}$.

The trigger efficiency obtainer from MC is used to correct the mu4 tail of the dimuon trigger together with the data to MC scale factor to cover

possible difference between simulation and data. The mu4noL1 tail of the dimuon trigger is corrected with efficiency obtained from minimun-bias data using the inclusive method, as well, together with the hardprobe to minbias scale factor to cover possible difference between this two data samples. The key idea of the inclusive method is use muons from events recorded by triggers other than the muon triggers. The minimum bias triggers offer a set of events that are almost completely uncorrelated with the muon trigger. Each event is required to satisfy HLT_mb_sptrk_ion_L1ZDC_A_C_VTE50 || HLT_noalg_mb_L1TE50, then each muon that fire the L1_MU4 is matched to a trigger object if it lies within a distance $\Delta R < 0.01$ from an HLT object. The trigger efficiency is defined as the fraction of muons that are associated with a trigger object divided by the total number of muons. The reconstruction scale factor is defined as:

$$\mathrm{SF}(p_T^{\mu}, \eta_{\mu}) = \frac{\varepsilon_{\mathrm{data}}(\mathrm{x}; p_T^{\mu}, \eta_{\mu})}{\varepsilon_{\mathrm{MC}}(\mathrm{x}; p_T^{\mu}, \eta_{\mu})}; \text{ where x = mu4} \tag{5.8}$$

$$\mathrm{SF}(p_T^{\mu}, \eta_{\mu}) = \frac{\varepsilon_{\mathrm{data}}(\mathrm{x}; p_T^{\mu}, \eta_{\mu})}{\varepsilon_{\mathrm{MB}}(\mathrm{x}; p_T^{\mu}, \eta_{\mu})}; \text{ where x = mu4noL1} \tag{5.9}$$

respectively for each trigger. The resulting one dimentional HLT_mu4 and HLT_mu4noL1 trigger efficiencies obtained from Pb+Pb data and MC/MB are shown in Figures 5.15,5.16 and 5.17 together with their respective scale factor. As we can see the single-chains shown a small dependence as a function of the centrality. The source of the inefficiency was studied and results can be seen in appendix D.

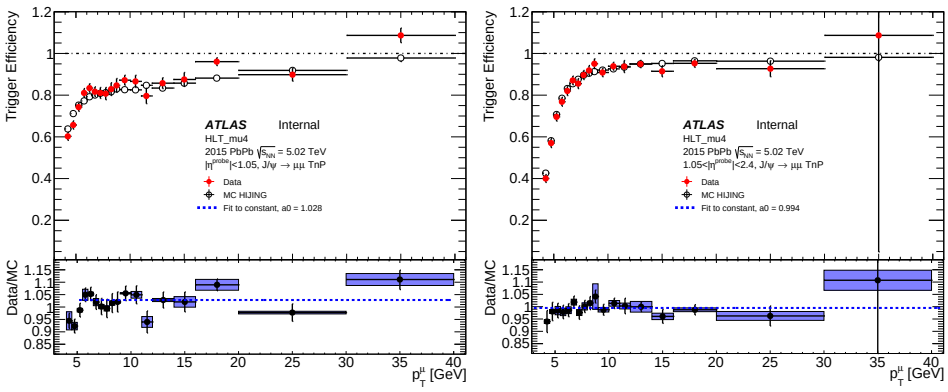

FIGURE 5.15: HLT_mu4 trigger efficiency and scale factor obtained from Pb+Pb data using $J/\psi \rightarrow \mu^+\mu^-$ tag and probe method in comparison with $J/\psi \rightarrow \mu^+\mu^-$ MC, shown as a function of the muon p_T for the barrel region (left) and the end-cap region (right).

The two dimensional efficiency map obtained from $\psi \rightarrow \mu^+\mu^-$ MC and used to correct data is shown in Figure 5.18.

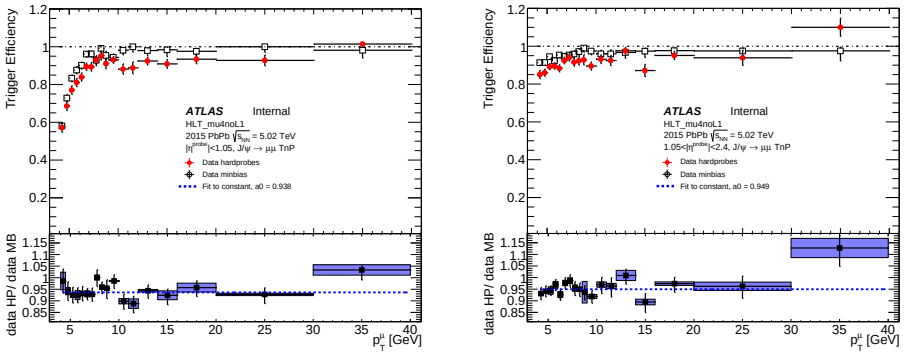

FIGURE 5.16: HLT_mu4noL1 trigger efficiency and scale factor obtained from Pb+Pb data using $J/\psi \rightarrow \mu^+\mu^-$ tag and probe method in comparison with minimum-bias efficiency, shown as a function of the muon p_T for the barrel region (left) and the end-cap region (right).

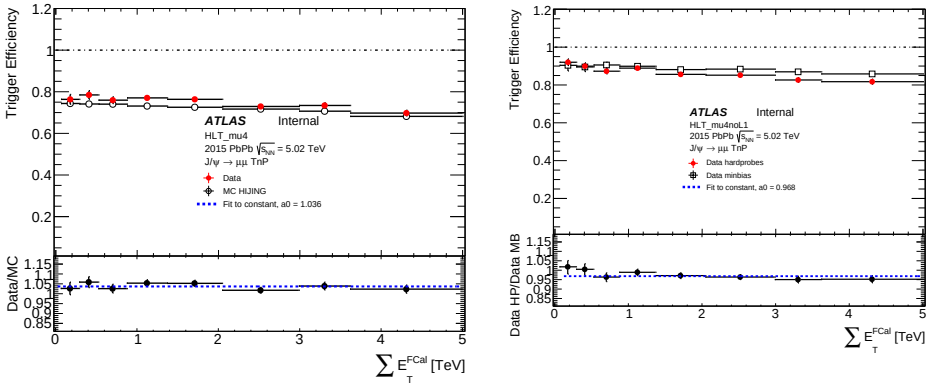

FIGURE 5.17: HLT_mu4 (left) and HLT_mu4noL1 (right), trigger efficiency and scale factor obtained from Pb+Pb data using $J/\psi \rightarrow \mu^+\mu^-$ tag and probe method in comparison with $J/\psi \rightarrow \mu^+\mu^-$ MC for HLT_mu4 and inclusive method in minbias data for HLT_mu4noL1, shown as a function of the sum of E_T in the forward calorimeter.

Dimuon trigger in pp collisions

The event selection trigger at for pp data is HLT_2mu4_bJpsimumu. This di-muon trigger is seeded by a dimuon L1 item, L1_2MU4, which requires the formation of two different RoIs with $p_{\mathrm{T}} > 4$ GeV at L1. To further reduce the L1 trigger rates such that to collect data with this dimuon chain unprescaled, the hardware based L1 topological cuts [22] on invariant mass and ΔR between the two RoIs are also applied. The two muon candidates found at L1 must be confirmed at HLT, and the ID-MS combined tracks of the trigger elements must also satisfy $p_{\mathrm{T}} > 4$ GeV.

To estimate the efficiency of HLT_2mu4_bJpsimumu chain, the following factorization form is used:

$$\varepsilon_{\mathrm{trig}}(\mu_1\mu_2) = \varepsilon(mu4;\ \mu_1) \cdot \varepsilon(mu4;\ \mu_2) \cdot C_{\mu\mu}(\Delta R_{\mu\mu}, y_{\mu\mu}, \tau_{\mu\mu}) \qquad (5.10)$$

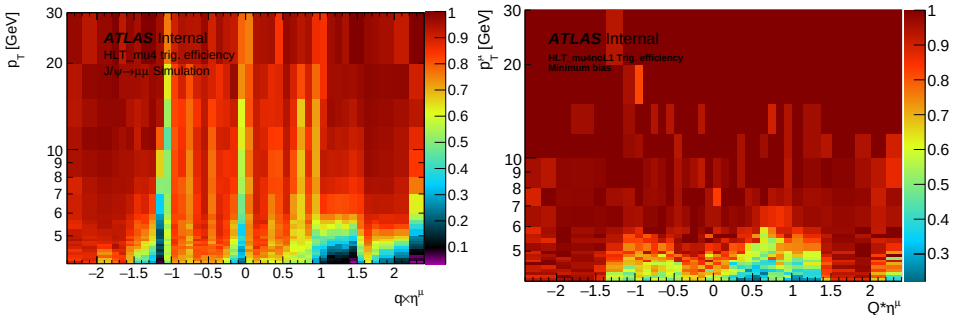

FIGURE 5.18: Trigger efficiency maps using correct the J/ψ yields. (left) HLT_mu4 efficiency obtained from MC, (Right) HLT_mu4noL1 efficiency obtained from minimum bias data.

where $\varepsilon(mu4)$ is the efficiency of RoI based HLT_mu4 single muon trigger efficiency with respect to reconstructed muons, $C_{\mu\mu}(\Delta R_{\mu\mu}, y_{\mu\mu}, \tau_{\mu\mu})$ is the correction factor aiming to recover the events loss due to features that the single muon trigger chains don't have, which are the requirement of one additional RoI and L1 topological cuts applied to the RoI pairs. The two single muon efficiency terms become strongly correlated in the case of both muons contained in the same RoI, since the efficiency of the dimuon chain should be 0 if only single RoI has been formed. In order to suppress such strong correlation, tight L1 muon and RoI matching requirement is applied to the HLT_mu4 efficiency determination. The resulting 1D HLT_mu4 trigger efficiency obtained from pp data and MC is shown in Fig 5.19.

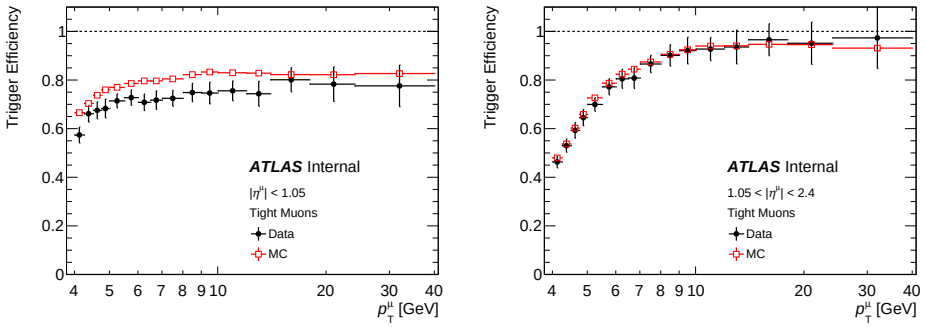

FIGURE 5.19: HLT_mu4 trigger efficiency as a function of the muon p_{T} for the barrel region (left) and the end-cap region (right).

The trigger efficiency obtained from MC is used to correct data together with the data to MC scale factor defined as:

$$\mathrm{SF}(p_{\mathrm{T}}^{\mu}, \eta_{\mu}) = \frac{\varepsilon_{\mathrm{data}}(mu4;\ p_{\mathrm{T}}^{\mu}, \eta_{\mu})}{\varepsilon_{\mathrm{MC}}(mu4;\ p_{\mathrm{T}}^{\mu}, \eta_{\mu})}; \tag{5.11}$$

The 1D HLT_mu4 trigger efficiency scale factors are shown in Fig. 5.20. The 2D MC map used to correct data is shown in Fig. 5.21.

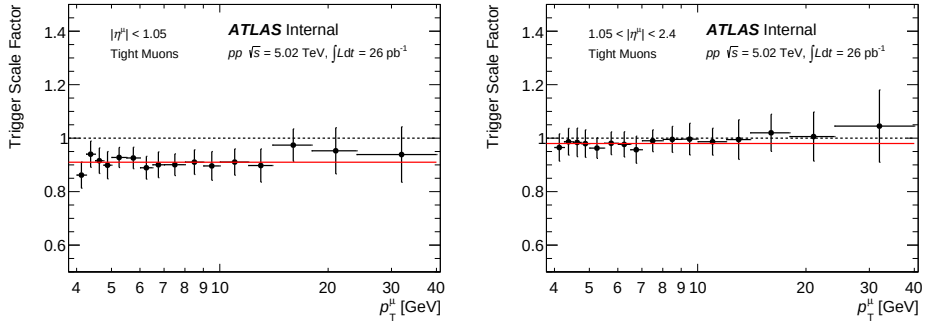

FIGURE 5.20: HLT_mu4 trigger efficiency scale factor as a function of the muon p_{T} for the barrel region (left) and the end-cap region (right). Flat fits are applied to the full p_{T} range. The fitted scale factor value is 9.2 for the barrel region and 9.8 for the end-cap region.

This correction factor is measured by using $J/\psi \rightarrow \mu^+\mu^-$ MC, and a control sample is selected with trigger HLT_mu4 and the muon with positive charge in the event must be matched with HLT_mu4 trigger elements. The value of the correction is determined from the ratio of the J/ψ signal in the control sample passing the dimuon trigger HLT_2mu4_bJpsimumu and weighted with $1/\varepsilon(mu4;\mu^-)$, to the total signals in the control sample:

$$C_{\mu\mu}(\Delta R_{\mu\mu}, y_{\mu\mu}, \tau_{\mu\mu}) = \frac{N_{J/\psi}(\text{HLT\_mu4 and HLT\_2mu4\_bJpsimumu})}{N_{J/\psi}(\text{HLT\_mu4}) \cdot \varepsilon(mu4;\mu^-)} \tag{5.12}$$

If the two single muon trigger efficiency terms are uncorrelated, the correction factor equals 1. The correction factor is less than 1 in case that the dimuon trigger is less efficient than the combination of two single muons terms. The correction factor has been factorized as:

$$C_{\mu\mu}(\Delta R_{\mu\mu}, y_{\mu\mu}, \tau_{\mu\mu}) = C_{\mu\mu}(\Delta R_{\mu\mu}, y_{\mu\mu}) \cdot C_{\mu\mu}(\tau_{\mu\mu}) \tag{5.13}$$

where $C_{\mu\mu}(\Delta R_{\mu\mu}, y_{\mu\mu})$ is for correcting double RoI requirement and L1 topological cuts while $C_{\mu\mu}(\tau_{\mu\mu})$ is added to fix bias as a function of dimuon lifetime due to a bug in the trigger algorithm. $C_{\mu\mu}(\Delta R_{\mu\mu}, y_{\mu\mu})$ and $C_{\mu\mu}(\tau_{\mu\mu})$ are found to be uncorrelated. To avoid double counting of any sources of the dimuon chain inefficiency, the two terms are further required to be: $C_{\mu\mu}(\Delta R_{\mu\mu}, y_{\mu\mu}) = C_{\mu\mu}(\Delta R_{\mu\mu}, y_{\mu\mu};\ |\tau| < 3$ ps), and a scale factor has been applied to $C_{\mu\mu}(\tau_{\mu\mu})$ such that $C_{\mu\mu}^{\max}(\tau_{\mu\mu}) = 1$. Fig. 5.22 shows the correction factor used to correct the pp data.

5.2.5 Closure test of dimuon trigger factorization

Due to the factor that dimuon trigger efficiency cannot be measured directly, it has been always factorized into terms consisting single muon trigger efficiency and, sometimes, the correlation correction terms. The factorization holds under assumptions, so it becomes crucial to validate the factorization. In the simulation, the so-called closure test can be used as the

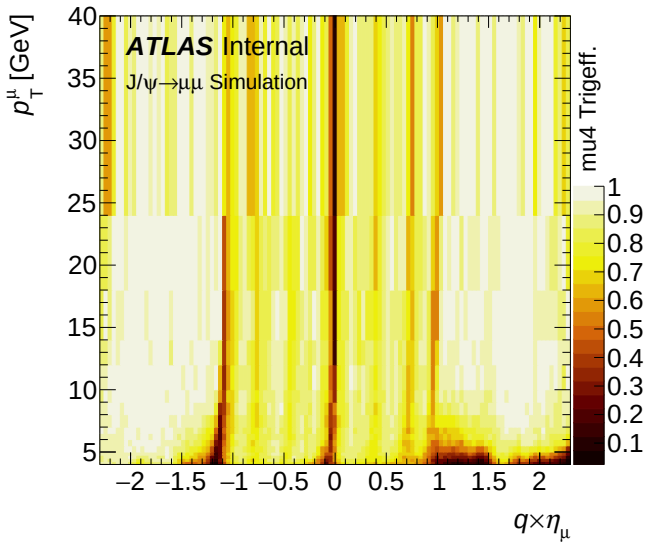

FIGURE 5.21: HLT_mu4 trigger efficiency with respect to reconstructed muons obtained from pp data using $J/\psi \rightarrow \mu^+\mu^-$ tag and probe method.

validation tools without biases from background processes which usually have different kinematic constrains from the signal processes.

The numbers of recovered J/ψ signals after trigger matching requirements and the weighting procedure are checked against the original number of reconstructed signals. The closure for each bin is defined by

$$C = \frac{\sum_{i=1}^{k} \omega_i}{N}. \tag{5.14}$$

where k is the number of J/ψ surviving from trigger requirements, N is the total number of reconstructed J/ψ signals and ω is the trigger weight of the selected J/ψ signal. A perfectly consistent set of weights would give a closure of 1.0. The error on the closure is calculated assuming a binomial correlation.

The closure test of HLT_mu4_mu4noL1 in $\mathrm{Pb} + \mathrm{Pb}$ is shown in Figure 5.23 and the closure test of HLT_2mu4_bJpsimumu in pp is shown in Fig. 5.24. As we can see the Pb+Pb dimuon trigger don't seems to be sensitive to the centrality as the single chains are, so not extra corrections are applied to account for this effect.

5.3 Acceptance

The acceptance of quarkonium decays to muon pairs are defined as the probability that the decay products fall within the fiducial volume ($p_{\mathrm{T}}(\mu^{\pm}) > 4$ GeV, $|\eta(\mu^{\pm})| < 2.4$). The acceptance depends on the spin-alignment of the quarknoium. Previous measurements in pp collisions suggest that produced quarkonium messons at the LHC energies are consistent with being unpolarized. Based on the assumption that the nuclear medium does not modify the average polarization of produced quarkonium, all quarkonium

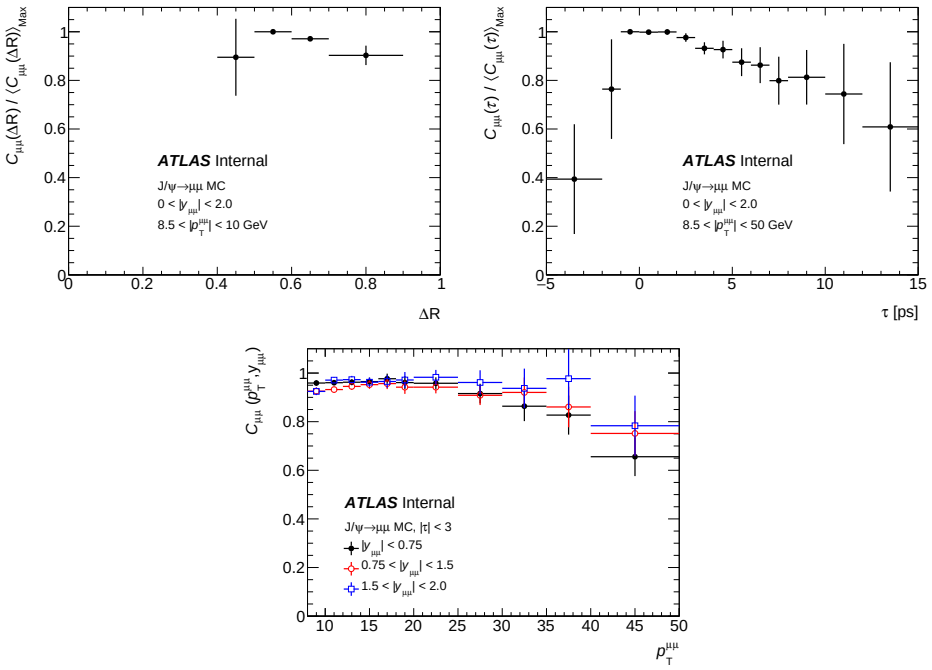

FIGURE 5.22: HLT_mu4 correction factor, $C_{\mu\mu}$, as a function of $\Delta R_{\mu\mu}$ (top, left), $\tau_{\mu\mu}$ (top. right), and transverse momentum (bottom).

states in both Pb+Pb and pp in this analysis are considered as unpolarized. For the ψ mesons studied in this analysis, 2D maps are produced as a function of the ψ p_{T} and $|y|$ for the set of spin-alignment hypotheses. The dependence of ψ production on the azimuthal angle ϕ is trivial for unpolarized incoming beams and has been integrated out. Acceptance maps are defined within the range $p_{\mathrm{T}}(\psi) < 50$ GeV, $|y(\psi)| < 2.4$ corresponding to the data considered in this analysis. The reconstructed candidates in data will cover a range of masses, corresponding to the detector resolution of the ψ mesons signal and non-signal background contributions. In order to apply the acceptance correction to the yields, a simple linear interpolation is used assuming the mass upper boundary for the J/ψ candidates to be 3.5 GeV and the mass lower boundary for the $\psi(2S)$ candidates to be 3.2 GeV. Within the interpolation range $[3.2\ \mathrm{GeV}, 3.5\ \mathrm{GeV}]$, the following function is applied to the acceptance correction:

$$\mathcal{A} = \mathcal{A}(J/\psi) \cdot \frac{3.5 - M_{\mu^+\mu^-}[\mathrm{GeV}]}{0.3} + \mathcal{A}(\psi(2S)) \cdot \frac{M_{\mu^+\mu^-}[\mathrm{GeV}] - 3.2}{0.3} \quad (5.15)$$

The 2D $J/\psi \to \mu\mu$ and $\psi(2S) \to \mu\mu$ acceptance maps for the FLAT hypothesis as a function of the ψ p_{T} and $|y|$ are shown in Figure 5.25. Each map is defined by 96 slices in absolute rapidity and 300 slices in p_{T}, using 10k trials for each point.

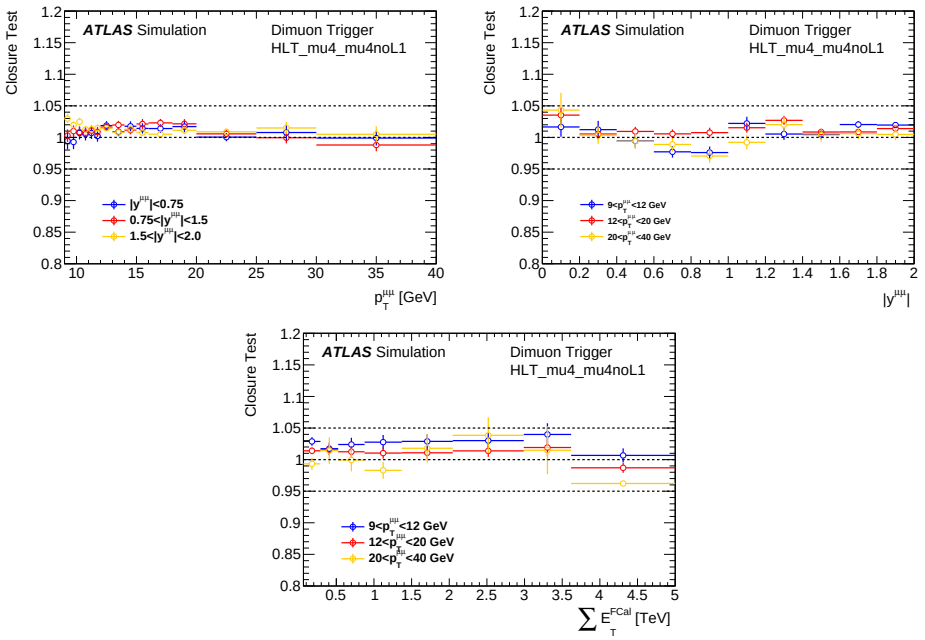

FIGURE 5.23: Closure test of HLT_mu4_mu4noL1 factorization in simulation as a function of J/ψ p_{T} (top,left), J/ψ $|y|$ (top,right), and event centrality (bottom).

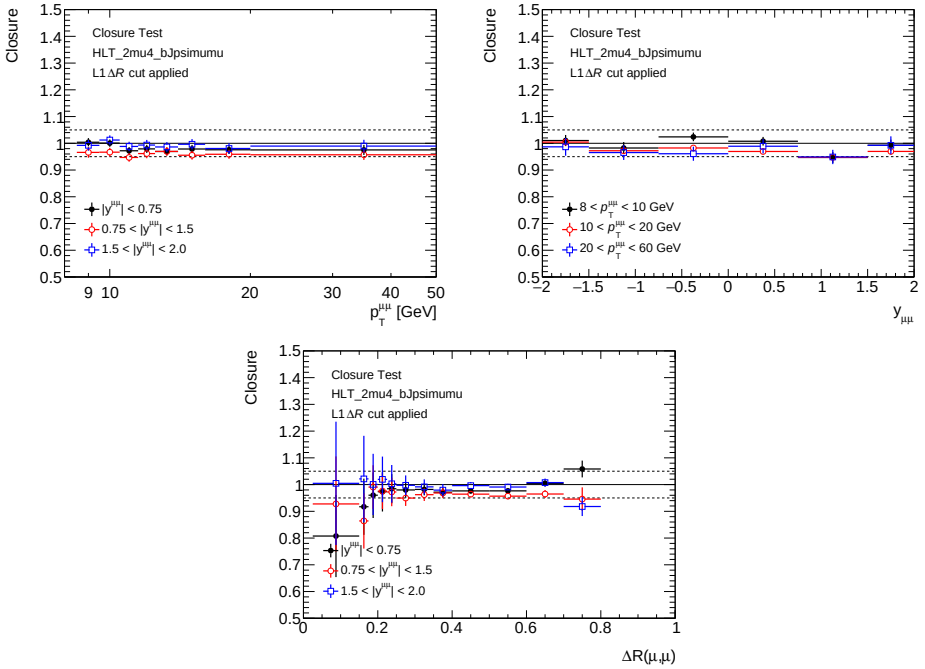

FIGURE 5.24: Closure test of HLT_2mu4_bJpsimumu factorization in simulation as a function of J/ψ p_{T} (top,left), J/ψ $|y|$ (top,right), and $\Delta R_{\mu\mu}$ (bottom).

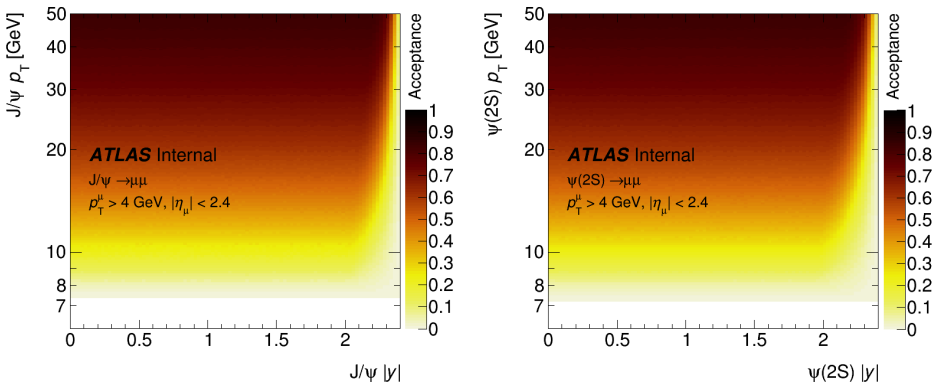

FIGURE 5.25: The unpolarised 2D acceptance map for $J/\psi \to \mu\mu$ (left) and $\psi(2S) \to \mu\mu$ (right).

Chapter 6

Analisys

6.1 Centrality definition

The centrality of Pb+Pb collisions is characterised by the sum of the transverse energy, $\sum E_{\mathrm{T}}^{\mathrm{FCal}}$, evaluated at the electromagnetic scale in FCal modules. It describes the degree of geometric overlap of two colliding nuclei in the plane perpendicular to the beam with large overlap in central collisions and small overlap in peripheral collisions.. Centrality intervals are defined in successive percentiles of the $\sum E_{\mathrm{T}}^{\mathrm{FCal}}$ distribution ordered from the most central (highest $\sum E_{\mathrm{T}}^{\mathrm{FCal}}$) to the most peripheral collisions. A Glauber model analysis of the $\sum E_{\mathrm{T}}^{\mathrm{FCal}}$ distribution was used to evaluate the mean nuclear thickness function, $\langle T_{\mathrm{AA}} \rangle$, and the number of nucleons participating in the collision, $\langle N_{\mathrm{part}} \rangle$, in each centrality interval [56, 7, 14]. The centrality intervals used in this measurement are indicated in Table 6.1 along with their respective calculations of $\langle T_{\mathrm{AA}} \rangle$ and $\langle N_{\mathrm{part}} \rangle$.

Centrality [%]	$\langle T_{\mathrm{AA}} \rangle$ $[mb^{-1}]$	$\langle N_{\mathrm{part}} \rangle$	N_{evt}
0-5	26.23 ± 0.22	384.4 ± 1.9	1.87×10^8
5-10	20.47 ± 0.19	333.1 ± 2.7	1.87×10^8
0-10	23.35 ± 0.20	358.8 ± 2.3	3.74×10^8
10-20	14.33 ± 0.17	264.0 ± 2.8	3.74×10^8
20-30	8.63 ± 0.17	189.1 ± 2.7	3.74×10^8
30-40	4.94 ± 0.15	131.4 ± 2.6	3.74×10^8
40-50	2.63 ± 0.11	87.0 ± 2.3	3.74×10^8
50-60	1.27 ± 0.07	53.9 ± 1.9	3.74×10^8
60-80	0.39 ± 0.03	22.9 ± 1.2	7.48×10^8
0-80	6.99 ± 0.10	141.3 ± 2.0	2.99×10^9

TABLE 6.1: The $\langle T_{\mathrm{AA}} \rangle$, $\langle N_{\mathrm{part}} \rangle$ and N_{evt} values and their uncertainties in each centrality bin.

6.2 Signal candidate selection

Muon candidates in Pb+Pb data samples are required to pass the "tight" muon working point selection [20] without any TRT selection (see Apendix C), as well as the following criteria:

- $p_{\mathrm{T}} > 4$ GeV and $|\eta| < 2.4$;
- pixel hits + inoperative pixel sensors > 0;

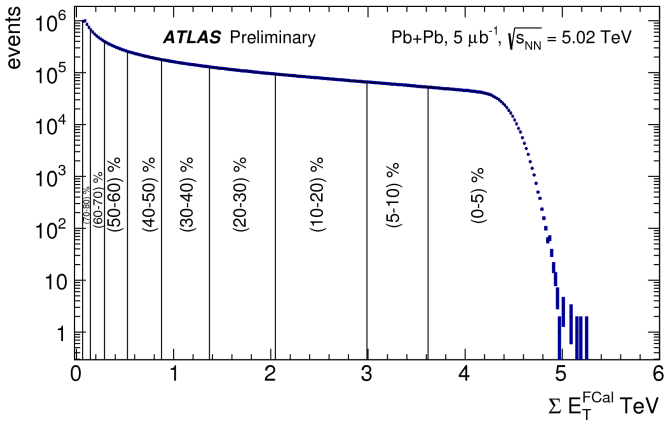

FIGURE 6.1: Measured $\sum E_T$ distribution in minimum-bias Pb+Pb collisions at $\sqrt{s_{NN}} = 5.02$ TeV.

- SCT hits + inoperative SCT sensors > 4;
- pixel holes + inoperative SCT sensors < 3;
- The selected muon must be consistent with having passed the trigger.

The selected muon pairs must be consistent with being originated from a common vertex, have opposite charges, and an invariant mass in the range $2.6 < m_{\mu\mu} < 4.2$ GeV. The charmonium candidate is further required to satisfy $p_{\mathrm{T}} > 9$ GeV to ensure that the pair candidates are reconstructed in a fiducial region where acceptance and efficiency corrections do not vary significantly relative to the magnitude of the systematic uncertainties quoted on the final results.

6.3 Observables determination

To distinguish prompt and non-prompt charmonium production, the pseudo-proper decay time, τ, is used, which is defined as:

$$\tau = \frac{L_{xy} m_{\mu\mu}}{p_{\mathrm{T}}^{\mu\mu}}, \tag{6.1}$$

where L_{xy} is the distance between the position of the reconstructed secondary vertex and the primary vertex projected onto the transverse plane. To determine the prompt and non-prompt cross sections, a weight, w_{total}, is defined for each selected dimuon candidate using the relation:

$$w_{\mathrm{total}}^{-1} = A \cdot \epsilon_{\mathrm{reco}} \cdot \epsilon_{\mathrm{trig}}, \tag{6.2}$$

where A is the acceptance, ϵ_{reco} is the reconstruction efficiency, and ϵ_{trig} is the trigger efficiency.

Then a two dimensional fit was performed to the invariant mass and pseudo-proper time distributions of weighted events to separate the background from the signal in order to determine the yields of the prompt and non-prompt charmonium components.

The differential cross sections for the production of prompt (p) and non-prompt (np) J/ψ and $\psi(2S)$ were calculated in another study and are defined as [15]:

$$\frac{d^2\sigma^{\mathrm{p(np)}}}{dp_{\mathrm{T}}dy} \times \mathrm{BR}(\psi(\mathrm{nS}) \to \mu\mu) = \frac{N^{\mathrm{p(np),\ corr}}_{\psi(\mathrm{nS})}}{\Delta p_{\mathrm{T}} \times \Delta y \times \int \mathcal{L} dt}, \tag{6.3}$$

where $\mathrm{BR}(\psi(\mathrm{nS}) \to \mu\mu)$ is the branching ratio for charmonium states decaying into two muons, and $N^{\mathrm{corr}}_{\psi(\mathrm{nS})}$ is the charmonium yield corrected for acceptance and detector effects. In the same way we define the per-event yield of charmonium states measured in A+A collisions as:

$$\left.\frac{d^2N^{\mathrm{p(np)}}}{dp_{\mathrm{T}}dy}\right|_{\mathrm{cent}} \times \mathrm{BR}(\psi(\mathrm{nS}) \to \mu\mu) = \frac{1}{\Delta p_{\mathrm{T}} \times \Delta y} \times \left.\frac{N^{\mathrm{p(np),\ corr}}_{\psi(\mathrm{nS})}}{N^{\mathrm{MB}}_{\mathrm{evt}}}\right|_{\mathrm{cent}}, \tag{6.4}$$

where $N^{\mathrm{MB}}_{\mathrm{evt}}$ is the number of minimum bias events.

6.3.1 Acceptance and efficiency corrections

The kinematic acceptance $A(p_{\mathrm{T}}, y)$ for a $\psi(\mathrm{nS})$ with transverse momentum p_{T} and rapidity y decaying into $\mu\mu$ was obtained from a MC simulation defined as the probability that both muons fall within the fiducial volume $p_T(\mu^{\pm}) > 4$ GeV, $|\eta(\mu^{\pm})| < 2.4$, assuming an unpolarised spin-alignment scenario [53, 2, 33], as described in section 5.3. Trigger and reconstruction efficiencies were calculated for both data and MC using the tag and probe method (T&P). The method is based on the selection of an almost pure muon sample from $J/\psi \to \mu\mu$ events, requiring one muon of the decay (tag) to be identified as the tight muon which triggered the readout of the event and the second muon (probe) to be reconstructed by a system independent of the one being studied, allowing a measure of the performance with a minimal amount of bias. Once the tag and probe sample is defined, the background contamination and the muon efficiency are measured with a simultaneous maximum-likelihood fit of two statistically independent distributions of the invariant mass: events in which the probe is or is not successfully matched to the selected muon [20, 25]. Both efficiencies have been evaluated as a function of p_T and η using muons from simulated $J/\psi \to \mu\mu$ decays. Muon reconstruction efficiency increases from low to high p_{T} and decrease from central to forward rapidities and from peripheral to central collisions as shown in figure 6.2. Its magnitude varies between 60% and 90%, becoming consistent with constant for $p_{\mathrm{T}} > 6$ GeV.

The dimuon trigger efficiency is studied and factorized in terms of single muon trigger efficiencies which increase from low to high p_{T} and from central to forward rapidities. Dimuon trigger efficiency vary from 50% up to 85%, between the lowest up to the highest dimuon p_{T}. To account for the difference between efficiency in simulation and experimental data, the data-to-MC ratio, $\epsilon^{\mathrm{data}}_{\mathrm{reco}}/\epsilon^{\mathrm{MC}}_{\mathrm{reco}}$, was parameterized as a function of p_{T} and centrality and applied as a multiplicative scale factor on the efficiency correction separately for the barrel and endcap systems. The magnitude of this scale factor varies between 1% to 5%. After applying this correction, the inverse average total weight, w^{-1}_{total}, used to correct the $\psi(\mathrm{nS})$ candidates is

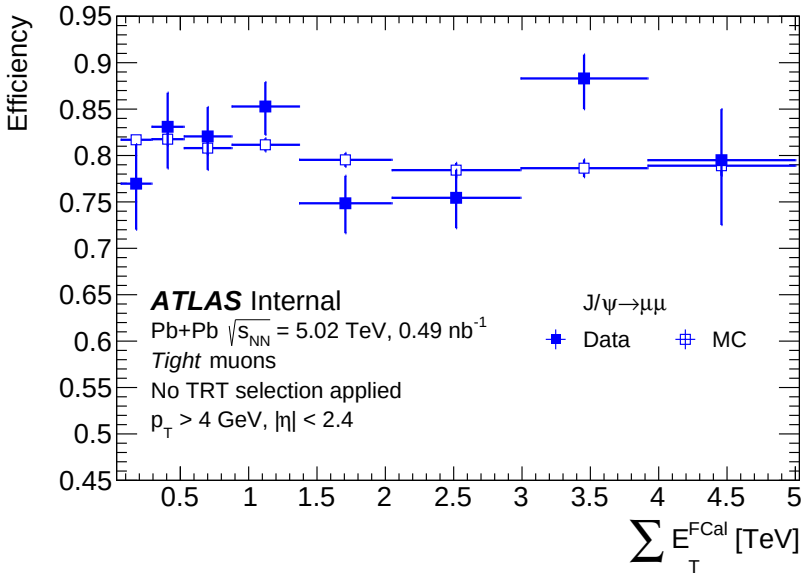

FIGURE 6.2: Muon reconstruction efficiency as a function of the summed transverse energy in the forward calorimeters, $\sum E_{\mathrm{T}}^{\mathrm{FCal}}$.

shown in the left panel of Figure 6.3, as a function of the dimuon transverse momentum and rapidity. Right panel of Figure 6.3 shows the breakdown of the total wight in each correction term.

6.3.2 Fit model

The corrected prompt and non-prompt $\psi(\mathrm{nS})$ yields are extracted from two-dimensional weighted unbinned maximum likelihood fits performed on invariant mass and pseudo-proper decay time distributions in each p_{T}, y or centrality interval. The probability distribution function (PDF) for the fit is defined as a normalised sum of seven terms, where each term is factorised into mass and decay time dependent functions; these functions are described in detail below. The PDF can be written in a compact form as:

$$\mathrm{PDF}(m,\tau) = \sum_{i=1}^{7} \kappa_i f_i(m) \cdot h_i(\tau) \otimes g(\tau), \tag{6.5}$$

where κ_i is the normalisation factor of each component, $f_i(m)$ and $h_i(\tau)$ are distribution functions for the mass m and the pseudo-proper time τ respectively; $g(\tau)$ is the resolution function described with a double Gaussian; and the "$\otimes$" symbol implies a convolution. The composite PDF terms are defined by a Crystal Ball function (CB) [58], Gaussian (G) and exponential (E) distributions; individual components are shown in Table 6.2.

The fit is performed using the RooFit framework [67]. In order to stabilise the fit model, and reduce the correlation between parameters, a number of component terms share common parameters, or use a free scaling parameter. The default fit model is described below.

The signal mass shapes are described by the sum of a CB and a single Gaussian. For the J/ψ and $\psi(2\mathrm{S})$ the CB and Gaussian share a common

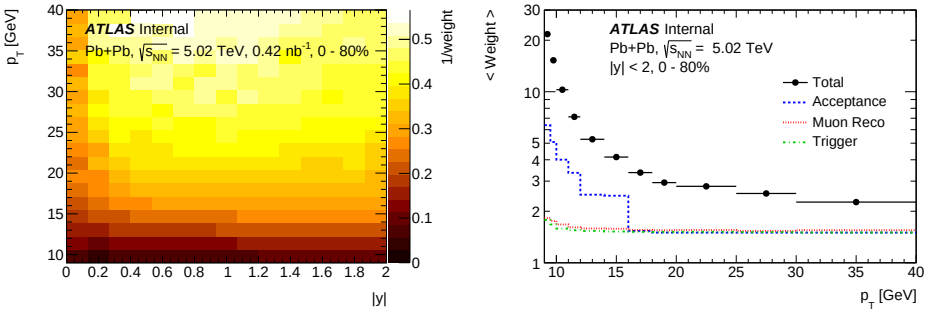

FIGURE 6.3: (Left) Inverse average total weight as a function of the dimuon transverse momentum and rapidity for integrated centrality, measured in simulation and corrected for differences between efficiency in simulation and experimental data. Decreases in efficiency at very central rapidity correspond to the $|\eta| < 0.1$ region not covered by the muon detectors. The total size of the weight is dominated by the acceptance correction. (Right) Average contribution of is correction to the total weight.

mean. The width term in the CB function is equal to the Gaussian standard deviation times a free scaling term that is common for the J/ψ and $\psi(2S)$. The CB left-tail and height parameters are fixed, and variations of the two parameters are considered as part of the fit model systematic uncertainties. The mean of the Gaussian of the $\psi(2S)$ is set to be the mean of the J/ψ multiplied by $m_{\psi(2S)}/m_{J/\psi} = 1.190$ [57]. The width of the Gaussian of the $\psi(2S)$ is also set to be the width of the J/ψ multiplied by the same factor; variations of this scaling term are considered as part of the fit model systematic uncertainties. The relative fraction of the CB and the Gaussian is free, but common between the J/ψ and $\psi(2S)$.

The non-prompt signal pseudo-proper decay time PDFs are described by a single sided exponential convolved with a double Gaussian lifetime resolution function. The double Gaussian resolution function has a fixed mean at $\tau = 0$ and free widths with the fraction between the two single

i	Type	Source	$f_i(m)$	$h_i(\tau)$
1	J/ψ	P	$\omega_i \mathrm{CB}_1(m) + (1-\omega_i)\mathrm{G}_1(m)$	$\delta(\tau)$
2	J/ψ	NP	$\omega_i \mathrm{CB}_1(m) + (1-\omega_i)\mathrm{G}_1(m)$	$\mathrm{E}_1(\tau)$
3	$\psi(2S)$	P	$\omega_i \mathrm{CB}_2(m) + (1-\omega_i)\mathrm{G}_2(m)$	$\delta(\tau)$
4	$\psi(2S)$	NP	$\omega_i \mathrm{CB}_2(m) + (1-\omega_i)\mathrm{G}_2(m)$	$\mathrm{E}_2(\tau)$
5	Bkg	P	$\mathrm{E}_3(m)$	$\delta(\tau)$
6	Bkg	NP	$\mathrm{E}_4(m)$	$\mathrm{E}_5(\tau)$
7	Bkg	NP	$\mathrm{E}_6(m)$	$\mathrm{E}_7(\lvert\tau\rvert)$

TABLE 6.2: PDFs for individual components in the default fit model used to extract the prompt and non-prompt contribution for J/ψ and $\psi(2S)$ signal (S) and background (Bkg). ω_i is the normalisation factor of the CB component with respect to the CB+G signal and $\delta(\tau)$ is the Dirac delta function.

Gaussian components fixed. The same resolution function is used to describe the prompt contribution by convolving it with a delta function.

The pseudo-proper decay time PDFs describing the background are represented by the sum of one prompt component and two non-prompt components. The prompt background component is described by a delta function convolved with a double Gaussian function. While one of the non-prompt background contributions is described by a single-sided decay model (for positive τ only), the other is described by a double-sided decay model accounting for candidates of mis-reconstructed or non-coherent dimuon pairs. The same Gaussian resolution functions are used for the background as for the signal. For the background parameterisations in the mass distribution, the single-sided non-prompt contribution is modelled by an exponential. The prompt mass background contribution follows a flat distribution, and the double-sided background is modelled with an exponential. As validation of our fit model, figure 6.4 shown the fit projections for a mass selection of $2.6 < m_{\mu\mu} < 2.85$ allowing us to check that the proper-time background is well modelled.

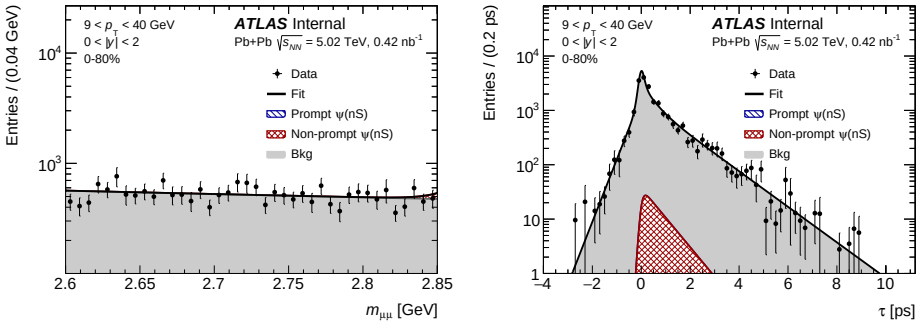

FIGURE 6.4: Dimuon invariant mass of the charmonia mass range $2.6 < m_{\mu\mu} < 2.85$ GeV (left) and dimuon pseudo-proper lifetime (right). The data shown are for the range $9 < p_{\mathrm{T}} < 40$ GeV, $|y| < 2.0$ and 0-80% centrality in Pb+Pb collisions. Superimposed on the data are the projections of the fit results.

Example plot of fit projections is shown in Figure 6.5. The important quantities extracted from the fit are: the fraction of signal; the fraction of signal that is prompt; the fraction of the prompt signal that is $\psi(2\mathrm{S})$; and the fraction of non-prompt signal that is $\psi(2\mathrm{S})$. From these parameters, the covariance matrix of the fit and the weighted sum of entries, all measured values are extracted.

6.3.3 Observables

The suppression of charmonium states is quantified by the nuclear modification factor which can be defined for a given centrality class as:

$$R_{\mathrm{AA}} = \frac{N_{\mathrm{AA}}}{\langle T_{\mathrm{AA}} \rangle \times \sigma_{pp}}, \tag{6.6}$$

where N_{AA} is the per-event yield of charmonium states measured in A+A collisions, $\langle T_{AA} \rangle$ is the mean nuclear thickness function and σ_{pp} is the cross

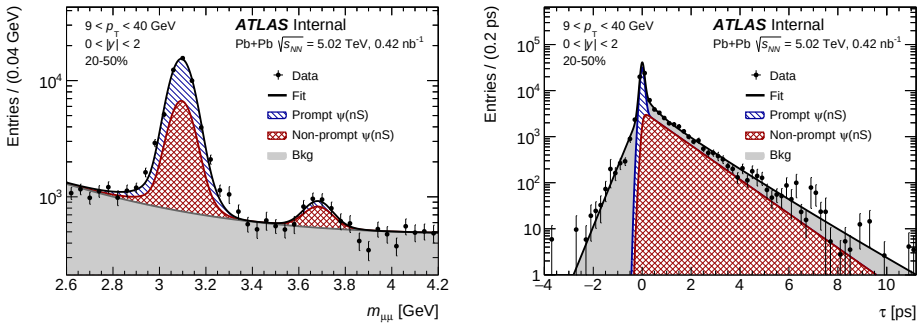

FIGURE 6.5: Dimuon invariant mass of the full charmonia mass range $2.6 < m_{\mu\mu} < 4.2$ GeV (left) and dimuon pseudo-proper lifetime (right). The data shown are for the range $9 < p_{\mathrm{T}} < 40$ GeV, $|y| < 2.0$ and 20-50% centrality in Pb+Pb collisions. Superimposed on the data are the projections of the fit results.

section for the production of the corresponding charmonium states in pp collisions at the same energy [15]. To quantify the production of $\psi(2\mathrm{S})$ relative to J/ψ a ratio of nuclear modification factors, $\rho^{\psi(2S)/J/\psi}_{\mathrm{PbPb}} = R^{\psi(2\mathrm{S})}_{\mathrm{AA}}/R^{J/\psi}_{\mathrm{AA}}$, can be used. However, in this analysis the numerator and denominator are not calculated directly from Eq. 6.6, rather, it is advantageous to calculate it in the equivalent form as:

$$\rho^{\psi(2S)/J/\psi}_{\mathrm{PbPb}} = (N_{\psi(2S)}/N_{J/\psi})_{\mathrm{Pb+Pb}}/(N_{\psi(2S)}/N_{J/\psi})_{pp} \tag{6.7}$$

In this formulation the systematic uncertainties will be minimised due to a substantial cancellation of the trigger and reconstruction efficiencies for the two quarkonia systems, since they are very similar in mass and they are measured in the identical final state channel.

The non-prompt fraction, f_{NP}, is also measured, which is defined as the number of non-prompt charmonia relative to the number of inclusively produced charmonia:

$$f^{\psi(\mathrm{nS})}_{\mathrm{NP}} = \frac{N^{\mathrm{np,corr}}_{\psi(\mathrm{nS})}}{N^{\mathrm{np,corr}}_{\psi(\mathrm{nS})} + N^{\mathrm{p,corr}}_{\psi(\mathrm{nS})}}, \tag{6.8}$$

where the non-prompt fraction can be determined for the J/ψ and $\psi(2\mathrm{S})$ simultaneously. This observable has the advantage that acceptances and efficiencies are similar for the numerator and denominator, and thus systematic uncertainties are reduced in the ratio.

6.4 Systematic uncertainties

The main sources of systematic uncertainties in this measurement are the assumptions in the fitting procedure, the acceptance and efficiency calculations, and the pp luminosity and $\langle T_{AA} \rangle$ determination. As the acceptance depends on the spin-alignment state of the $\psi(nS)$ and hence affects the corrected yield, six scenarios are considered in order to assign an uncertainty due to the unknown spin-alignment. Since the polarization of charmonia in

pp was measured to be small [53, 2, 33], its modification due to the nuclear environment is neglected and the spin-alignment uncertainty is assumed to cancel in R_{AA} and $\rho_{\mathrm{PbPb}}^{\psi(2S)/J/\psi}$. Changes in the yields due to bin migration effects are at the per-mil level and thus no correction is needed. Table 6.4 shows the contributions of the systematic uncertainties of three measured observables. The total systematic uncertainty is calculated by summing the different contributions in quadrature and were derived separately for pp and Pb+Pb results. The yield extraction uncertainties increase from central to forward rapidity, and from high to low p_T where the dominant source of systematic uncertainty is the muon reconstruction. The double R_{AA} ratio has a substantially larger fit uncertainty than the other observables; this is because the signal-to-background ratio for the $\psi(2\mathrm{S})$ is much smaller than for the J/ψ.

6.4.1 pp luminosity and $\langle T_{\mathrm{AA}} \rangle$ uncertainty

The integrated luminosity determined for the 2015 pp data has been calibrated based on data from dedicated beam-separation scans, also known as van der Meer scans. Similar systematic uncertainties to those examined in the 2012 pp luminosity calibration [16] were studied in order to assess the systematic uncertainties for the 2015 data. The combination of these systematic uncertainties results in a final uncertainty on the ATLAS luminosity during pp collisions at $\sqrt{s} = 5.02$ TeV of $\delta\mathcal{L}/\mathcal{L} = \pm 5.4\%$. The uncertainty on the nuclear overlap function, $\langle T_{\mathrm{AA}} \rangle$, is estimated by varying the Glauber model parameters and is show in table 6.1.

6.4.2 Reconstruction efficiency uncertainty

Several sources of uncertainty have been evaluated to determine the systematic uncertainties of the muon reconstruction efficiency Pb+Pb data, independently for the ID and the MS component:

- Uncertainty in the fit of the data to MC ratio.
- Signal and background fit model used to extract data efficiency are changed to assess systematic uncertainties related to the choice of the signal and background PDFs:
  - Chebychev polynomial is used instead of exponential function for background model variation.
  - Single Gaussian function is used instead of weighted sum of Gaussian and CB functions for signal mass resolution model variation.
- Truth closure test: difference between truth muon efficiency and efficiency determined using TnP method in MC is also assigned as systematic uncertainty.

6.4.3 Trigger efficiency uncertainty

Several sources of uncertainty have been evaluated as systematic uncertainties of muon trigger efficiency in Pb+Pb data:

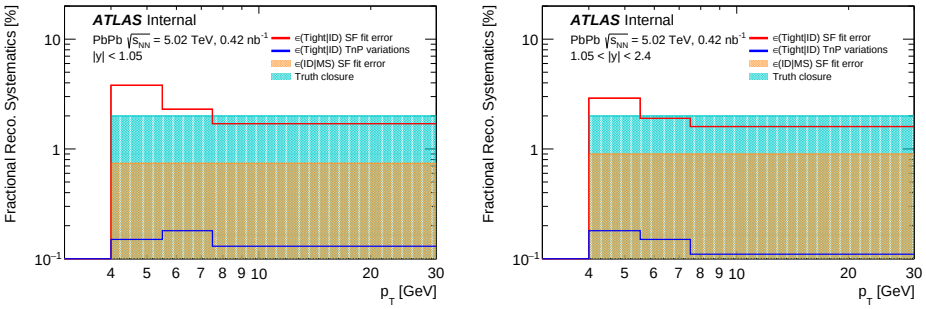

FIGURE 6.6: The fractional systematic uncertainty on the muon reconstruction efficiency scale factor as a function of muon p_T for barrel region (left) and end-cap region (right).

- Statistical uncertainties of data used in the scale factor calculation.
- Charge asymmetry: difference in efficiency between positive and negative muons.
- Signal and background fit model used to extract data efficiency are changed to assess systematic uncertainties related to the choice of the signal and background PDFs:
  - 3rd order polynomial is used instead of exponential function for background model variation.
  - Single Gaussian function is used instead of weighted sum of Gaussian and CB functions for signal mass resolution model variation.
- For the nominal fit, the mean and standard deviation of the CB and Gaussian distributions for the mass are the same; as a systematic variation they are allowed to be different.
- an extra 5% correlated uncertainty is added to cross-section observable to cover the non-closure of the dimuon chain factorization. But cancelled in the $\psi(2S)$ to J/ψ ratio.

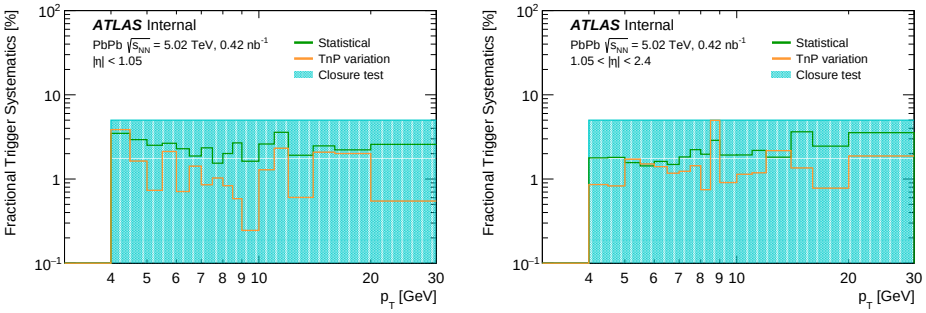

FIGURE 6.7: The fractional systematic uncertainty on the muon trigger efficiency scale factor from different sources as a function of muon p_T for barrel region (left) and end-cap region (right).

6.4.4 Bin migration

The bin migration effect has been studied using a HIJING MC sample. We study the migration between bins in transverse momentum and rapidity of J/ψ used in this analysis. We compare the number of J/ψ from the truth-level muons in the generated event to J/ψ formed from the reconstructed muons. For these muons we require both generated and reconstructed transverse momentum greater than 4 GeV and the invariant mass of the pair must be reconstructed in the range $2.8 < m_{\mu\mu} < 3.4$ GeV. Bin migration in Pb+Pb collisions was found to have a maximum value of < 2 % with an average value that is much smaller (see figure 6.8) so no corrections are included to take this effect into account. The corresponding quantity in pp collisions, where the tracking resolution is of higher quality, is completely negligible.

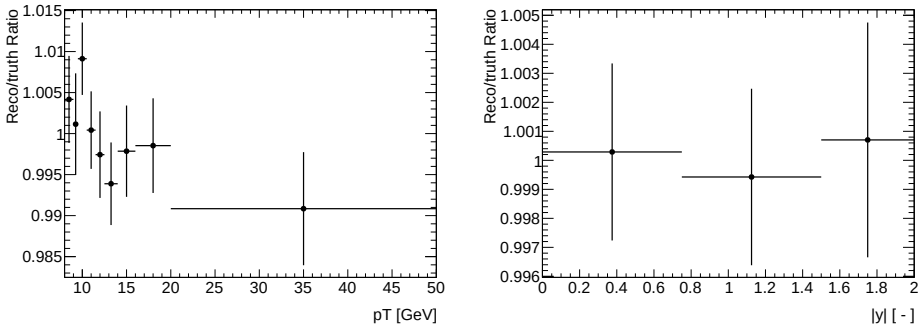

FIGURE 6.8: Reconstructed to truth J/ψ ratio, as a function p_T (left) and | y | (right).

6.4.5 Fit model uncertainty

Two different kinds of uncertainties are associated to the fitting procedure, uncertainty due to the fixation of some of the parameter and uncertainty due to choosing a particular PDF.
The uncertainty due to fixation of parameter is estimated with a closure test based in pseudo-experiments, in each experiment a weight between 0.5 and 2 is applied to the non-prompt MC. Then it is mixed with an unweighted prompt MC, this allow us to map the full set of values of the non-prompt fraction observed in data. Then the fit is performed, the fractional difference between input and output yields are assigned as systematic uncertainty, see Figure 6.10.
The uncertainty due to choosing a particular PDF is evaluated in pseudo-experiments. In each experiment, a bootstrap method is used to generate a toy samples based the fluctuation of the original data. To be more specific, every event from the original data will be filled into the toy sample n times, where n is a random integer number obtained from a Poisson distribution with μ = 1. Then the nominal mode and a set of variation models are fitted to the toy sample, and all measured quantities are recalculated and the shift between nominal model and certain variation model is extracted. After repeat the pseudo-experiment many times, the variation systematic uncertainty is defined as the mean shift of certain varied model from the

nominal model. The root mean square of all variations is then assigned as the fit model systematic uncertainties, see Figure 6.9. The following variations on the nominal model are considered:

- Signal mass PDF: By replacing the CB plus Gaussian with the double Gaussian function, and varying parameters of the CB model, which were originally fixed.
- Signal decay time PDF: A single exponential was changed to a double exponential.
- Background mass PDFs: By varying the functions from exponentials to 2^{nd} order Chebyshev polynomial to describe the prompt, non-prompt and double-sided background terms.
- Decay time resolution: By using a single Gaussian in place of the double Gaussian.

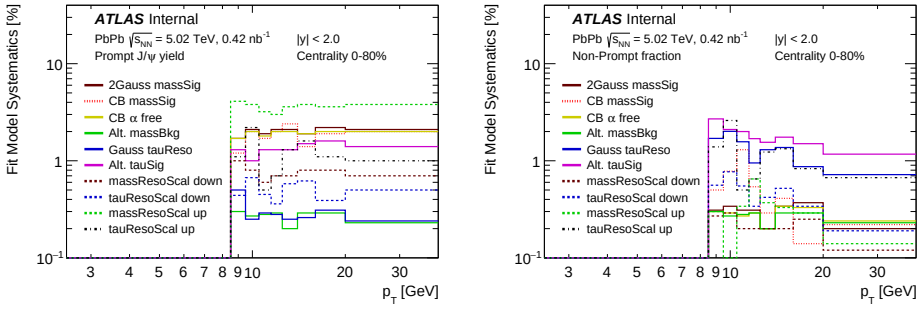

FIGURE 6.9: Charmonium fit model systematic uncertainties on two observable for all model variation for a selected kinematic range in Pb+Pb collisions.

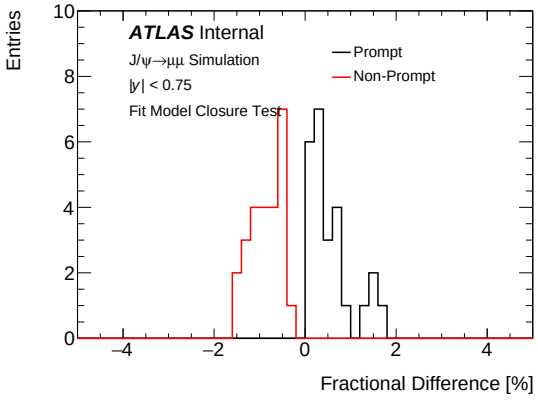

FIGURE 6.10: Fitting closure test.

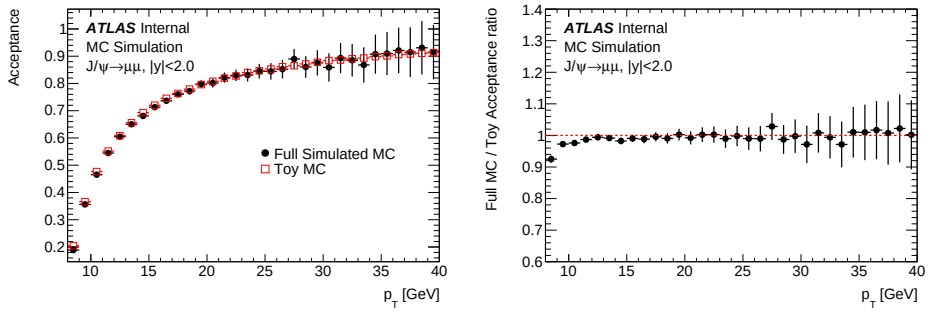

FIGURE 6.11: acceptance of $J/\psi \to \mu\mu$ as a function of J/ψ p_{T} from full simulated MC and toy MC (left) and the acceptance ratio from full simulated MC to that from toy MC (right).

6.4.6 Acceptance

FSR correction uncertainty

The central acceptance maps are produced by toy MC programs in which the final state radiation (FSR) is not included. Missing FSR would lead to an overestimation of quarkonium acceptance especially at low p_{T} where a lot of muons from quarkonium decay have p_{T} close to the fiducial single muon p_{T} cut. On the other hand, one has to rely on the toy MC acceptance since there were muon p_{T} and η cut applied in full MC at generator level, such that one cannot obtain the full phase space acceptance. A comparison of acceptance obtained from full simulated MC and toy MC is shown in Figure 6.11, the same phase space muon p_{T} and η cuts applied to the full simulated MC ($p_{\mathrm{T}} > 2.5$ GeV, $|\eta| < 2.7$ for $J/\psi \to \mu\mu$ MC) are applied to the toy MC for purpose of comparison. The FSR effects show a strong dependence on p_{T} as expected. The FSR correction is defined as:

$$C_{\mathrm{FSR}} = \frac{\omega_{\mathrm{acc}}(p_{\mathrm{T}}; \text{full MC})}{\omega_{\mathrm{acc}}(p_{\mathrm{T}}; \text{toy MC})} \tag{6.9}$$

where ω_{acc} is the average acceptance weight assigned to data sample. The following sources are considered as the FSR correction systematic uncertainties:

- statistical uncertainties propagated from full simulated MC sample which is found to be negligible;
- difference between FSR correction factors obtained with excited and ground quarkonium state enriched data sample. The size of this effect is found to be less than 0.5% therefore it's ignored.
- the difference between full simulated MC and toy MC is almost in dependent of quarkonium rapidity as shown in Figure 6.12, so the rapidity dependence is ignored for obtaining FSR corrections and the residual effect is included in systematic uncertainties of FSR correction.

The final FSR correction factors with full systematics are given in Figure 6.13. The Pb+Pb data at $\sqrt{s} = 5.02$ TeV are used for obtaining the correction, and

the same FSR corrections are applied to pp and Pb+Pb data. The systematic uncertainties due to FSR effect are fully cancelled in ratio observables in the same dataset and between different datasets. Validation of the FSR correction to the acceptance is detailed in appendix F.

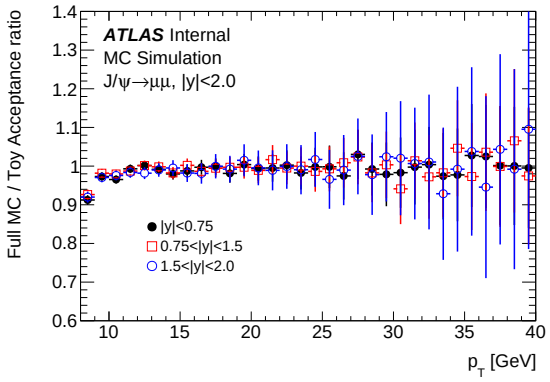

FIGURE 6.12: Acceptance ratio from full simulated MC to that from toy MC in 3 rapidity slices.

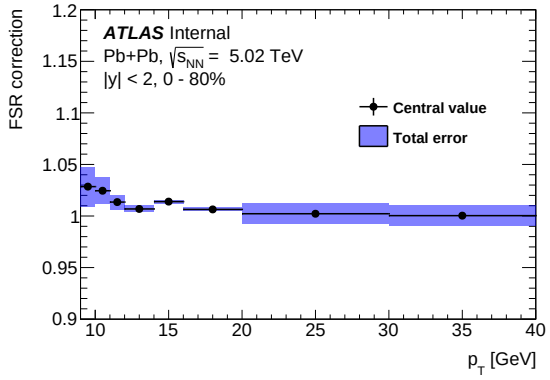

FIGURE 6.13: The derived FSR correction factor for charmonium candidates.

Interpolation uncertainty

Uncertainty introduced by the acceptance interpolation describe in Equation 5.15. An artificial slope is introduced to the background that is not correctly manage by the fitting procedure when the signal/background ratio is too small. This bias has a stronger effect in the $\psi(2S)$ signal determination when p_T is low or collisions are too central, see Figure 6.14.

6.4.7 Spin-alignment

The acceptance also depends on the spin-alignment of the J/ψ, which is not known for LHC conditions. The general angular distribution for the decay

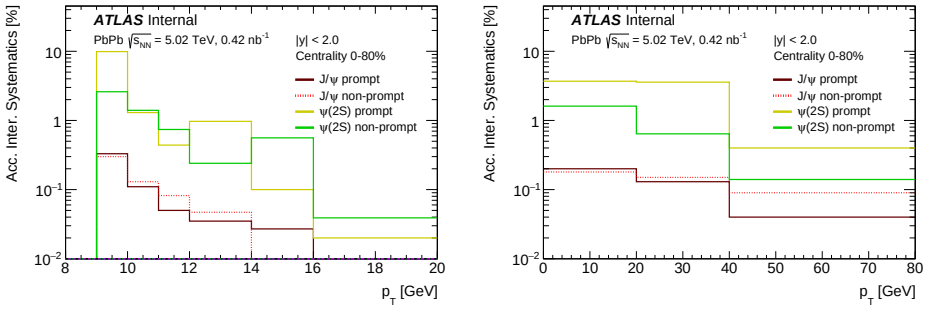

FIGURE 6.14: Acceptance interpolation uncertainty as a function of (left) charmonia p_T and (right) centrality in Pb+Pb collisions.

$J/\psi \to \mu\mu$ in the J/ψ decay frame is given by:

$$\frac{d^2N}{d\cos\theta^* d\phi*} \propto 1 + \lambda_\theta \cos^2\theta^* + \lambda_\phi \sin^2\theta^* \cos 2\phi^* + \lambda_{\theta\phi} \sin 2\theta^* \cos\phi^* \qquad (6.10)$$

where θ^* is the angle between the direction of the positive muon momentum in the J/ψ decay frame and the J/ψ line of flight, while ϕ^* is defined as the angle between the J/ψ production and decay planes in the lab frame (see figure 6.15).

A large number of possible combinations of the coefficients λ_θ, λ_ϕ, $\lambda_{\theta\phi}$ have been studied. Seven extreme cases have been identified that lead to the biggest variation of acceptance within the kinematics of the ATLAS detector and define an envelope in which the results may vary under all possible polarisation assumptions:

1. Isotropic distribution, independent of θ^* and ϕ^*, with $\lambda_\theta = \lambda_\phi = \lambda_{\theta\phi} = 0$, labelled as "Unpolarised". This is used as the main (central) hypothesis.

2. Full longitudinal alignment with $\lambda_\theta = -1$, $\lambda_\phi = \lambda_{\theta\phi} = 0$, labelled as “Longuitudinal”.

3. Transverse alignment with $\lambda_\theta = +1$, $\lambda_\phi = \lambda_{\theta\phi} = 0$, labelled as "Transverse 0".

4. Transverse alignment with $\lambda_\theta = +1$, $\lambda_\phi = +1$, $\lambda_{\theta\phi} = 0$, labelled as "Transverse P".

5. Transverse alignment with $\lambda_\theta = +1$, $\lambda_\phi = -1$, $\lambda_{\theta\phi} = 0$, labelled as "Transverse M".

6. Off-plane alignment with $\lambda_\theta = \lambda_\phi = 0$, $\lambda_{\theta\phi} = +0.5$, labelled as "Off-plane P".

7. Off-plane alignment with $\lambda_\theta = \lambda_\phi = 0$, $\lambda_{\theta\phi} = -0.5$, labelled as "Off-plane M".

Two-dimensional acceptance maps are produced in bins of p_{T} and y of the J/ψ, for each of these five scenarios, and are illustrated in figure 6.16.

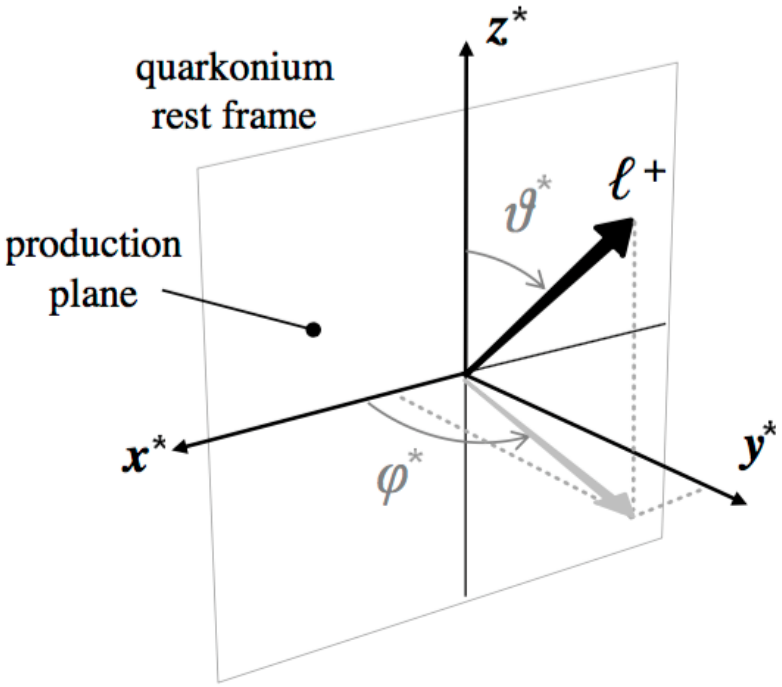

FIGURE 6.15: Definitions of the J/ψ spin-alignment angles, in the ψ decay frame. θ^* is the angle between the direction of the positive muon in that frame and the direction of J/ψ in the laboratory frame, which is directed along the z^*-axis. ϕ^* is the angle between the J/ψ production ($x^* - z^*$) plane and its decay plane formed by the direction of the J/ψ and the lepton l^+ (from [41]).

6.4.8 Uncertainties propagation

Yields systematic uncertainties

The statistical component of the uncertainties associated with the determination of ϵ_{reco} and ϵ_{trig} scale factors, is propagated to the yields using a series of pseudo-experiments. For each pseudo-experiment the SF is randomly varied according to the statistical uncertainty. After repeating the pseudo-experiment N times, the systematic uncertainty is defined as the mean of the shift of the varied yields with respect to the nominal case. The systematic component of the uncertainties associated with the determination of ϵ_{reco} and ϵ_{trig} scale factors and the FSR correction of the acceptance, is propagated on the yields by varying the SF, up/down, according with maximum and minimum value of the systematic uncertainty in each bin, and calculating a new weight , $w_{\uparrow\downarrow}$ define as:

$$w_{\uparrow\downarrow} = \frac{1}{\epsilon_{\text{nom}} \pm \delta(\text{syst.})} \tag{6.11}$$

The systematic uncertainty of the yield is then calculated with the following expression in each bin analysed.

$$\text{Syst.} \uparrow\downarrow [\%] = \frac{|N(w_0) - N(w_{\uparrow\downarrow})|}{N(w_0)} \tag{6.12}$$

Source	Propagated as:
Trigger	Uncorrelated
Reconstruction	Uncorrelated
Fitting	Partially correlated
Acceptance	Correlated
Lumi, T_{AA}	Uncorrelated

TABLE 6.3: Summary table of R_{AA} systematic uncertainties propagation.

where, w_0 is the nominal weight and $w_{\uparrow\downarrow}$ are the maximum and minimum systematic variation. Systematic uncertainty from T_{AA} and fitting procedure are applied directly in the final expression. Fractional systematic uncertainties of each sources are show in Figure 6.17, the nature of the asymmetry in the systematic uncertainties is described in appendix E.

R_{AA} systematic uncertainties

Uncertainties of the R_{AA} can be categorised into two classes depending in how they are propagated from the Pb+Pb and pp yields to the R_{AA}. Trigger, reconstruction and normalisation uncertainties are treated as uncorrelated. pp and Pb+Pb used different trigger sequences in the event selection, in pp we used the doble RoI dimuon trigger HLT_2mu4 while in Pb+Pb we used the asymmetric RoI-FS dimuon trigger HLT_mu4_mu4noL1, both trigger have different L1 and logic sequences so no correlation should be expected. Muon selection in pp and Pb+Pb is different as well, in the pp sample muons are required to pass the standard tight selection while in Pb+Pb the tracking selection is relaxed by no applying TRT requirement, this because the saturation of the sub-detector observed in the Pb+Pb collisions. On top of that a degradation of the tracking efficiency is observed when we move to high values of $|\eta|$ (endcaps), associated with the typical high multiplicity of the Pb+Pb collision in the forward/backward directions. No correlation is expected in reconstruction uncertainties. Same for the normalisation terms, integrated luminosity in pp and T_{AA} in Pb+Pb as they have no relations between each other.
Fitting uncertainty was studied using pseudo-experiment, as is explained in section 6.4.5, simultaneously in pp and Pb+Pb. The uncertainty was found partially correlated.
The acceptance uncertainty was propagated as correlated as this correction is exactly the same for both pp and Pb+Pb samples.
For uncorrelated uncertainties, the uncertainty was propagated using the usual method:

$$\delta R_{\mathrm{AA}}|_U \equiv \frac{A}{B}\sqrt{(\frac{\delta A}{A})^2 + (\frac{\delta B}{B})^2} \tag{6.13}$$

While for correlated uncertainties, the uncertainty was propagated using the method:

$$\delta R_{\mathrm{AA}}|_C \equiv \frac{A \pm \delta A}{B \pm \delta B} - \frac{A}{B} \tag{6.14}$$

Summary of each systematic uncertainty component propagation is shown in table 6.3.

Source	J/ψ pp cross sec. Uncorr.	Corr.	J/ψ Yield in Pb+Pb Uncorr.	Corr.	$R_{\mathrm{AA}}^{J/\psi}$ Uncorr.	Corr.	$R_{\mathrm{AA}}^{\psi(2S)}/R_{\mathrm{AA}}^{J/\psi}$ Uncorr.
Trigger	1 - 3%	5%	2 - 4%	3%	5 - 6%	5.8%	$< 1\%$
Recons.	4 - 6%	1%	4 - 5%	2%	6 - 7%	2.2%	$< 1\%$
Fitting	1%	1%	1 - 2%	1%	1 - 2%	1.1%	8 - 9%
T_{AA}	–	–	1 - 8%	–	1 - 8%	–	–
Migration	–	$< 1\%$	–	$< 1\%$	–	$< 1\%$	–
Accep.	$< 1\%$	–	1%	–	$< 1\%$	–	1 - 4%
Spin-Alig.	10 - 50%	–	10 - 50%	–	–	–	–
Luminosity	–	5.4%	–	–	–	5.4%	–

TABLE 6.4: Systematic uncertainties of the J/ψ pp cross section, J/ψ yield in Pb+Pb, $R_{\mathrm{AA}}^{J/\psi}$ and $R_{\mathrm{AA}}^{\psi(2S)}/R_{\mathrm{AA}}^{J/\psi}$ measured in Pb+Pb collisions. "Uncorrelated" refers to bin-to-bin uncorrelated uncertainties and "Correlated" refers to global uncertainties from various sources.

6.4.9 Summary of systematic uncertainties

Table 6.4 shows the contributions of the systematic uncertainties of various observables. The total systematic uncertainty is estimated by summing the different contributions in quadrature. The yield extraction uncertainties increase from central to forward rapidity, and also from high to low p_T where the dominant source of systematic uncertainty is the muon reconstruction as in shown in figure 6.17 together with the other systematic sources. The double R_{AA} ratio has a substantially larger fit uncertainty than the other observables; this is because the signal-to-background ratio for the $\psi(2\mathrm{S})$ is much smaller than for the J/ψ, adversely affecting the fits.

In all the results shown in Figures 7.6 to 7.11, statistical uncertainties are represented by error bars and systematic uncertainties by boxes on the points. Uncertainties coming from trigger, reconstruction and fitting closure test are consider as a global systematic uncertainties and are plotted by separated in a bar at y-axis = 1 of the relevant figures.

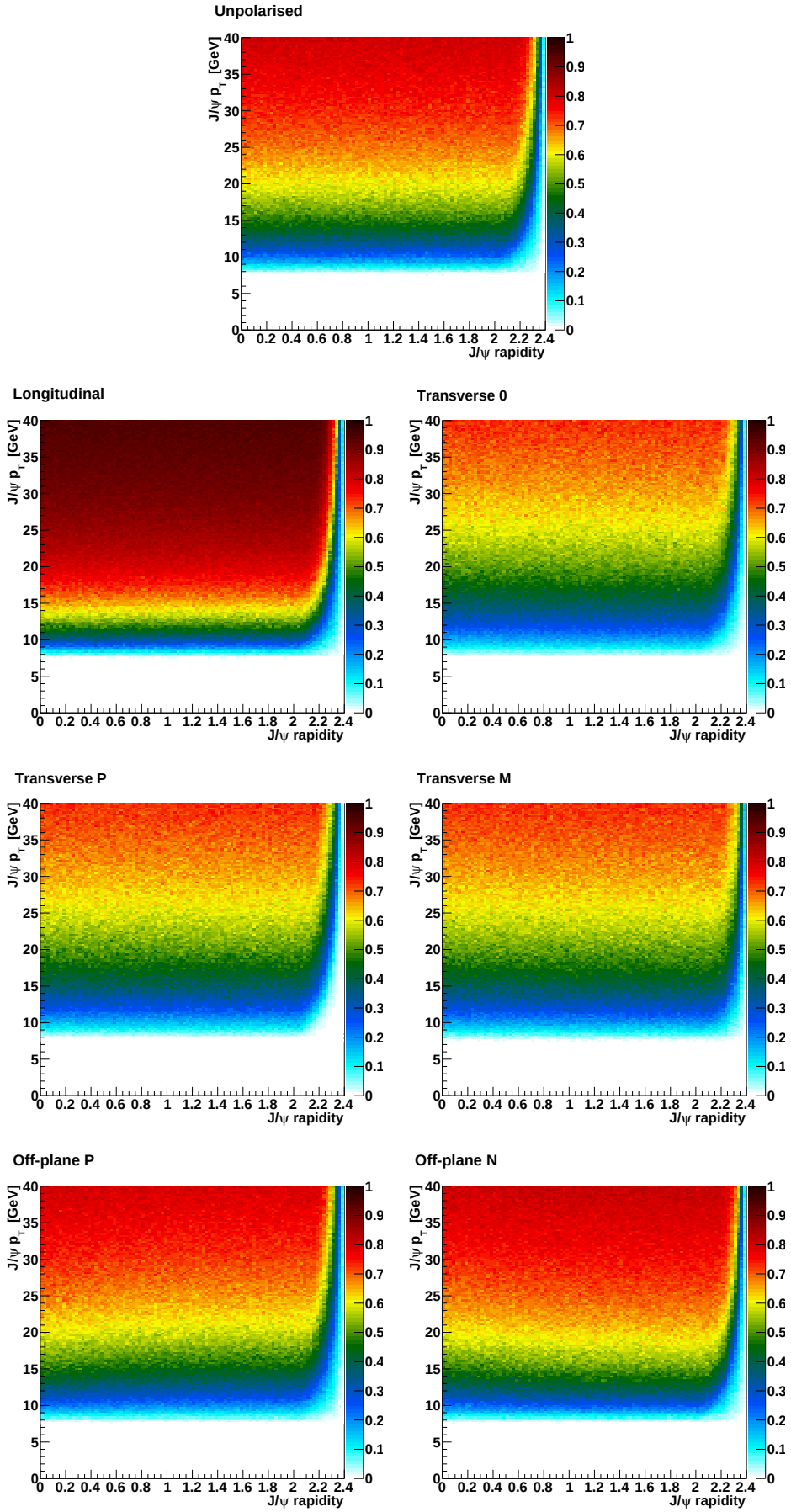

FIGURE 6.16: Kinematic acceptance maps as a function of J/ψ transverse momentum and rapidity for specific spin-alignment scenarios considered, which are representative of the extrema of the variation of the measured cross-section due to spin-alignment configurations.

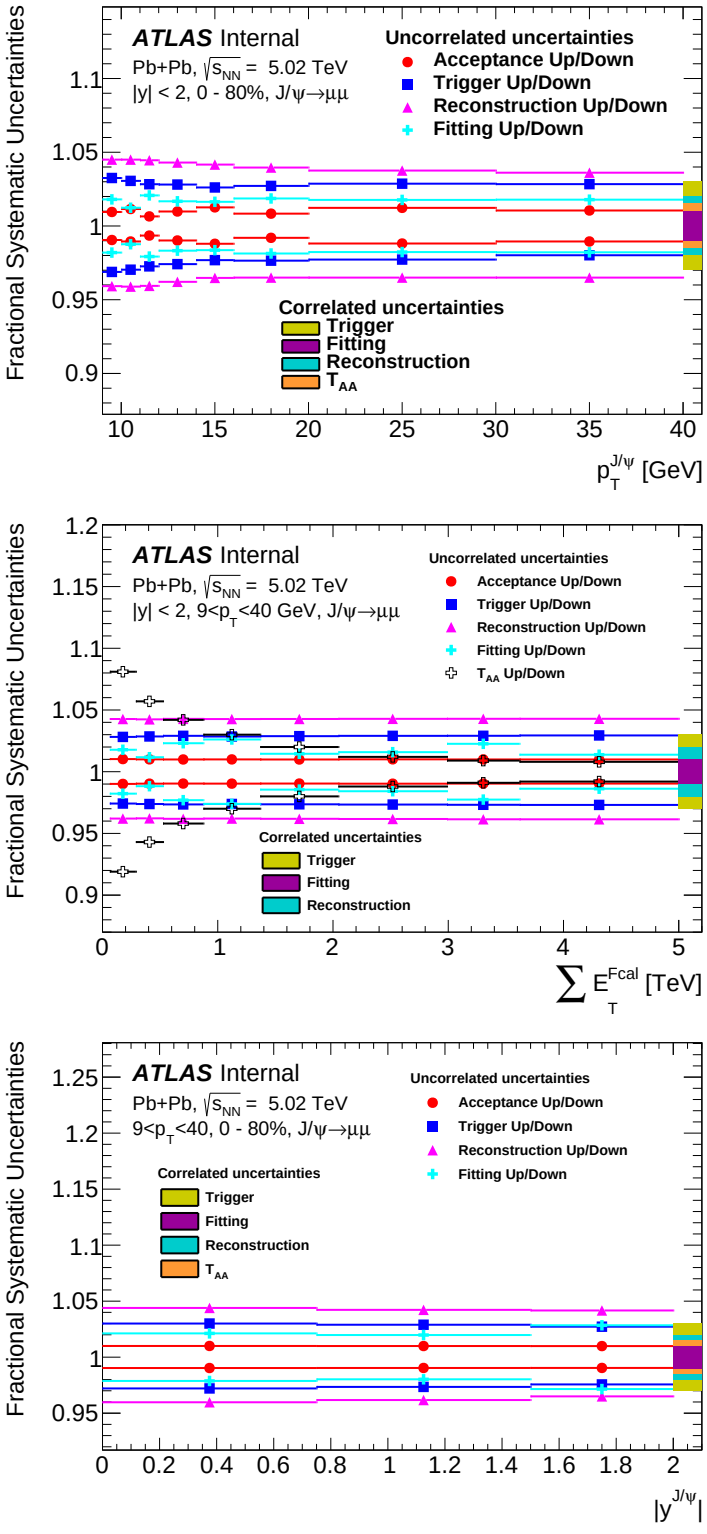

FIGURE 6.17: Summary of the different sources of systematic uncertainty in the Pb+Pb yields as a function of p_{T} (top), as a function of rapidity (middle) and as a function of $\sum E_{\mathrm{T}}^{\mathrm{Fcal}}$ (bottom). Local sources are shown with point to point symbols, global sources are presented with solid bands.

Chapter 7

Results

7.0.1 Prompt and non-prompt J/ψ and $\psi(2S)$ cross section in pp collisions

The results for the measurement of the cross section of prompt and non-prompt charmonium states in pp collisions are shown in this section.

In Figure 7.1 and Figure 7.2, the cross section as a function of p_{T} for production of prompt and non-prompt J/ψ and $\psi(2\mathrm{S})$ mesons is shown for central, mid and forward rapidities out to 40 GeV. The data are shown in the solid and open circles while the shaded band indicates the result and uncertainties from the non-relativistic QCD model [62] (the model calculations are only for $|y| < 2.5$). As can be seen, the data are in very good agreement with the calculations of this model within the uncertainties.

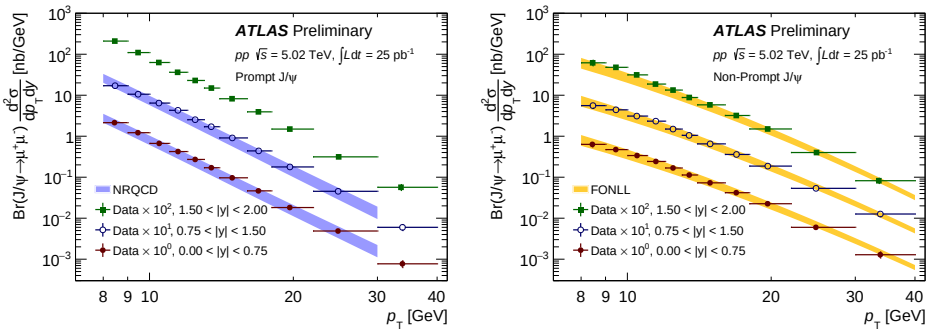

FIGURE 7.1: pp cross section of prompt J/ψ (left) and non-prompt J/ψ (right) production as a function of p_T for three $|y|$ slices, 1.50 < $|y|$ < 2.0 (top), 0.75 < $|y|$ < 1.50 (middle), 0.00 < $|y|$ < 0.75 (bottom). The vertical error bars are the combined systematic and statistical uncertainties, the are smaller than the plotted symbol for most of the points.

In Figure 7.3, the non-prompt fraction of J/ψ production is shown for central, mid, and forward rapidities. Figure 7.3 also shows the non-prompt fraction of J/ψ production for 13 TeV pp ATLAS data [13], together with 5.02 TeV pp ATLAS data, for central rapidities, $|y| < 0.75$. The figure also includes the non-prompt fraction measured by the CDF experiment [31] in $p\bar{p}$ collisions at $\sqrt{s}$ = 1.96 TeV for the rapidity interval of $|y| < 0.6$.

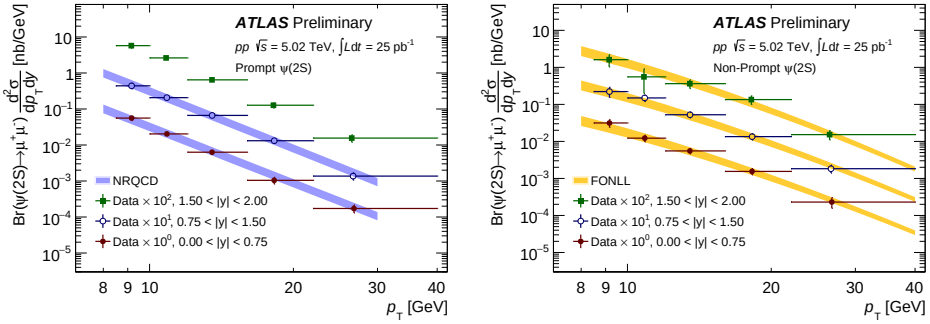

FIGURE 7.2: pp cross section of prompt $\psi(2S)$ (left) and non-prompt $\psi(2S)$ (right) production as a function of p_T for three $|y|$ slices, 1.50 < $|y|$ < 2.0 (top), 0.75 < $|y|$ < 1.50 (middle), 0.00 < $|y|$ < 0.75 (bottom). The vertical error bars are the combined systematic and statistical uncertainties

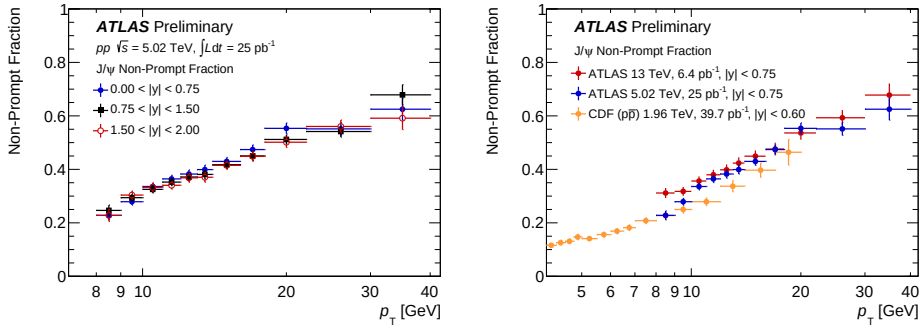

FIGURE 7.3: Non-prompt fraction of J/ψ production in 5.02 TeV pp collision data for different rapidity regions (left) and a comparison with the ATLAS 13 TeV pp collisions data and CDF $p\bar{p}$ collision data at 1.96 TeV at lower dimuon transverse momentum (right). The vertical error bars are the combined systematic and statistical uncertainties.

7.0.2 Prompt and non-prompt J/ψ per-event yields for Pb+Pb collisions

The per-event yields are defined as the number of J/ψ produced per bin of p_{T}, y and centrality intervals normalised by the width of the p_{T} and y bin and the number of events measured in minimum bias data for each centrality class, N_{evt}, as defined in Eq. 6.4. The resulting per-event yields and non-prompt fraction for J/ψ production are shown in Figures 7.4 and 7.5 respectively, as a function of transverse momentum, for three centrality slices and rapidity range $|y| < 2$. The vertical error bars in the J/ψ per-event yields shown in Figure 7.4 are the combined systematic and statistical uncertainties. The non-prompt fraction appears to be essentially centrality-independent and to have a slightly different slope from that found in pp collisions [15].

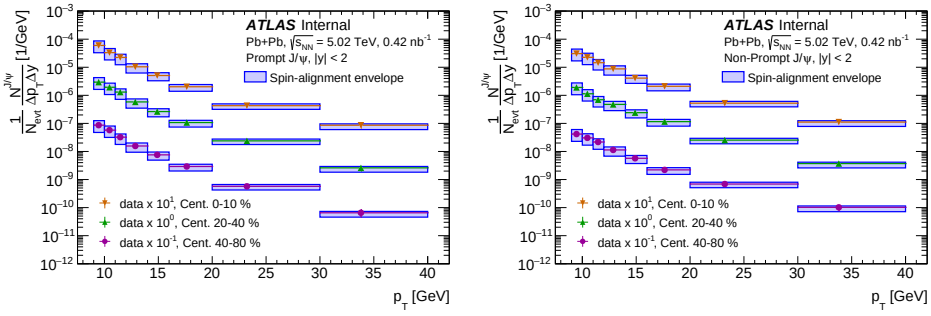

FIGURE 7.4: Pb+Pb per-event yields of prompt J/ψ (left) and non-prompt J/ψ (right) as a function of p_{T} for three different centrality slices in the rapidity range $|y| < 2$. The centroids of the p_{T} bins are the mean value of the transverse momentum distributions corrected for acceptance $\times$ efficiency. The vertical error bars are the combined systematic and statistical uncertainties.

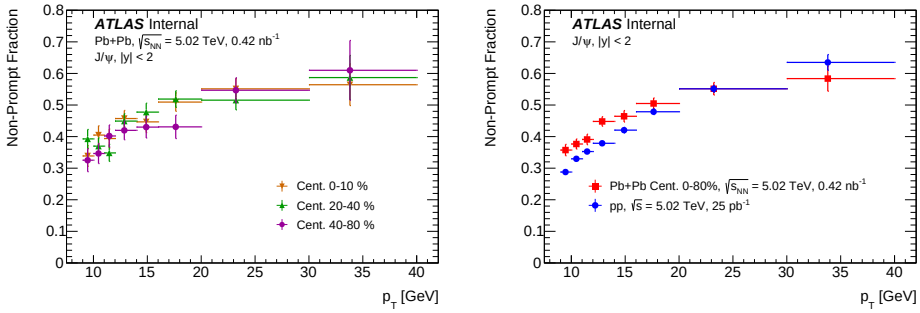

FIGURE 7.5: (Left) Non-prompt fraction of J/ψ production in 5.02 TeV Pb+Pb collision data as a function of p_{T} for three different centrality slices in the rapidity range $|y| < 2$. (Right) Comparison with the ATLAS 5.02 TeV pp collisions data [15]. The vertical error bars are the combined systematic and statistical uncertainties, dominated by the statistical uncertainty.

7.0.3 Nuclear modification factor, $R_{\mathrm{AA}}^{J/\psi}$

As discussed earlier, the influence of the hot dense medium on the production of the J/ψ mesons is quantified by the nuclear modification factor, given in Eq. 6.6, which compares production of charmonium in Pb+Pb collisions to the same process in pp collisions, taking geometric factors into account. The results from the measurement of this observable are presented as a function of transverse momentum in Figure 7.6, rapidity in Figure 7.9, and centrality in Figure 7.10; the last being presented as the mean number of participants. The error box at y-axis = 1 indicates the correlated systematic uncertainties of the measurement, while the error boxes associated with data-points represent the uncorrelated systematic uncertainties, and the error bars indicate the statistical uncertainties. The results exhibit an agreement with previous measurement performed by CMS at $\sqrt{s_{\mathrm{NN}}} = 2.76$ TeV in a similar kinematic region [35].

Figure 7.6 shows the nuclear modification factor as a function of p_{T} for production of prompt and non-prompt J/ψ, for $|y| < 2.0$, and for four selections of centrality. In this figure, it can be seen that the production of J/ψ is strongly suppressed in central Pb+Pb collisions. In the kinematic range plotted, as a function of p_{T}, the nuclear modification factor for both prompt and non-prompt J/ψ production is seen to be in the range $0.2 < R_{\mathrm{AA}} < 1$, depending on the centrality slice, having the minimum value for prompt J/ψ of 0.229 $\pm$ 0.017(stat) $\pm$ 0.016(syst) and 0.290 $\pm$ 0.034(stat) $\pm$ 0.021(syst) for the non-prompt. For p_{T} over 12 GeV, a small increase in R_{AA} with increasing p_{T} is observed for the first time in the prompt J/ψ production, as shown in Figure 7.7 (right), similar in shape and magnitude to what is observed for charged particles and D-mesons [17, 5], typically attributed to parton energy loss processes and for the case of charmonia, also to coherent radiation from the pre-resonant $q\bar{q}$ pair [65, 10]. In Figure 7.7 (left), one can see the prompt J/ψ R_{AA} evaluated for 0-20% centrality bin compared with several models, showing that the data is also consistent with the colour screening picture [47, 11]. The non-prompt J/ψ are seen to be approximately constant in p_{T} within the uncertainties, also consistent with parton energy loss mechanism [68]. As shown in figure 7.8, we also observe a good consistency between ATLAS and ALICE results.

In Figure 7.9, the nuclear modification factor is presented as a function of rapidity for production of prompt and non-prompt J/ψ for transverse momentum $9 < p_{\mathrm{T}} < 40$ GeV and for four selections of centrality. It can be seen from the figure that the R_{AA} exhibits a modest dependence on rapidity, expected as shown in Ref. [32]. These patterns are seen to be similar for both prompt and non-prompt J/ψ production.

Figure 7.10 presents the nuclear modification factor as a function of centrality, expressed as the number of participants, N_{part}, for production of prompt and non-prompt J/ψ for $|y| < 2.0$, and for $9 < p_{\mathrm{T}} < 40$ GeV. In the kinematic range plotted, as a function of centrality, the nuclear modification factor for both prompt and non-prompt decrease from the most peripheral bin, 60-80%, up to the most central, 0-5%, with a smallest value of 0.217 $\pm$ 0.010(stat) $\pm$ 0.020(syst) for prompt and 0.264 $\pm$ 0.017(stat) $\pm$ 0.023(syst) for non-prompt. Suppression by a factor of five for both prompt and non-prompt J/ψ mesons in central collisions is a very striking signature of a strong influence of the hot dense medium on the particle production processes. While the production of prompt J/ψ mesons is found to be suppressed slightly more in the mid-centrality region, the two classes of meson production have essentially the same pattern. This is not expected, because the two classes are believed to have quite different physical origins: the non-prompt production should be dominated by b-quark processes that extend far outside the deconfined medium, whereas the prompt production happens predominantly within the medium. This may be an indication that the prompt J/ψ suppression is also influenced by the energy loss mechanism as suggested in Ref. [65].

7.0.4 $\psi(2\mathrm{S})$ to J/ψ yield double ratio

A last observable discussed in this paper is the double ratio of $\psi(2\mathrm{S})$ production to J/ψ meson production, $\rho_{\mathrm{PbPb}}^{\psi(2S)/J/\psi}$, which is shown in Figure 7.11.

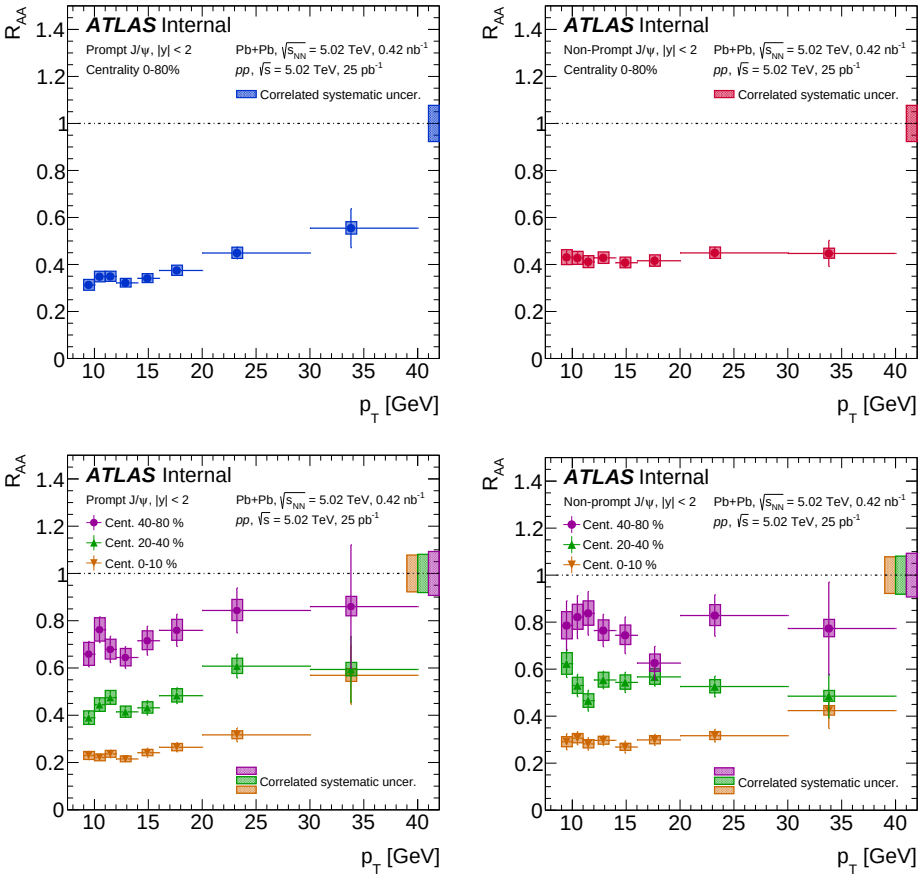

FIGURE 7.6: The nuclear modification factor as a function of p_{T} for the prompt J/ψ (left) and non-prompt J/ψ (right) for $|y| < 2$, in 0-80% centrality bin (top) and in 0-10%, 20-40%, and 40-80% centrality bins (bottom). The statistical uncertainty on each point is indicated by a narrow error bar. The error box plotted with each point represents the uncorrelated systematic uncertainty, while the shaded error box at y-axis=1 represents correlated scale uncertainties.

The results presented in this section represent a complementary measurement to an earlier measurement of $\psi(2S)$ to J/ψ yield ratios at the same center-of-mass energy done by CMS Collaboration [34]. This ratio, which compares the suppression of the two mesons, can be interpreted in models in which the binding energy of the two mesons is estimated, or in which the formation mechanisms differ. In the simplest interpretation, it can also offer an important cross-check: if the non-prompt J/ψ and $\psi(2\mathrm{S})$ originate from b-quarks losing energy in medium and hadronising outside of the medium, then the ratio of their yields should be unity. This statement should be true for the ratio expressed as a function of any kinematic variable. By contrast, prompt J/ψ and $\psi(2\mathrm{S})$ should traverse the hot and dense medium. Considering both mesons as composite systems, with potentially different formation mechanisms and different binding energies, they may respond differently to the hot dense medium. This interpretation is supported by the results of Figure 7.11, which shows the ratio of $\psi(2\mathrm{S})$ to J/ψ production as a function of the number of collision participants, N_{part}. The ratio is

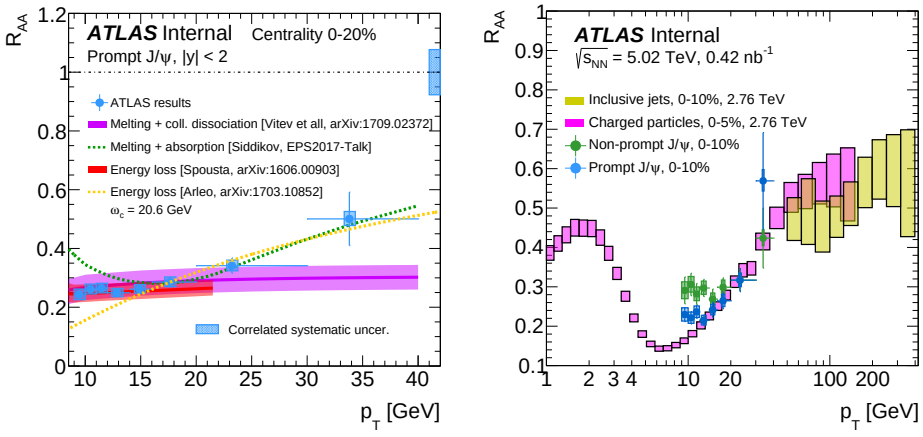

FIGURE 7.7: (Left) Comparison of the R_{AA} for prompt J/ψ production with different theoretical models. (Right) Comparison of prompt and non-prompt J/ψ R_{AA} with the R_{AA} of inclusive jets and charged particles. The statistical uncertainty on each point is indicated by a narrow error bar. The error box plotted with each point represents the uncorrelated systematic uncertainty, while the shaded error box at y-axis=1 represents correlated scale uncertainties.

consistent with unity within the experimental uncertainties for non-prompt mesons, while for prompt J/ψ the ratio is different from unity. These data support the enhanced suppression of prompt $\psi(2\mathrm{S})$ relative to J/ψ. This observation is consistent with the interpretation that the tightest bound quarkonium system, the J/ψ, survives the temperature of the hot and dense medium with a higher probability than the more loosely bound state, the $\psi(2\mathrm{S})$. It is however also consistent with the radiative energy loss scenario as shown in Ref. [65]. Irrespective of the underlying mechanism for the charmonium suppression, one may expect less ambiguity in the interpretation of these results since quark recombination processes, J/ψ's formed from uncorrelated $c\bar{c}$ pairs in the plasma, which are important at small $p_{\mathrm{T}}^{\psi(\mathrm{nS})}$, should not play a significant role here [66, 27, 3]. At the same time, the possible enhancement of $\psi(2S)$ yields seen for N_{part} above 300 in the $\rho_{\mathrm{PbPb}}^{\psi(2S)/J/\psi}$ distribution might be an indication of a sequential regeneration of charmonia in the most central collisions [40, 39].

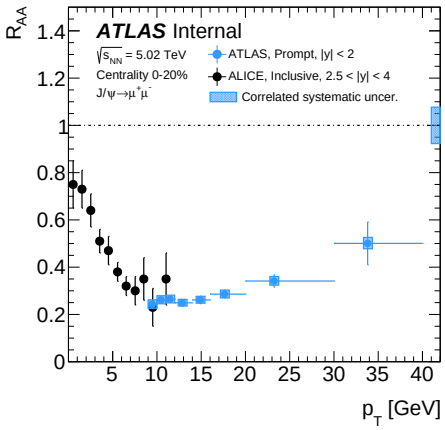

FIGURE 7.8: Comparisons with ALICE inclusive J/ψ R_{AA} at 5.02 TeV.

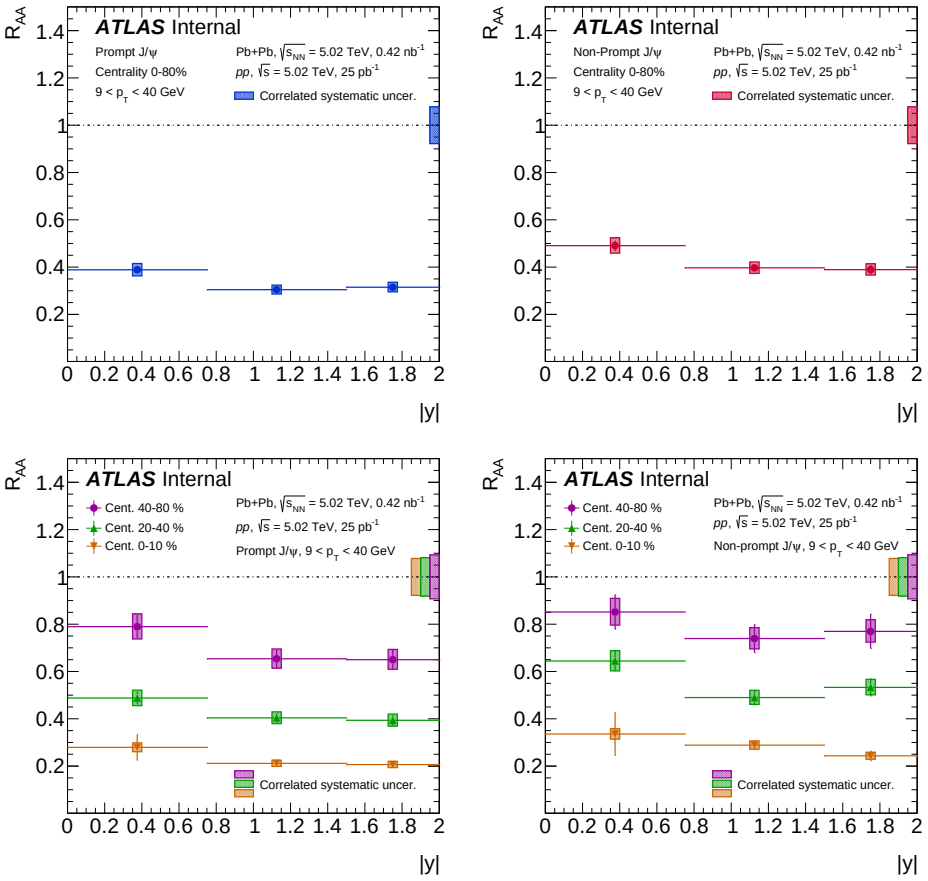

FIGURE 7.9: The nuclear modification factor as a function of rapidity for the prompt J/ψ (left) and non-prompt J/ψ (right) for $9 < p_{\mathrm{T}} < 40$ GeV, in 0-80% centrality bin (top) and in 0-10%, 20-40%, and 40-80% centrality bins (bottom). The statistical uncertainty on each point is indicated by a narrow error bar. The error box plotted with each point represents the uncorrelated systematic uncertainty, while the shaded error box at y-axis=1 represents correlated scale uncertainties.

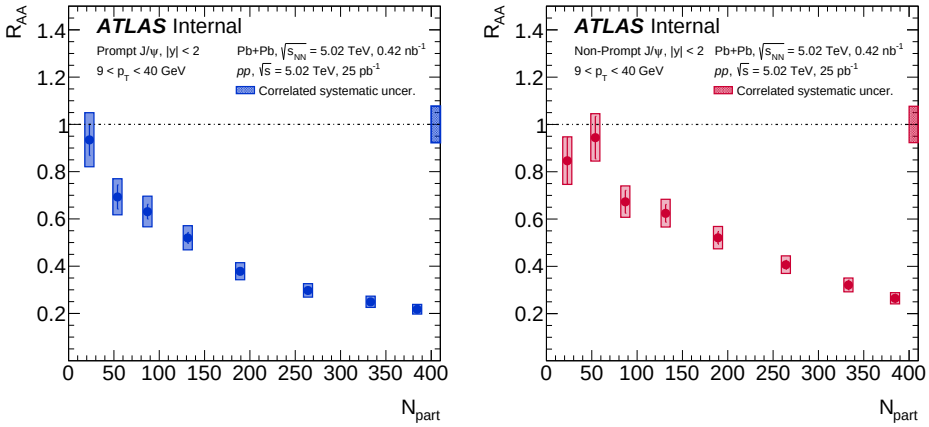

FIGURE 7.10: The nuclear modification factor as a function of number of participants, N_{part}, for the prompt J/ψ (left) and non-prompt J/ψ (right) for $9 < p_{\mathrm{T}} < 40$ GeV and for rapidity $|y| < 2$. The statistical uncertainty on each point is indicated by a narrow error bar. The error box plotted with each point represents the uncorrelated systematic uncertainty, while the shaded error box at y-axis=1 represents correlated scale uncertainties.

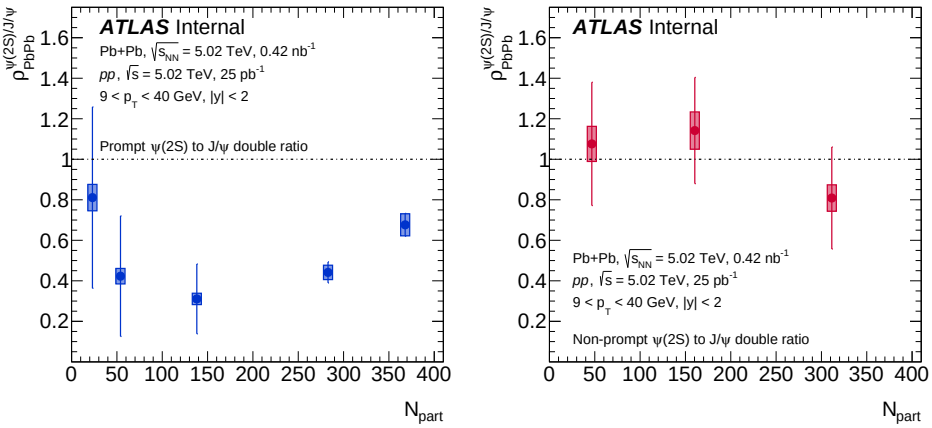

FIGURE 7.11: $\psi(2\mathrm{S})$ to J/ψ double ratio, as a function of number of participants, N_{part}, for prompt meson production (left) and non-prompt meson production (right). The narrow error bar represents the statistical uncertainties while the error box represents the total systematic uncertainty.

Chapter 8

Conclusion

ATLAS measurements are presented of prompt and non-prompt differential production cross sections and nuclear modification factors, R_{AA}, of the J/ψ and $\psi(2\mathrm{S})$ mesons. The measurements are performed in the dimuon decay channel in Pb+Pb collisions at $\sqrt{s_{\mathrm{NN}}}$ = 5.02 TeV, with an integrated luminosity of $0.49\ \mathrm{nb}^{-1}$, and in pp collisions at $\sqrt{s}$ = 5.02 TeV, with an integrated luminosity of $25\ \mathrm{pb}^{-1}$. The measurements are presented for $9 < p_{\mathrm{T}} < 40$ GeV in transverse momentum, and $|y| < 2.0$ in rapidity.

A strong suppression of both prompt and non-prompt J/ψ and $\psi(2\mathrm{S})$ mesons is observed. The maximal suppression of both prompt and non-prompt J/ψ is observed for the most central events. The distribution of the dependence of the nuclear modification factor R_{AA} on centrality is approximately the same for both prompt and non-prompt J/ψ. The similarity of this shape for both prompt and non-prompt J/ψ is striking since in the simplest interpretation the observed prompt mesons come predominantly from potentially fragile composite systems exposed to the hot dense medium while the non-prompt mesons come predominantly from b-quarks traversing through the medium; thus, one might expect different trends as a function of centrality. As shown in Figure 8.1 the suppression observed in Pb+Pb collisions can be totally attribute to Quark-Gluon-Plasma effects, discarding suppression due to cold matter effects. The ratio of $\psi(2\mathrm{S})$ to J/ψ

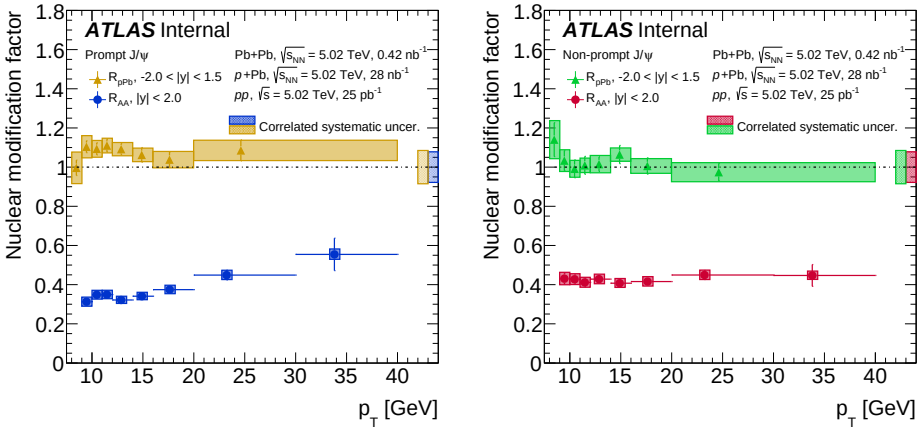

FIGURE 8.1: Comparison of the nuclear modification factor in Pb+Pb and p+Pb collisions as a function of p_{T} for the prompt J/ψ (left) and non-prompt J/ψ (right). The error box plotted with each point represents the uncorrelated systematic uncertainty, while the shaded error box at y-axis=1 represents correlated scale uncertainties.

meson production is measured for both prompt and non-prompt mesons, and shown as a function of centrality. Values consistent with unity are measured for the non-prompt mesons, while the values observed for the prompt mesons are below unity. This result is consistent with what would be expected for *b*-quarks in the hot dense medium with the same behaviour for both mesons, while composite mesons formed in the hot dense medium are affected differently. In particular, the $\psi(2\mathrm{S})$ meson is suppressed more than the J/ψ meson, a pattern consistent with the lower binding energy of the $\psi(2\mathrm{S})$ meson causing it to have a lower formation and survival probability in the hot dense medium for the values of $p_{\mathrm{T}}^{\psi(\mathrm{nS})}$ sampled in this measurement.

Appendix A

Datasets

xAOD samples used to measure the detector performance are listed in the table A.1. DAOD samples reconstructed with the derivation HION3 are listed in table A.2.

HION3 algorithm summary

- Augmentation:
  - JpsiFinder: vertex reffiting tool, secondary vertex reconstruction.
  - Reco_mumu: Add output vertex collection and add decoration which do not depend on the vertex mass hypo (p_T error, L_{xy} ...).
  - Select_onia2mumu: decorate the vertices with variables that depend on the vertex mass hypo (inv Mass, tau).
- Skimming (event selection) in AND logic:
  - At least one (J/ψ || $\psi(2S)$ || $\Upsilon(nS)$) candidate must been found.
  - Triggers Selection: L1_MU4 || L1_MU6 || HLT_mu4 || HLT_mu6 || HLT_mu4_mu2noL1 || HLT_mu4_mu4noL1 || HLT_mu6_mu4noL1 || HLT_2mu4.
  - At least one reconstructed vertex.
- Thinning in OR logic:
  - Keep only track and vertices related to (J/ψ || $\psi(2S)$ || $\Upsilon(nS)$).
  - Keep only track related to Muons.
  - TrigNavigation save only L1_MU* & L1_2MU* & HLT_mu* & HLT_2mu*
- Slimming:
  - Muon Container.
  - Tracks: InDetTrackParticles, CombinedMuonTracksParticles, ExtrapolatedMuonTrackParticles.
  - HI related: CaloSums, ZDCModules, HIEventShape.
  - HION3Candidates.
  - Muon Trigger info.
- if MC:
  - TruthEvent, TruthParticles, TruthVertices, MuonTruthParticles.

xAOD sample
data15_hi.00287334.physics_HardProbes.merge.AOD.r7874_p2580
data15_hi.00287560.physics_HardProbes.merge.AOD.r7874_p2580
data15_hi.00287270.physics_HardProbes.merge.AOD.r7874_p2580
data15_hi.00287931.physics_HardProbes.merge.AOD.r7874_p2580
data15_hi.00287728.physics_HardProbes.merge.AOD.r7874_p2580
data15_hi.00287594.physics_HardProbes.merge.AOD.r7874_p2580
data15_hi.00287380.physics_HardProbes.merge.AOD.r7874_p2580
data15_hi.00287866.physics_HardProbes.merge.AOD.r7874_p2580
data15_hi.00287038.physics_HardProbes.merge.AOD.r7874_p2580
data15_hi.00286967.physics_HardProbes.merge.AOD.r7874_p2580
data15_hi.00287259.physics_HardProbes.merge.AOD.r7874_p2580
data15_hi.00286711.physics_HardProbes.merge.AOD.r7874_p2580
data15_hi.00286748.physics_HardProbes.merge.AOD.r7874_p2580
data15_hi.00287378.physics_HardProbes.merge.AOD.r7874_p2580
data15_hi.00287224.physics_HardProbes.merge.AOD.r7874_p2580
data15_hi.00287843.physics_HardProbes.merge.AOD.r7874_p2580
data15_hi.00286834.physics_HardProbes.merge.AOD.r7874_p2580
data15_hi.00287382.physics_HardProbes.merge.AOD.r7874_p2580
data15_hi.00286854.physics_HardProbes.merge.AOD.r7874_p2580
data15_hi.00287632.physics_HardProbes.merge.AOD.r7874_p2580
data15_hi.00286717.physics_HardProbes.merge.AOD.r7874_p2580
data15_hi.00286995.physics_HardProbes.merge.AOD.r7874_p2580
data15_hi.00287330.physics_HardProbes.merge.AOD.r7874_p2580
data15_hi.00287222.physics_HardProbes.merge.AOD.r7874_p2580
data15_hi.00286908.physics_HardProbes.merge.AOD.r7874_p2580
data15_hi.00287827.physics_HardProbes.merge.AOD.r7874_p2580
data15_hi.00287924.physics_HardProbes.merge.AOD.r7874_p2580
data15_hi.00286767.physics_HardProbes.merge.AOD.r7874_p2580
data15_hi.00287706.physics_HardProbes.merge.AOD.r7874_p2580
data15_hi.00287044.physics_HardProbes.merge.AOD.r7874_p2580
data15_hi.00286990.physics_HardProbes.merge.AOD.r7874_p2580
data15_hi.00287068.physics_HardProbes.merge.AOD.r7874_p2580
data15_hi.00287321.physics_HardProbes.merge.AOD.r7874_p2580
data15_hi.00287281.physics_HardProbes.merge.AOD.r7874_p2580

TABLE A.1: HardProbes (xAOD) stream data samples used to measure the detector performance.

HION3 derivation samples
data15_hi.00287866.physics_HardProbes.merge.DAOD_HION3.r7874_p2580_p2709
data15_hi.00287259.physics_HardProbes.merge.DAOD_HION3.r7874_p2580_p2709
data15_hi.00287068.physics_HardProbes.merge.DAOD_HION3.r7874_p2580_p2709
data15_hi.00287728.physics_HardProbes.merge.DAOD_HION3.r7874_p2580_p2709
data15_hi.00287382.physics_HardProbes.merge.DAOD_HION3.r7874_p2580_p2709
data15_hi.00286967.physics_HardProbes.merge.DAOD_HION3.r7874_p2580_p2709
data15_hi.00287924.physics_HardProbes.merge.DAOD_HION3.r7874_p2580_p2709
data15_hi.00287334.physics_HardProbes.merge.DAOD_HION3.r7874_p2580_p2709
data15_hi.00286748.physics_HardProbes.merge.DAOD_HION3.r7874_p2580_p2709
data15_hi.00287038.physics_HardProbes.merge.DAOD_HION3.r7874_p2580_p2709
data15_hi.00286995.physics_HardProbes.merge.DAOD_HION3.r7874_p2580_p2709
data15_hi.00286767.physics_HardProbes.merge.DAOD_HION3.r7874_p2580_p2709
data15_hi.00287330.physics_HardProbes.merge.DAOD_HION3.r7874_p2580_p2709
data15_hi.00286854.physics_HardProbes.merge.DAOD_HION3.r7874_p2580_p2709
data15_hi.00287222.physics_HardProbes.merge.DAOD_HION3.r7874_p2580_p2709
data15_hi.00286908.physics_HardProbes.merge.DAOD_HION3.r7874_p2580_p2709
data15_hi.00287270.physics_HardProbes.merge.DAOD_HION3.r7874_p2580_p2709
data15_hi.00286711.physics_HardProbes.merge.DAOD_HION3.r7874_p2580_p2709
data15_hi.00287321.physics_HardProbes.merge.DAOD_HION3.r7874_p2580_p2709
data15_hi.00287560.physics_HardProbes.merge.DAOD_HION3.r7874_p2580_p2709
data15_hi.00286834.physics_HardProbes.merge.DAOD_HION3.r7874_p2580_p2709
data15_hi.00287931.physics_HardProbes.merge.DAOD_HION3.r7874_p2580_p2709
data15_hi.00287632.physics_HardProbes.merge.DAOD_HION3.r7874_p2580_p2709
data15_hi.00287224.physics_HardProbes.merge.DAOD_HION3.r7874_p2580_p2709
data15_hi.00286990.physics_HardProbes.merge.DAOD_HION3.r7874_p2580_p2709
data15_hi.00287594.physics_HardProbes.merge.DAOD_HION3.r7874_p2580_p2709
data15_hi.00286717.physics_HardProbes.merge.DAOD_HION3.r7874_p2580_p2709
data15_hi.00287843.physics_HardProbes.merge.DAOD_HION3.r7874_p2580_p2709
data15_hi.00287378.physics_HardProbes.merge.DAOD_HION3.r7874_p2580_p2709
data15_hi.00287827.physics_HardProbes.merge.DAOD_HION3.r7874_p2580_p2709
data15_hi.00287044.physics_HardProbes.merge.DAOD_HION3.r7874_p2580_p2709
data15_hi.00287380.physics_HardProbes.merge.DAOD_HION3.r7874_p2580_p2709
data15_hi.00287281.physics_HardProbes.merge.DAOD_HION3.r7874_p2580_p2709
data15_hi.00287706.physics_HardProbes.merge.DAOD_HION3.r7874_p2580_p2709

TABLE A.2: HardProbes (DAOD) stream data samples used to measure the detector performance.

Appendix B

MinBias event counting

The number of minimum-bias events is needed to normalised the production of any particle in the Pb+Pb collisions, like the integrated luminosity is the pp cross sections. Basically $N_{\text{evt}}^{\text{MB}}$ is equal to the total number of collisions.
In order to calculate this number we used the following event selection in the minimum-bias data sets listed in the table B.1:

- MinBias trigger (MBT) selection:
  - HLT_mb_sptrk_ion_L1ZDC_A_C_VTE50 | | HLT_noalg_mb_L1TE50
- At least 1 primary vertex
- pileup rejection
- GRL

Figure (B.1) show the distribution of the energy deposited in the fordward calorimeters, of the total number of events in the minbias stream, the one that passes the MBT and the pileup events. Pileup events correspond to the 1% of the events that passes the MBT. Once the selection is done, each event

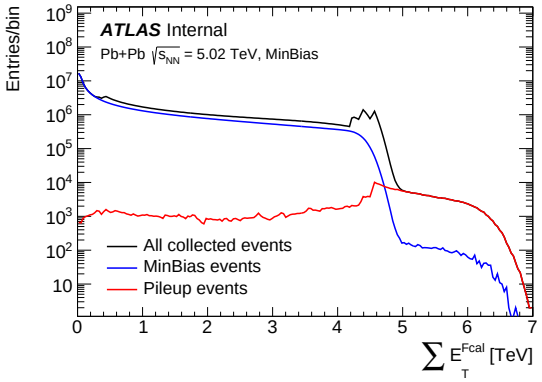

FIGURE B.1: figure shows the total number of events in the minbias stream in black, the one that passes the MBT in blue and the pileup events in red.

that passes the selection is weighted with the prescale of their respective trigger.
We found 37.4 million events by 1% centrality bin (Fig. (B.2)), considering total luminosity collected of 486 μb^{-1}, the number of events by luminosity is 37.4M*80/486 = 6.156.378. Consistent with run-by-run results, as shown in Fig. (B.2).

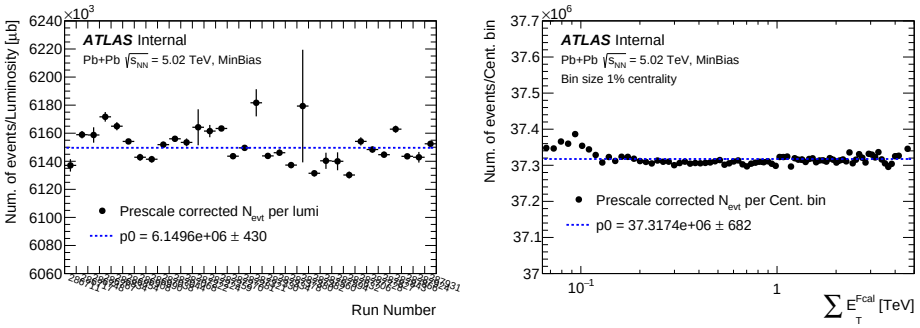

FIGURE B.2: Run-by-run stability of the number of events by luminosity (left) and number of events as a function of the sum of the energy deposited in the forward calorimeters in bins equivalents to 1% of centrality (right).

Name of the sample
data15_hi.00287270.physics_MinBias.merge.AOD.r7874_p2580
data15_hi.00287706.physics_MinBias.merge.AOD.r7874_p2580
data15_hi.00287281.physics_MinBias.merge.AOD.r7874_p2580
data15_hi.00287843.physics_MinBias.merge.AOD.r7874_p2580
data15_hi.00286967.physics_MinBias.merge.AOD.r7874_p2580
data15_hi.00286711.physics_MinBias.merge.AOD.r7874_p2580
data15_hi.00287728.physics_MinBias.merge.AOD.r7874_p2580
data15_hi.00287321.physics_MinBias.merge.AOD.r7874_p2580
data15_hi.00287866.physics_MinBias.merge.AOD.r7874_p2580
data15_hi.00286834.physics_MinBias.merge.AOD.r7874_p2580
data15_hi.00286665.physics_MinBias.merge.AOD.r7874_p2580
data15_hi.00287334.physics_MinBias.merge.AOD.r7874_p2580
data15_hi.00287594.physics_MinBias.merge.AOD.r7874_p2580
data15_hi.00287380.physics_MinBias.merge.AOD.r7874_p2580
data15_hi.00286748.physics_MinBias.merge.AOD.r7874_p2580
data15_hi.00287044.physics_MinBias.merge.AOD.r7874_p2580
data15_hi.00287931.physics_MinBias.merge.AOD.r7874_p2580
data15_hi.00287259.physics_MinBias.merge.AOD.r7874_p2580
data15_hi.00287038.physics_MinBias.merge.AOD.r7874_p2580
data15_hi.00287382.physics_MinBias.merge.AOD.r7874_p2580
data15_hi.00286990.physics_MinBias.merge.AOD.r7874_p2580
data15_hi.00286908.physics_MinBias.merge.AOD.r7874_p2580
data15_hi.00286767.physics_MinBias.merge.AOD.r7874_p2580
data15_hi.00286995.physics_MinBias.merge.AOD.r7874_p2580
data15_hi.00287330.physics_MinBias.merge.AOD.r7874_p2580
data15_hi.00286717.physics_MinBias.merge.AOD.r7874_p2580
data15_hi.00287632.physics_MinBias.merge.AOD.r7874_p2580
data15_hi.00287827.physics_MinBias.merge.AOD.r7874_p2580
data15_hi.00287068.physics_MinBias.merge.AOD.r7874_p2580
data15_hi.00287560.physics_MinBias.merge.AOD.r7874_p2580
data15_hi.00287224.physics_MinBias.merge.AOD.r7874_p2580
data15_hi.00286854.physics_MinBias.merge.AOD.r7874_p2580
data15_hi.00287378.physics_MinBias.merge.AOD.r7874_p2580
data15_hi.00287924.physics_MinBias.merge.AOD.r7874_p2580
data15_hi.00287222.physics_MinBias.merge.AOD.r7874_p2580

TABLE B.1: Minbias data samples used to calculate the total number of collisions.

Appendix C

Working Point

Heavy ions muon selection is defined as *tight* [20] without the the **TRT** requirement because this sub-detector do not perform well in high multiplicity environment of the typical heavy-ion collision. The study of the detector performance was done in MC using a sample of $pp \rightarrow J/\psi \rightarrow \mu\mu$ simulated with PYTHIA8B [64] and the same sample overlaid with a sample of data to emulate the high multiplicity density produce by the Pb+Pb collision.

pp@5.02TeV
mc15_5TeV.300000.Pythia8BPhotospp_A14_CTEQ6L1_pp_Jpsimu2p5mu2p5.merge.AOD.e4973_s2860_r7792_r7676
PbPb@5.02TeV (pp + data overlay)
mc15_5TeV.300000.Pythia8BPhotospp_A14_CTEQ6L1_pp_Jpsimu2p5mu2p5.merge.AOD.e4973_d1413_r8026_r7676

Figure C.1 shown the offline muon parameters p_T, η, and ϕ. We can see that the offline muons linked to truth in the overlay sample (signal), in red triangles, match very well to the pp simulation, solid purple. The muons coming from the data overlay sample are shown in green triangles. Figure C.2 show the comparison MS reconstruction parameters of MC data overlay signal muons and pp MC muons. We can see that there is a good agreements between the two samples. Figure C.3 show the comparison ID reconstruction parameters of MC data overlay signal muons and pp MC muons. As we can see in the plots at the bottom there is a huge tension between the distributions of TRT hits, and outliers in the data overlay, and pp standalone MC sample. We understand this as an issue with the pattern recognition in high multiplicities, basically the TRT saturated very quick in the central collision and the information provided by this sub-detector is not trustable. Figure C.4 show the comparison of quality reconstruction parameters in MC data overlay signal muons and pp MC muons. There is also some tension in the distribution of the χ^2/ndf but seen to be not important.

In order to quantified the impact of the TRT requirement in the selection of the PbPb data we extracted the ID selection efficiency, define as:

$$\epsilon_{ID} = \frac{\text{Muon that pass ID selection}}{\text{all muons}} \tag{C.1}$$

Results are shown in figure C.5, as we can see there are a 40% less muons that pass the selection in the overlay sample with respect to the standalone pp simulation. In figure C.6 we can see that the efficiency of the quality selection defined as:

$$\epsilon_{ID} = \frac{\text{tight without ID selection}}{\text{all muons}} \tag{C.2}$$

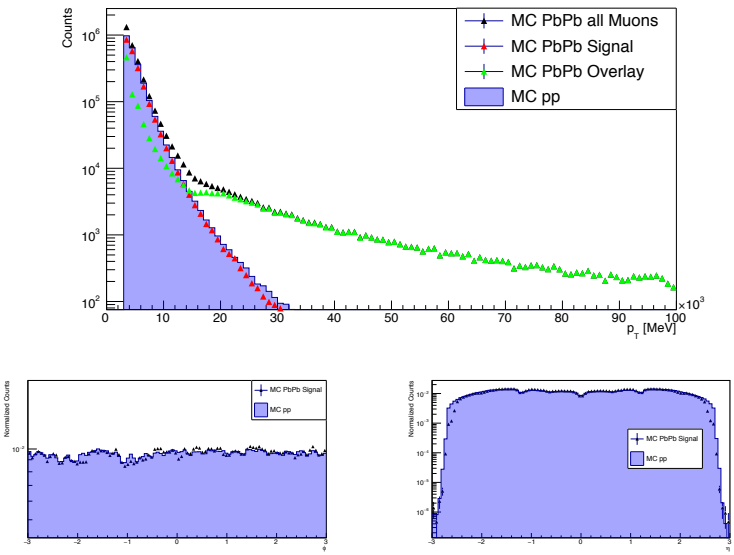

FIGURE C.1: Offline reconstruction muon distributions. (top) Muon p_T distribution of MC data overlay sample, full sample of muon are shown in black triangles, muons linked to truth in red, and muons from the overlay sample in green. (bottom, right) Muon ϕ distribution, (bottom, left) muon η distribution. The pp simulation is show in solid purple.

this efficiency show good agreement between the both samples, pointing that the issue is at the ID selection as expected.

To finalise we show the ID efficiency removing the TRT selection criteria, fig C.7, we can see that by removing this selection the efficiency is recovered, concluding that the TRT should not be used to select muon in the PbPb sample, as we pointed at the beginning.

In order to do the selection we used the *MuonSelectorTool* with the TRT selection turned off, using the option:

```
m_muonSelection->setProperty("TrtCutOff",true)
```

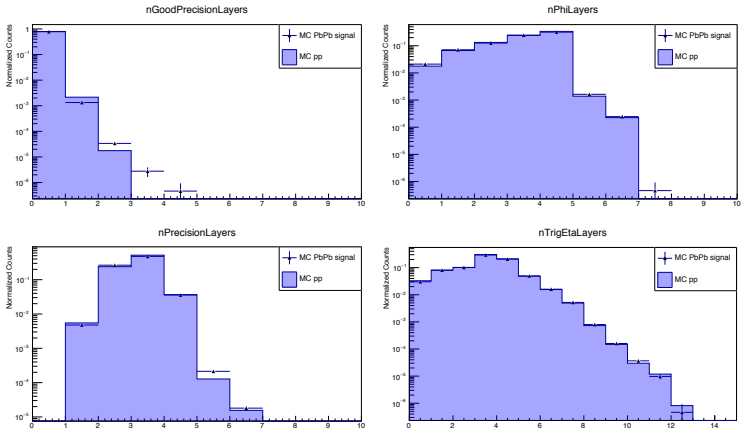

FIGURE C.2: Muon p_T distribution of MC data overlay sample

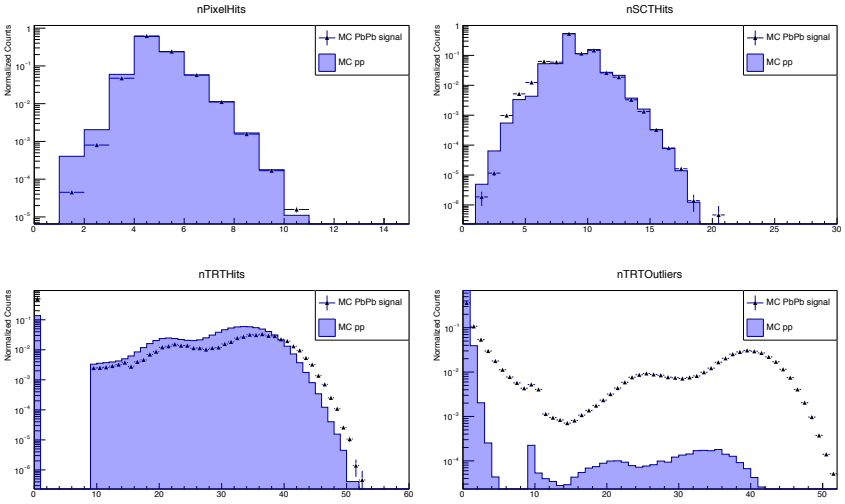

FIGURE C.3: Muon p_T distribution of MC data overlay sample

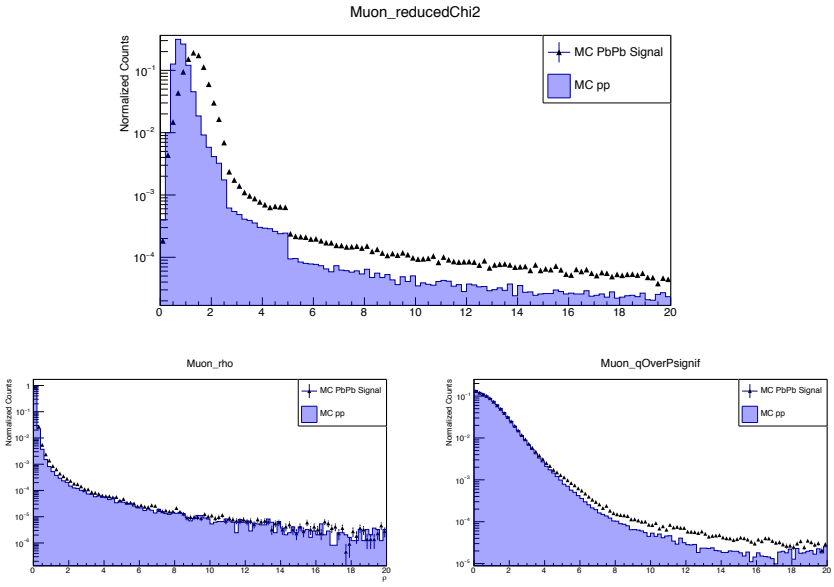

FIGURE C.4: Muon p_T distribution of MC data overlay sample

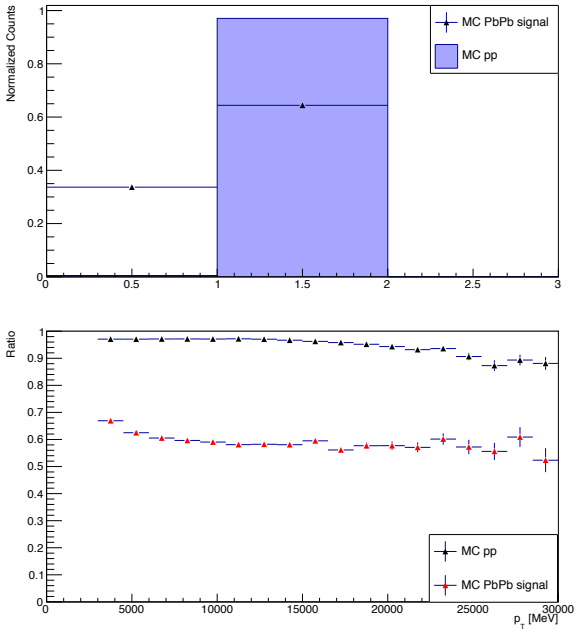

FIGURE C.5: ID selection efficiency, for the integrate sample in the top and as a function of the muon p_T at bottom.

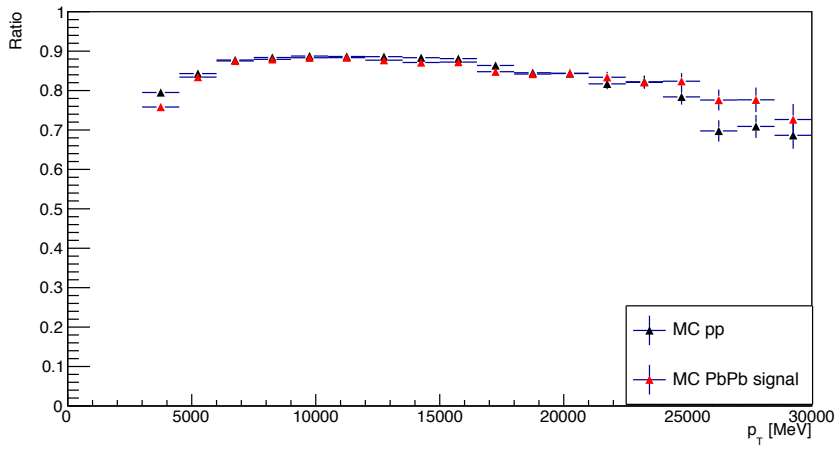

FIGURE C.6: Quality selection efficiency, as a function of the muon p_T.

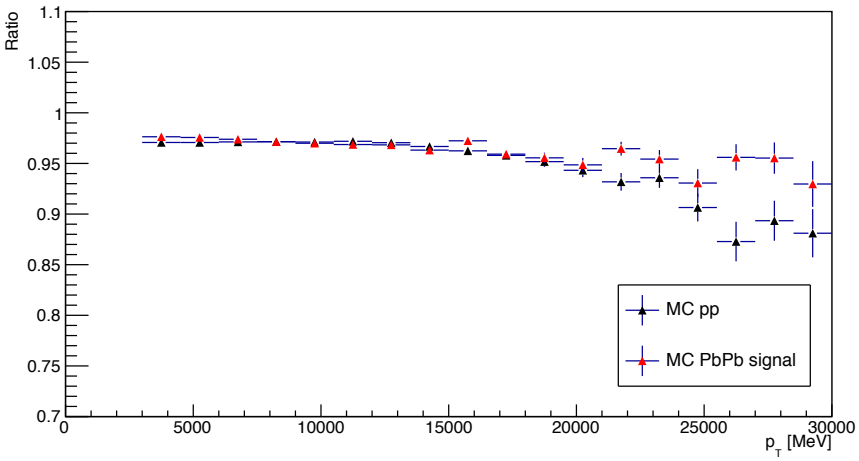

FIGURE C.7: ID selection efficiency without TRT, as a function of the muon p_T.

Appendix D

Trigger efficiency: centrality dependence

As is shown in figure 5.17 a small dependence in the trigger efficiency is observed as a function of the centrality in data and MC. To cross-check that this is not induce by the different distributions of the $\sum E_T^{\text{FCal}}$ in data and MC (see figure D.1) we reweigh the efficiency observed in MC with the E_T distribution of the data, in order to get a better description of the efficiency in MC. Results is shown in figure D.2, and not strong difference is observed between weighed and no weighed efficiency.
As the dependence as a function of the centrality seems to be real, we broken down the HLT_mu4 efficiency in their different steps in order to determine which is the algorithm that is inefficient. Looking at the results in figure D.3 and D.4, we can see that the inefficiency is coming from the EF. In the case of the HLT_mu4 this step is composed by two algorithm:

EF_EFIDInsideOut_mu4_MU4
TrigMuSuperEF / TrigMuSuperEF
TrigMuonEFCombinerHypo / TrigMuonEFCombinerHypo_Muon_4GeV

Further studies are required to determined what is the problem with the algorithm and how to fix it, the last check we made was the p_T dependence of the EF efficiency. We can see in figure D.5 that the efficiency, $\epsilon_{mu}(EF|CB)$, don't show a strong dependence to the transverse momentum of the probe.

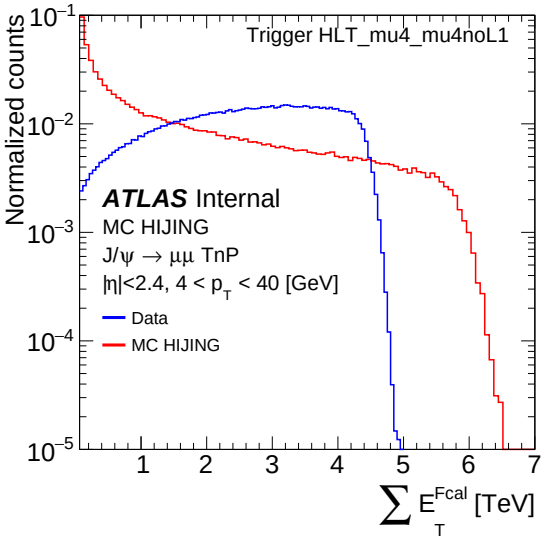

FIGURE D.1: $\sum E_T^{\mathrm{FCal}}$ distribution in data and MC

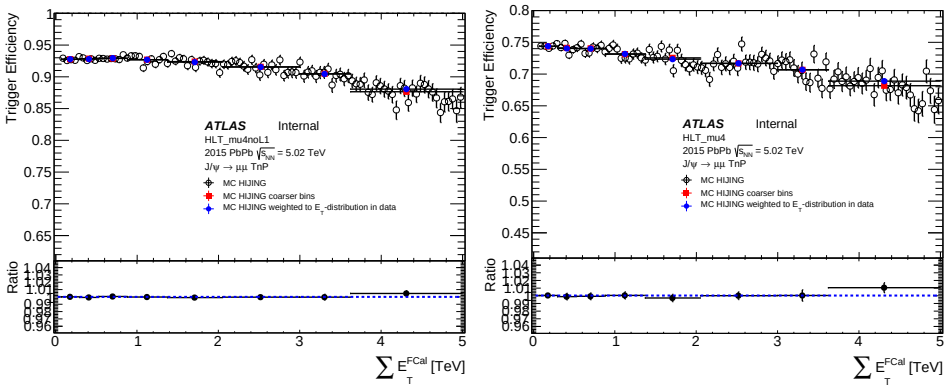

FIGURE D.2: Comparisons of TnP MC efficiency as a function of centrality for fine bins, coarser bins, and weighted to the E_T-distribution observed in data. (left) HLT_mu4noL1 and (right) HLT_mu4

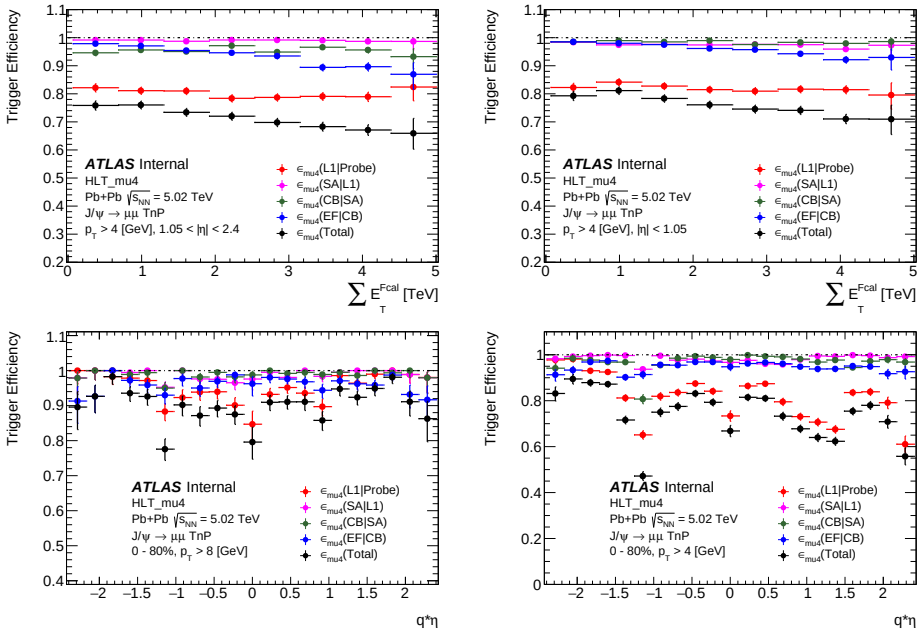

FIGURE D.3: HLT_mu4 efficiency breakdown, as a function of centrality (top) and η (bottom).

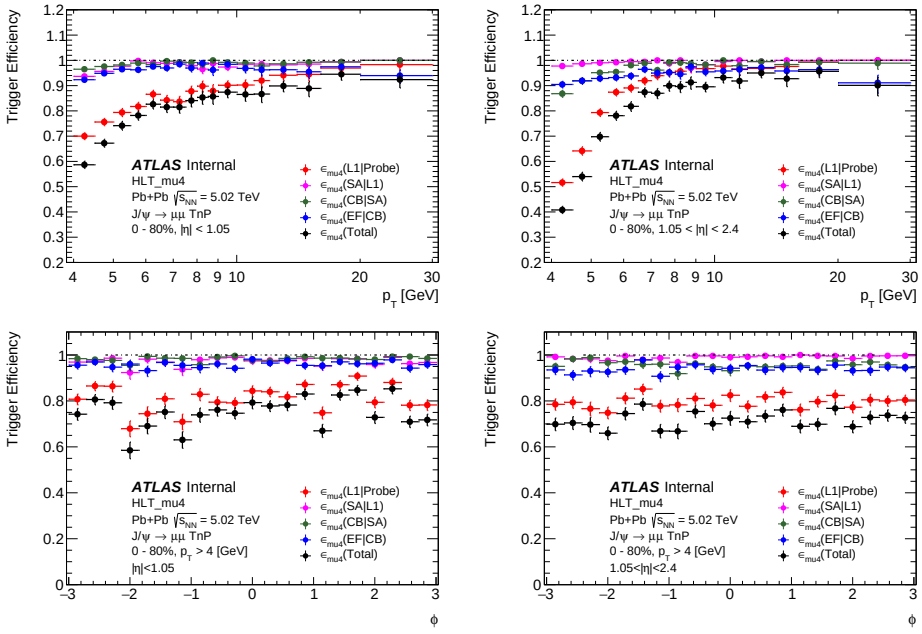

FIGURE D.4: HLT_mu4 efficiency breakdown, as a function of p_T (top) and ϕ (bottom).

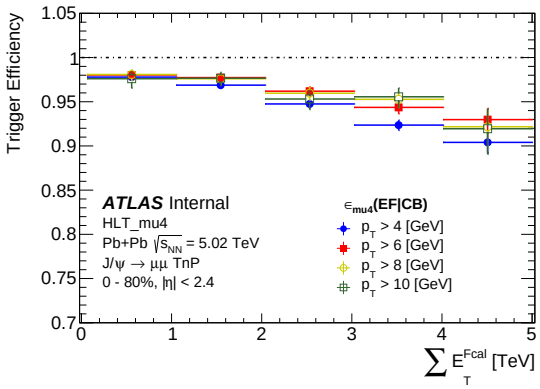

FIGURE D.5: $\epsilon_{mu}(EF|CB)$ as a function of the $\sum E_T^{FCal}$ for different p_T slices.

Appendix E

Asymmetry of systematic uncertainties

Asymmetry of the systematic comes explicitly from the procedure that we use to propagate them.
Each weight is defined as:

$$w = \frac{1}{\epsilon} \tag{E.1}$$

having a total weight equal to:

$$w_{\text{total}} = \frac{1}{\epsilon_{\text{trig}} \cdot \epsilon_{\text{reco}} \cdot Acc} \tag{E.2}$$

where ϵ_{trig} and ϵ_{reco} are the trigger and reconstruction efficiencies and Acc the detector kinematic acceptance.
In order to propagate the systematic uncertainty of each term, the efficiency is varied according to the value of the respective uncertainty, up and down, and producing new weights. as follows:

$$w_{\uparrow} = \frac{1}{\epsilon + \nu} \tag{E.3}$$

$$w_{\downarrow} = \frac{1}{\epsilon - \nu} \tag{E.4}$$

where ν is the systematic variation of the efficiency.
Then, the value of the systematic uncertainty is calculated as:

$$\text{Syst.} \uparrow\downarrow [\%] = \frac{|N(w_0) - N(w_{\uparrow\downarrow})|}{N(w_0)} \tag{E.5}$$

where, w_0 is the nominal weight and $w_{\uparrow\downarrow}$ are the positive and negative systematic variation.
From here the reason of the asymmetry becomes clear, if we expand Eq.(E.3) and Eq.(E.4),

$$w_{\uparrow} = \frac{1}{\epsilon + \nu} = \frac{1}{\epsilon} \cdot \frac{1}{1 + \frac{\nu}{\epsilon}} = \frac{1}{\epsilon}(1 - \frac{\nu}{\epsilon} + (\frac{\nu}{\epsilon})^2 - (\frac{\nu}{\epsilon})^3 + \Theta[\frac{\nu}{\epsilon}]^4) \tag{E.6}$$

$$w_{\downarrow} = \frac{1}{\epsilon - \nu} = \frac{1}{\epsilon} \cdot \frac{1}{1 - \frac{\nu}{\epsilon}} = \frac{1}{\epsilon}(1 + \frac{\nu}{\epsilon} + (\frac{\nu}{\epsilon})^2 + (\frac{\nu}{\epsilon})^3 + \Theta[\frac{\nu}{\epsilon}]^4) \tag{E.7}$$

We can see the second-order term, $(\frac{\nu}{\epsilon})^2$, in the expansion will produce the asymmetry in the weight, and the uncertanty, when the term $\frac{\nu}{\epsilon}$ is not small enough to be neglected. This is the case of the reconstruction efficiency,

specially at low p_{T} as is shown if Figure 5.8.

Appendix F

Acceptance FSR validation

By final state radiation (FSR) we mean the electromagnetic radiation of the muons, as shown in figure F.1 that is not reconstructed by the detector and therefore invisible.

As the correction is extracted from a simulation with a cut in the transverse momentum of the muons, $p_{\mathrm{T}} > 2.5\,\mathrm{GeV}$, is necessary to check that this cut in the phase-space is not biasing the result. in order to add the FSR to the toy MC we try several exponential distributions to emulate the p_{T} distribution of the emitted photon, in figure F.2 we can see the distribution for four different choice of the λ parameter. In figure F.3 we can see the acceptance as a function of the J/ψ p_{T} with and without the phase-space cut in the muon transverse momentum and applying our FSR emulation with two values for the exponential distribution parameter.
Looking at figure F.4, the ratio between the acceptance applying the FSR and the standard method, we can conclude that the correction depend on the distribution we used to emulate the p_{T} of the photon but is independent of the phase space cut we applied.

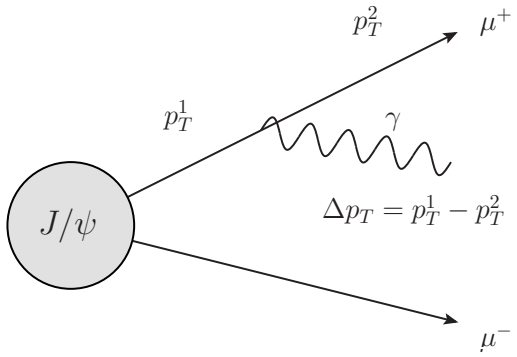

FIGURE F.1: Diagram of muon electromagnetic radiation.

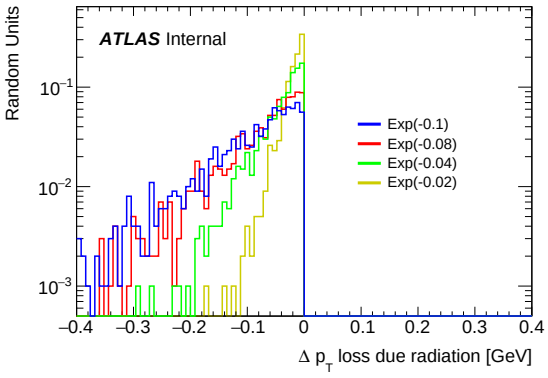

FIGURE F.2: Exponential distribution for four different values of λ.

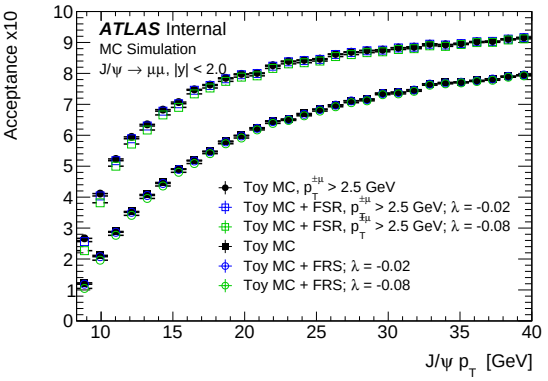

FIGURE F.3: J/ψ kinematic acceptance as a function of p_{T}. Calculated with and without a cut in the daughters muons and with and without FSR emulation.

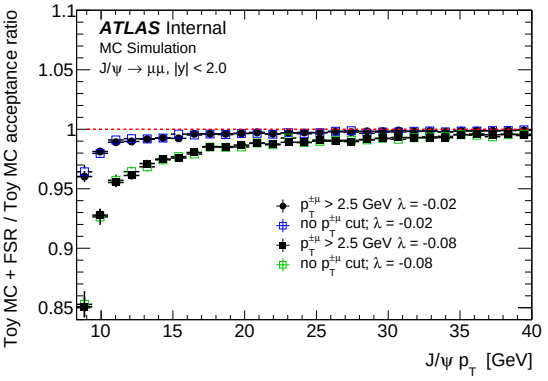

FIGURE F.4: Ratio of the acceptance get from the toy MC plus FSR and the standard toy MC (without FSR).

Bibliography

[1] Adare, A. and others (PHENIX Collaboration). "Cold Nuclear Matter Effects on J/ψ Yields as a Function of Rapidity and Nuclear Geometry in Deuteron-Gold Collisions at $\sqrt{(s_{NN})}$ = 200 GeV". In: *Phys. Rev. Lett.* 107 (2011), p. 142301. DOI: 10.1103/PhysRevLett.107.142301. arXiv: 1010.1246 [nucl-ex].

[2] ALICE Collaboration. In: *Phys. Rev. Lett.* 108 (2012), p. 082001. DOI: 10.1103/PhysRevLett.108.082001. arXiv: 1111.1630 [hep-ex].

[3] ALICE Collaboration. In: *Phys. Lett.* B766 (2017), pp. 212–224. DOI: 10.1016/j.physletb.2016.12.064. arXiv: 1606.08197 [nucl-ex].

[4] ALICE Collaboration. "Centrality, rapidity and transverse momentum dependence of J/ψ suppression in Pb-Pb collisions at $\sqrt{s_{\rm NN}}$=2.76 TeV". In: *Phys. Lett.* B734 (2014), pp. 314–327. DOI: 10.1016/j.physletb.2014.05.064. arXiv: 1311.0214 [nucl-ex].

[5] ALICE Collaboration. "D meson nuclear modification factors in Pb-Pb collisions at $\sqrt{s_{NN}} = 2.76$ TeV with the ALICE detector". In: *Nucl. Phys.* A904-905 (2013), pp. 635c–638c. DOI: 10.1016/j.nuclphysa.2013.02.096. arXiv: 1210.7332 [hep-ex].

[6] ALICE Collaboration. "Inclusive, prompt and non-prompt J/ψ production at mid-rapidity in Pb-Pb collisions at $\sqrt{s_{\rm NN}}$ = 2.76 TeV". In: *JHEP* 07 (2015), p. 051. DOI: 10.1007/JHEP07(2015)051. arXiv: 1504.07151 [nucl-ex].

[7] B. Alver et al. In: (2008). arXiv: 0805.4411 [nucl-ex].

[8] J. F. Amundson et al. "Colorless states in perturbative QCD: Charmonium and rapidity gaps". In: *Phys. Lett.* B372 (1996), pp. 127–132. DOI: 10.1016/0370-2693(96)00035-4. arXiv: hep-ph/9512248 [hep-ph].

[9] A. Andronic et al. In: *Eur. Phys. J.* C76.3 (2016), p. 107. DOI: 10.1140/epjc/s10052-015-3819-5. arXiv: 1506.03981 [nucl-ex].

[10] François Arleo. "Quenching of Hadron Spectra in Heavy Ion Collisions at the LHC". In: *Phys. Rev. Lett.* 119.6 (2017), p. 062302. DOI: 10.1103/PhysRevLett.119.062302. arXiv: 1703.10852 [hep-ph].

[11] Samuel Aronson et al. "Collisional and thermal dissociation of J/ψ and Υ states at the LHC". In: (2017). arXiv: 1709.02372 [hep-ph].

[12] ATLAS Collaboration. In: *JINST* 3 (2008), S08003. DOI: 10.1088/1748-0221/3/08/S08003.

[13] ATLAS Collaboration. In: *ATLAS-CONF-2015-030* ATLAS-CONF-2015-030 (2015). URL: https://cds.cern.ch/record/2037967.

[14] ATLAS Collaboration. In: *ATLAS-CONF-2016-123* ATLAS-CONF-2016-123 (2016). URL: https://cds.cern.ch/record/2215434.

[15] ATLAS Collaboration. In: *ATLAS-HION-2014-05-001* ATLAS-HION-2014-05-001 (2017). URL: https://cds.cern.ch/record/2240145.

[16] ATLAS Collaboration. "Improved luminosity determination in pp collisions at $\sqrt{(s)}$ = 7 TeV using the ATLAS detector at the LHC". In: *Eur. Phys. J.* C73.8 (2013), p. 2518. DOI: 10.1140/epjc/s10052-013-2518-3. arXiv: 1302.4393 [hep-ex].

[17] ATLAS Collaboration. "Measurement of charged-particle spectra in Pb+Pb collisions at $\sqrt{s_{\mathrm{NN}}} = 2.76$ TeV with the ATLAS detector at the LHC". In: *JHEP* 09 (2015), p. 050. DOI: 10.1007/JHEP09(2015)050. arXiv: 1504.04337 [hep-ex].

[18] ATLAS Collaboration. "Measurement of the centrality dependence of J/ψ yields and observation of Z production in lead–lead collisions with the ATLAS detector at the LHC". In: *Phys. Lett.* B697 (2011), pp. 294–312. DOI: 10.1016/j.physletb.2011.02.006. arXiv: 1012.5419 [hep-ex].

[19] ATLAS Collaboration. "Measurement of the muon reconstruction performance of the ATLAS detector using 2011 and 2012 LHC proton–proton collision data". In: *Eur. Phys. J.* C74.11 (2014), p. 3130. DOI: 10.1140/epjc/s10052-014-3130-x. arXiv: 1407.3935 [hep-ex].

[20] ATLAS Collaboration. "Muon reconstruction performance of the ATLAS detector in proton–proton collision data at $\sqrt{s}$ =13 TeV". In: *Eur. Phys. J.* C76.5 (2016), p. 292. DOI: 10.1140/epjc/s10052-016-4120-y. arXiv: 1603.05598 [hep-ex].

[21] ATLAS Collaboration. "Performance of the ATLAS Trigger System in 2015". In: *Eur. Phys. J.* C77.5 (2017), p. 317. DOI: 10.1140/epjc/s10052-017-4852-3. arXiv: 1611.09661 [hep-ex].

[22] ATLAS Collaboration. "The ATLAS Level-1 Muon Topological Trigger Information for Run 2 of the LHC". In: *Journal of Instrumentation* 10.02 (2015), p. C02027. URL: http://stacks.iop.org/1748-0221/10/i=02/a=C02027.

[23] R. Baier et al. "Radiative energy loss of high-energy quarks and gluons in a finite volume quark - gluon plasma". In: *Nucl. Phys.* B483 (1997), pp. 291–320. DOI: 10.1016/S0550-3213(96)00553-6. arXiv: hep-ph/9607355 [hep-ph].

[24] Elisabetta Barberio and Zbigniew Was. In: *Comput. Phys. Commun.* 79 (1994), pp. 291–308. DOI: 10.1016/0010-4655(94)90074-4.

[25] Olaf Behnke et al. *Data Analysis in High Energy Physics*. WILEY-VCH, 2013.

[26] N. Brambilla et al. In: *Eur. Phys. J.* C71 (2011), p. 1534. DOI: 10.1140/epjc/s10052-010-1534-9. arXiv: 1010.5827 [hep-ph].

[27] P. Braun-Munzinger and J. Stachel. In: *Phys. Lett.* B490 (2000), pp. 196–202. DOI: 10.1016/S0370-2693(00)00991-6. arXiv: nucl-th/0007059 [nucl-th].

[28] N. Cabibbo and G. Parisi. "Exponential Hadronic Spectrum and Quark Liberation". In: *Phys. Lett.* 59B (1975), pp. 67–69. DOI: 10.1016/0370-2693(75)90158-6.

[29] Shanshan Cao et al. "Collisional vs. Radiative Energy Loss of Heavy Quark in a Hot and Dense Nuclear Matter". In: *Nucl. Phys.* A904-905 (2013), pp. 653c–656c. DOI: 10.1016/j.nuclphysa.2013.02.100. arXiv: 1209.5410 [nucl-th].

[30] M. Capeans et al. "ATLAS Insertable B-Layer Technical Design Report". In: (2010). URL: https://cds.cern.ch/record/1291633.

[31] CDF Collaboration. In: *Phys. Rev.* D71 (2005), p. 032001. DOI: 10.1103/PhysRevD.71.032001. arXiv: hep-ex/0412071 [hep-ex].

[32] Baoyi Chen et al. "Detailed rapidity dependence of J/ψ production at energies available at the Large Hadron Collider". In: *Phys. Rev.* C93.5 (2016), p. 054905. DOI: 10.1103/PhysRevC.93.054905. arXiv: 1510.07466 [hep-ph].

[33] CMS Collaboration. In: *Phys. Lett.* B727 (2013), pp. 381–402. DOI: 10.1016/j.physletb.2013.10.055. arXiv: 1307.6070 [hep-ex].

[34] CMS Collaboration. "Relative Modification of Prompt $\psi(2S)$ and J/ψ Yields from pp to PbPb Collisions at $\sqrt{s_{NN}} = 5.02$TeV". In: *Phys. Rev. Lett.* 118.16 (2017), p. 162301. DOI: 10.1103/PhysRevLett.118.162301. arXiv: 1611.01438 [nucl-ex].

[35] CMS Collaboration. "Suppression and azimuthal anisotropy of prompt and nonprompt J/ψ production in PbPb collisions at $\sqrt{s_{\mathrm{NN}}} = 2.76$ TeV". In: *Eur. Phys. J.* C77.4 (2017), p. 252. DOI: 10.1140/epjc/s10052-017-4781-1. arXiv: 1610.00613 [nucl-ex].

[36] John C. Collins and M. J. Perry. "Superdense Matter: Neutrons Or Asymptotically Free Quarks?" In: *Phys. Rev. Lett.* 34 (1975), p. 1353. DOI: 10.1103/PhysRevLett.34.1353.

[37] S. Digal, P. Petreczky, and H. Satz. "Quarkonium feed down and sequential suppression". In: *Phys. Rev.* D64 (2001), p. 094015. DOI: 10.1103/PhysRevD.64.094015. arXiv: hep-ph/0106017 [hep-ph].

[38] Yuri L. Dokshitzer and D. E. Kharzeev. "Heavy quark colorimetry of QCD matter". In: *Phys. Lett.* B519 (2001), pp. 199–206. DOI: 10.1016/S0370-2693(01)01130-3. arXiv: hep-ph/0106202 [hep-ph].

[39] Xiaojian Du and Ralf Rapp. "ψ(2S) Production at the LHC". In: *J. Phys. Conf. Ser.* 779.1 (2017), p. 012042. DOI: 10.1088/1742-6596/779/1/012042. arXiv: 1609.04868 [hep-ph].

[40] Xiaojian Du and Ralf Rapp. "Sequential Regeneration of Charmonia in Heavy-Ion Collisions". In: *Nucl. Phys.* A943 (2015), pp. 147–158. DOI: 10.1016/j.nuclphysa.2015.09.006. arXiv: 1504.00670 [hep-ph].

[41] Pietro Faccioli et al. "Towards the experimental clarification of quarkonium polarization". In: *Eur. Phys. J.* C69 (2010), pp. 657–673. DOI: 10.1140/epjc/s10052-010-1420-5. arXiv: 1006.2738 [hep-ph].

[42] E. G. Ferreiro et al. "Impact of the Nuclear Modification of the Gluon Densities on J/ψ production in pPb collisions at $\sqrt{s_{NN}} = 5$ TeV". In: *Phys. Rev.* C88.4 (2013), p. 047901. DOI: 10.1103/PhysRevC.88.047901. arXiv: 1305.4569 [hep-ph].

[43] David J. Gross and Frank Wilczek. "Ultraviolet Behavior of Nonabelian Gauge Theories". In: *Phys. Rev. Lett.* 30 (1973), pp. 1343–1346. DOI: 10.1103/PhysRevLett.30.1343.

[44] Miklos Gyulassy and XinNian Wang. In: *Comput. Phys. Commun.* 83 (1994), p. 307. DOI: 10.1016/0010-4655(94)90057-4. arXiv: nucl-th/9502021 [nucl-th].

[45] Peter Jenni, Marzio Nessi, and Markus Nordberg. *Zero Degree Calorimeters for ATLAS*. Tech. rep. LHCC-I-016. CERN-LHCC-2007-001. Geneva: CERN, 2007. URL: https://cds.cern.ch/record/1009649.

[46] F. Karsch, D. Kharzeev, and H. Satz. "Sequential charmonium dissociation". In: *Phys. Lett.* B637 (2006), pp. 75–80. DOI: 10.1016/j.physletb.2006.03.078. arXiv: hep-ph/0512239 [hep-ph].

[47] B. Z. Kopeliovich et al. In: *Phys. Rev.* C91.2 (2015), p. 024911. DOI: 10.1103/PhysRevC.91.024911. arXiv: 1409.5147 [hep-ph].

[48] B. Z. Kopeliovich et al. "Novel scenario for production of heavy flavored mesons in heavy ion collisions". In: *EPJ Web Conf.* 164 (2017), p. 01018. DOI: 10.1051/epjconf/201716401018. arXiv: 1701.07121 [hep-ph].

[49] B. Z. Kopeliovich et al. "Quantum-mechanical description of in-medium fragmentation". In: *Phys. Rev.* C78 (2008), p. 055204. DOI: 10.1103/PhysRevC.78.055204. arXiv: 0809.4613 [hep-ph].

[50] Andreas S. Kronfeld. "Twenty-first Century Lattice Gauge Theory: Results from the QCD Lagrangian". In: *Ann. Rev. Nucl. Part. Sci.* 62 (2012), pp. 265–284. DOI: 10.1146/annurev-nucl-102711-094942. arXiv: 1203.1204 [hep-lat].

[51] L. Adamczyk et al. (STAR Collaboration). "J/ψ production at low p_T in Au+Au and Cu+Cu collisions at $\sqrt{s_{NN}} = 200$ GeV with the STAR detector". In: *Phys. Rev.* C90.2 (2014), p. 024906. DOI: 10.1103/PhysRevC.90.024906. arXiv: 1310.3563 [nucl-ex].

[52] J. P. Lansberg et al. In: *AIP Conf. Proc.* 1038 (2008), pp. 15–44. DOI: 10.1063/1.2987169. arXiv: 0807.3666 [hep-ph].

[53] LHCb Collaboration. In: *Eur. Phys. J.* C73.11 (2013), p. 2631. DOI: 10.1140/epjc/s10052-013-2631-3. arXiv: 1307.6379 [hep-ex].

[54] LHCb Collaboration. "Prompt and nonprompt J/ψ production and nuclear modification in pPb collisions at $\sqrt{s_{\rm NN}} = 8.16$ TeV". In: (2017). arXiv: 1706.07122 [hep-ex].

[55] T. Matsui and H. Satz. In: *Phys. Lett.* B178 (1986), pp. 416–422. DOI: 10.1016/0370-2693(86)91404-8.

[56] Michael L. Miller et al. In: *Ann. Rev. Nucl. Part. Sci.* 57 (2007), pp. 205–243. DOI: 10.1146/annurev.nucl.57.090506.123020. arXiv: nucl-ex/0701025 [nucl-ex].

[57] Olive, K.A. and others. In: *Chin. Phys. C* 38 (2014), p. 090001. DOI: 10.1088/1674-1137/38/9/090001.

[58] M. Oreglia. "A Study of the Reactions $\psi' \to \gamma\gamma\psi$". In: *Ph.D. Thesis, Standford University, SLAC-236* (1980).

[59] PHENIX Collaboration. "J/ψ Production vs Centrality, Transverse Momentum, and Rapidity in Au+Au Collisions at $\sqrt{s_{NN}} = 200\,\text{GeV}$". In: *Phys. Rev. Lett.* 98 (2007), p. 232301. DOI: 10.1103/PhysRevLett.98.232301. arXiv: nucl-ex/0611020 [nucl-ex].

[60] Robert D. Pisarski and Frank Wilczek. "Remarks on the chiral phase transition in chromodynamics". In: *Phys. Rev. D* 29 (2 1984), pp. 338–341. DOI: 10.1103/PhysRevD.29.338. URL: https://link.aps.org/doi/10.1103/PhysRevD.29.338.

[61] H. David Politzer. "Reliable Perturbative Results for Strong Interactions?" In: *Phys. Rev. Lett.* 30 (1973), pp. 1346–1349. DOI: 10.1103/PhysRevLett.30.1346.

[62] HuaSheng Shao. In: *Comput. Phys. Commun.* 184 (2013), pp. 2562–2570. DOI: 10.1016/j.cpc.2013.05.023. arXiv: 1212.5293 [hep-ph].

[63] Edward V. Shuryak. "Quark-Gluon Plasma and Hadronic Production of Leptons, Photons and Psions". In: *Phys. Lett.* 78B (1978). [Yad. Fiz.28,796(1978)], p. 150. DOI: 10.1016/0370-2693(78)90370-2.

[64] Torbjorn Sjostrand, Stephen Mrenna, and Peter Z. Skands. In: *Comput. Phys. Commun.* 178 (2008), pp. 852–867. DOI: 10.1016/j.cpc.2008.01.036. arXiv: 0710.3820 [hep-ph].

[65] Martin Spousta. "On similarity of jet quenching and charmonia suppression". In: *Phys. Lett.* B767 (2017), pp. 10–15. DOI: 10.1016/j.physletb.2017.01.041. arXiv: 1606.00903 [hep-ph].

[66] Robert L. Thews, Martin Schroedter, and Johann Rafelski. In: *Phys. Rev.* C63 (2001), p. 054905. DOI: 10.1103/PhysRevC.63.054905. arXiv: hep-ph/0007323 [hep-ph].

[67] Wouter Verkerke and David P. Kirkby. In: *eConf* C0303241 (2003). [186(2003)]. arXiv: physics/0306116 [physics].

[68] Jiechen Xu, Jinfeng Liao, and Miklos Gyulassy. "Bridging Soft-Hard Transport Properties of Quark-Gluon Plasmas with CUJET3.0". In: *JHEP* 02 (2016), p. 169. DOI: 10.1007/JHEP02(2016)169. arXiv: 1508.00552 [hep-ph].

[69] B. G. Zakharov. "Radiative energy loss of high-energy quarks in finite size nuclear matter and quark - gluon plasma". In: *JETP Lett.* 65 (1997), pp. 615–620. DOI: 10.1134/1.567389. arXiv: hep-ph/9704255 [hep-ph].